Surface Studies of (110) Terminated Fe_3O_4 & $SrTiO_3$

Brian Conor Walls

School of Physics

Trinity College Dublin

A thesis submitted for the degree of

Doctor of Philosophy

March 2018

Declaration

I declare that this thesis has not been submitted as an exercise for a degree at this or any other university and apart from the advice, assistance and joint effort acknowledged and mentioned in the text, it is entirely my own work.

I agree to deposit this thesis in the University's open access institutional repository or allow the library to do so on my behalf, subject to Irish Copyright Legislation and Trinity College Library conditions of use and acknowledgement.

Brian Walls _____

March 13, 2018

Summary

In this thesis the surface reconstructions of (110) terminated single crystalline Fe_3O_4 and $SrTiO_3$ have been investigated by a host of surface-sensitive techniques. The core of this work focuses on two contrasting $Fe_3O_4(110)$ surface reconstructions investigated primarily by Scanning Tunneling Microscopy (STM). Additionally, the anisotropic optical response of bulk isotropic $Fe_3O_4(110)$ and $SrTiO_3(110)$ are investigated by Reflectance Anisotropy Spectroscopy (RAS).

The anisotropic optical responses of the two metal oxides show similarities: RAS is sensitive to the influence the surface termination has on the bulk-like region in the vicinity of the selvedge. The response is interpreted to originate from small anisotropic shifts in energy of the bulk-like optical transitions associated with an anisotropic strain gradient in the surface region.

Theoretical calculations of the {111}-nanofaceted row reconstruction of $Fe_3O_4(110)$ confirm the presence of an anisotropic strain gradient. The altered stoichiometry of $SrTiO_3$ surface terminations related to *ex-situ* precleaning, and/or *in-situ* cleaning procedures is suggested to give rise to strain and the modification of bulk-like states.

The altered spectra of different $SrTiO_3(110)$ terminations suggests RAS is sensitive to the contrasting modification of bulk-like states by different terminations. Additionally, this optical technique is extremely sensitive to the formation of an anisotropic conductance in the bandgap region associated with the formation of oxygen vacancies correlated to a metallic state and the modification of the Ti 2p core level. This electron gas is concluded to be close

to the surface and is likely anisotropic due to the influence of an anisotropic surface termination.

Annealing $Fe_3O_4(110)$ in oxygen or Ultra-High Vacuum (UHV) environments results in the formation of the known {111}-nanofaceted row reconstruction. However, sputtering prior to annealing results in the coexistence of an atomically flat surface structure alongside the row reconstruction.

Density functional theory calculations combined with the simulation of STM images provides insight into the atomically flat surface structure. Twofold-coordinated oxygen represents the most energetically stable oxygen vacancy on B-plane terminated $Fe_3O_4(110)$. STM simulations reveal that that the atomically flat surface structure corresponds to this energetically favourable B-termination and the oxygen surface vacancies form an ordered array. Calculations of the spin density distributions indicate charge ordering of the surface and sub-surface octahedrally coordinated iron. Charge ordering on this oxygen vacated surface compensates towards a polar compensated termination, and additional polarity compensation mechanisms can lead to a stabilised surface.

X-ray photoelecton spectroscopy measurements of the {111}-nanofaceted row reconstruction demonstrate that the reconstruction exhibits increased Fe^{2+}/Fe^{3+} and Fe/O ratios. However, the electronic properties are observed to differ depending on preparation environment, indicating the reconstruction is stable across some stoichiometry range.

Finally, the anisotropic strain gradient in the surface region identified by RAS, which is sensitive the termination has on the underlying bulk-like region, provides insight into surface sensitive STM/STS measurements: firstly, one-dimensional electronic states are observed and are suggested to originate from the compressive and tensile strain along the $[\bar{1}10]$ direction which gives rise to the inequivalence of electronic states. Secondly, the analysis of missing rows and atomic steps demonstrates that the {111} coverage is maximised at these irregularities. The row reconstructions (1×3) periodicity opposed to a larger periodic unit, which would increase the energetically favourable {111} coverage, is suggested to be a result of the competition between {111} coverage and the associated strain energy.

Acknowledgements

First and foremost I would like to thank my supervisor, Professor Igor Shvets, for the opportunity to pursue a PhD and for his guidance over the past four years. I would also like to thank all past and present members of the Applied Physics Research Group. I have always found everyone to be extremely helpful and the working environment has always been very pleasant.

Thank you to Dr Olaf Lübben, for preforming DFT calculations, providing experimental guidance and for always assisting me at a seconds notice. I would also like to thank Dr Barry Murphy for always being willing and happy to help me with anything and everything over the past four years. Thank you to Dr Karsten Fleischer for conducting XPS measurements, teaching me about RAS, conducting the small majority of strontium titanate RAS measurements and for general assistance and advice in relation to my work. Finally, thank you to Dr. Kriztian Palotás for simulating STM images and for invaluable discussions and contribution.

To the visiting researchers who I have had the pleasure of meeting and working with, namely, Dr Alexander Chaika, Dr Sergey Bozhko and
Dr Andrey Ionov, I would like to thank you for the knowledge and experience that I have gained. I hope my contribution has been helpful and look forward to working with you in the future.

Thank you to Emma and Daragh, for consistently joining me for burritos over the past four plus years, long may it continue.

Finally, I would like to thank my parents for giving me every opportunity to pursue this goal, and for your encouragement throughout.

I dedicate this work to my parents

List of publications

1. ***Oxygen vacancy induced surface stabilization: (110) terminated magnetite***
   Brian Walls, Olaf Lübben, Kriztian Palotás, Karsten Fleischer, Killian Walshe and Igor V. Shvets
   Physical Review B **94**, 165424 (2016)

2. ***Nanoclusters and nanolines: the effect of molybdenum oxide substrate stoichiometry on iron self-assembly***
   Olaf Lübben, Sergey A. Krasnikov, **Brian Walls**, Natalia N. Sergeeva, Barry E. Murphy, Alexander N. Chaika, Sergey I. Bozhko and Igor V. Shvets
   Nanotechnology **28**, 205602 (2017)

3. ***Optical anisotropy of $SrTiO_3$(110) for different surface terminations***
   Karsten Fleischer, Sangsoo Kim, **Brian Walls**, Kuanysh Zhussupbekov, Igor V. Shvets
   Physica Status Solidi B, 1700459 (2017)

List of abstracts presented

1. ***Surface structure of Fe_3O_4(110) investigated by Scanning Tunneling Microscopy and Density Functional Theory***
   Brian Walls*, Olaf Lübben, Krisztian Palotás, and Igor V. Shvets
   Deutsche Physikalische Gesellschaft (DPG) spring meeting, Regensburg, Germany, March 2016

2. ***Surface structure of (110) terminated magnetite investigated by scanning tunneling microscopy and density functional theory***
   Brian Walls*, Olaf Lübben, Krisztian Palotás, Karsten Fleischer, Killian Walshe and Igor V. Shvets
   32nd European Conference on Surface Science (ECOSS32), Grenoble, France, August 2016

3. ***Electronic structure and transport properties of graphene nanoribbons grown on SiC(001)***
   A. N. Chaika*, H. -C. Wu, O. V. Molodtsova, S. V. Babenkov, M. -C. Hsu, T. -W. Huang, Mourad Abid, Mohamed Abid, Y. Niu, **B. Walls**, B. E. Murphy, I. V. Shvets, H. Liu, B. S. Chun, Y. T. Janabi, S. N. Molotkov, A. I. Lichtenstein, M. I. Katsnelson, C. -R. Chang and V. Yu. Aristov.
   XXI International Conference on Nanophysics & Nanoelectronics, Nizhniy Novgorod, Russia, March 2017

4. ***STM visualization of surface and subsurface atomic structure of Gd_3Si_5/Si(111) using clean and oxygen-terminated tungsten tips***
   A. N. Chaika*, O. Lübben, J. I. Cerdá, C. Rogero, J. A. Martin-Gago, **B. Walls** and I. V. Shvets.
   16th International Conference on the Formation of Semiconductor Interfaces, Hannover, Germany, July 2017

*Presenting author

List of abbreviations

UHV	-	ultra-high vacuum
STM	-	scanning tunneling microscopy
DFT	-	density functional theory
RAS	-	reflectance anisotropy spectroscopy
2D	-	two-dimensional
XPS	-	x-ray photoelectron spectroscopy
STS	-	scanning tunneling spectroscopy
1D	-	one-dimensional
DOS	-	density of states
CCM	-	constant-current mode
CHM	-	constant-height mode
LEED	-	low-energy electron diffraction
TSP	-	titanium sublimation pump
PEM	-	photo elastic modulator
UPS	-	ultraviolet photoelectron spectroscopy
UV	-	ultraviolet
BO	-	Born-Oppenheimer
LDA	-	local density approximation
GGA	-	general gradient approximation
FCC	-	face-centred cubic
T_V	-	Verwey transition temperature
HCP	-	hexagonal close-packed
Q2DEG	-	quasi-two-dimensional electron gas
RHEED	-	reflection high-energy electron diffraction
IR	-	infrared
PAW	-	projector-augmented- wave
VASP	-	Vienna *ab-initio* simulation package
PBE	-	Perdew-Burke-Ernzerhof
MP	-	Monkhorst-Pack

Contents

List of Figures

Chapter 1

Introduction

Metal oxides display a wide variety of structures and correlated physical and chemical properties due to the range of different oxidation states metal cations can adopt. This versatility sees the class of materials utilised in a diverse range of applications and the surface plays a role in the vast majority of these. For example, metal oxide surfaces are pivotal in fields ranging from catalysis to modern electronics, and the oxidation of metals in ambient conditions results in metal oxides dictating processes such as friction, lubrication, wetting and corrosion.

Arguably the most important industrially and economically application of metal oxide surfaces is found in heterogeneous catalysis, where they are utilised as catalysts and offer catalytic support for a diverse range of reactions. For example, metal oxides routinely serve as a source of oxygen [1], are catalysts in industrial processes such as ammonia [2] and methanol synthesis [3] and catalyse the reduction of H_2O and N_2O to form molecular hydrogen [4] (the water-gas shift reaction) and elemental nitrogen [5], respectively.

Metal oxide terminations prepared in Ultra-High Vacuum (UHV) often exhibit complex reconstructions related to the ease at which their stoichiometry can be altered by *in-situ* preparation techniques and, in the case of polar terminations, the need to compensate for their polarity [6]. The range of structures and correlated properties which these surfaces can adopt sees them provide excellent templates for the growth of nanostructures of various sizes

and shapes (see for example, [7–11]). The fundamental understanding of the formation and atomic structure of $Fe_3O_4(001)$ has lead to the emerging study of single atom catalysis whereby this magnetite surface acts to catalyse the splitting of single molecules [12] or supports catalytically active single atoms [13]. It has been demonstrated that the surface and near-surface atomic scale structure dictates the absorption properties [10, 12–15]. Finally, heterostructures comprised of one or more polar metal oxide terminations often show fascinating properties at the interface, which drastically differ from those of their individual components. For example, heterostructure interfaces comprised of insulating oxide perovskites, which can grow epitaxially due to their similar lattice parameters, exhibit properties ranging from high-mobility to superconductivity [16–20].

It is clear that the characterisation of metal oxide terminations is required in order to probe their potential as a template for both nanostructure growth and the fundamental investigation of catalysis on the atomic scale. The understanding of the surface physics is also of importance in heterostructures, where interesting phenomena occur at the interface where two terminations interact.

As such in this thesis an investigation of the (110) terminations of magnetite (Fe_3O_4) and strontium titanate ($SrTiO_3$) is presented. Fe_3O_4 and $SrTiO_3$ crystallise into cubic inverse spinel and perovskite structures, respectively, and their (110) terminations are polar. The focus of this work is on formation and structure of two contrasting $Fe_3O_4(110)$ surface reconstructions. The primary technique utilised is Scanning Tunneling Microscopy (STM), which is combined with a range of surface-sensitive techniques and Density Functional Theory (DFT) calculations. Due to strontium titanate's insulating nature the focus of the $SrTiO_3(110)$ study is on the optical anisotropy of different surface terminations probed by Reflectance Anisotropy Spectroscopy (RAS).

The experimental techniques and set-up are discussed in chapter 2. In chapter 3 iron oxides and perovskites in general are introduced and a detailed introduction to Fe_3O_4 and $SrTiO_3$ is presented. A literature review of

metal oxide, magnetite and strontium titanate surface science is presented in chapter 4.

In chapter 5 the anisotropic optical response of the (110) terminations of bulk isotropic $SrTiO_3$ and Fe_3O_4 are investigated by RAS. In both cases RAS is sensitive to the influence that the surface structure has on the bulk-like region in the vicinity of the selvedge. The response is interpreted to originate from small anisotropic shifts in the energy of bulk-like optical transitions associated with an anisotropic strain gradient in the surface region. In the case of the {111}-nanofaceted row reconstruction of $Fe_3O_4(110)$, the existence of an anisotropic strain gradient is confirmed by DFT calculations and provides insight into surface sensitive STM measurements. Therefore, this study demonstrates the potential of combining surface sensitive measurements with RAS measurements, which are sensitive the termination has on the underlying bulk-like region. In the case of wide bandgap $SrTiO_3$, RAS is sensitive to the formation of a 2-Dimensional (2D) anisotropic conductance in the bandgap correlated to oxygen vacancies, which form during vacuum annealing. This is promising for work on $SrTiO_3/LaAlO_3$ heterostructures as RAS is a non-destructive probe, which can monitor the formation of the 2D electron gas which forms at the interface during growth.

In chapter 6 the surface structure of the {111}-nanofaceted row reconstruction of $Fe_3O_4(110)$ is examined. The chapter is split into two parts, firstly the influence of the annealing environment on the formation and structure of the reconstruction is presented: X-ray Photoelectron Spectroscopy (XPS) measurements demonstrate that the reconstruction is reduced, however the combination of Scanning Tunneling Spectroscopy (STS) and RAS measurements suggest the reconstruction's electronic properties differ depending on the annealing environment, and this indicates the reconstruction is stable across some stoichiometry range. Secondly, an investigation of the atomic and electronic structure is presented: analysis of high resolution STM images provides insight into the surface termination, while the observation of 1-Dimensional (1D) electronic states and the analysis of atomic steps and missing rows is understood in terms of the anisotropic strain in the terminating layers identified by RAS.

A contrasting atomically flat $Fe_3O_4(110)$ reconstruction is presented in chapter 7 which forms as a result of sputtering prior to annealing. The combination of a DFT study with the simulation of STM images allows one to draw conclusions on the atomic structure of the termination. Furthermore, the DFT calculations provide insight into the polarity compensation mechanism.

Chapter 2

Experimental Techniques & Set-up

2.1 Scanning tunneling microscopy

The scanning tunneling microscope was developed in the early 1980s, and in 1986 the Nobel prize in Physics was awarded to Binning and Rohrer for its development. The (110) surface of Au and $CaIrSn_4$ were initially investigated and the resolution of monoatomic steps demonstrated the STM's capabilities [21]. 30 years later the STM can routinely probe features on the Ångström scale and in this decade orbital resolution has been reported [22].

At the time of its invention the STM represented a real-space, non-destructive technique with order of magnitudes better resolution than any and all other techniques. In the proceeding 30 years, the ability of the STM to observe electronic and structural features on the sub-nanometer scale has led to the technique playing a vital role in the growth of the surface science field.

2.1.1 Tunneling theory

The underlying principle behind the operation of the STM is quantum tunneling. Consider an electron with energy E in a potential $U(z)$. The spatial evolution of the electron's wavefunction, $\varphi(z)$, can be described by the time-

independent Schrödinger equation:

$$\left(\frac{-\hbar^2}{2m}\frac{\mathrm{d}^2}{\mathrm{d}z^2} + U(z)\right)\varphi(z) = E\varphi(z) \tag{2.1}$$

m is the mass of the electron and $\hbar$ is the reduced Planck constant.

For an electron encountering a potential barrier there are three regions (depicted in figure 2.1(a)) to be considered: (I) The wave incident on the barrier, $U = 0$ and $-\infty < z \leq 0$. (II) The wave inside the barrier, $U > E$ and $0 \leq z \leq d$. (III) The wave transmitted through the barrier, $U = 0$ and $d \leq z < \infty$. Classically, in region II with $U > E$, the electron's wavefunction is exactly zero. Therefore, the probability of an electron tunneling through the barrier is also zero. However, a non-zero solution for equation 2.1 exists*:

$$\varphi(z) = \varphi(0)\exp(-\kappa z) \qquad \kappa = \sqrt{\frac{2m(U-E)}{\hbar^2}} \tag{2.2}$$

Taking into account periodic boundary conditions:

$$\varphi(d)_{II} = \varphi(d)_{III} = \varphi(0)\exp(-\kappa d) \tag{2.3}$$

The probability of tunneling occurring is proportional to the square of the electron's wavefunction (equation 2.2):

$$P \propto |\varphi(0)|^2 \exp(-2\kappa d) \tag{2.4}$$

When considering STM, regions I, II and III in figure 2.1(a) represent the sample, vacuum gap and the STM tip as seen in figure 2.1(b). $z = 0$ and $z = \mathrm{d}$ correspond to the surface and the tip apex, respectively. At 0 K, a bias voltage, V, must be applied between the STM tip and the surface for electrons to tunnel into unoccupied states. The applied bias voltage defines the energy range for which tunneling can occur. d now represents the tip-surface distance and at low bias voltages (U - E) is approximately equal to the surface work function, ϕ_s.

*A positive exponent would also provide a solution. However, an exponentially increasing wavefunction is unrealistic.

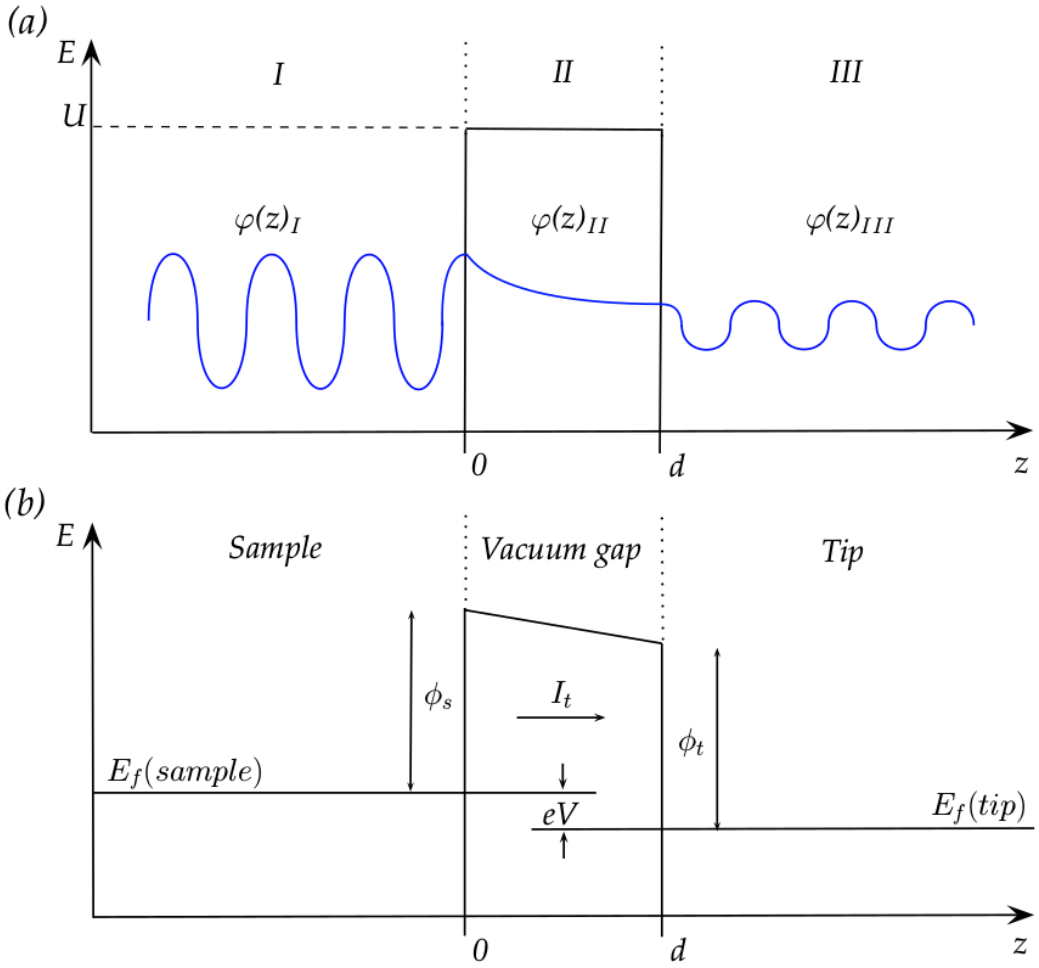

Figure 2.1: (a) An electron with an associated wavefunction, $\varphi(z)$, approaching an energetic barrier. Three regions are considered: (I) The wave incident on the barrier, (II) The wave inside the barrier and (III) The wave transmitted through the barrier. $\varphi(z)_I$ takes the form of a sine wave. Within the barrier $\varphi(z)_{II}$ decays exponentially. On the other side of the barrier $\varphi(z)_{III}$ takes the form of a sine wave, the magnitude of which depends on the magnitude of $\varphi(z)_I$ and the energetic barrier width and height (see equation 2.3). (b) When considering this tunneling phenomena in STM, regions I, II and III represent the sample, vacuum gap and the STM tip. A bias voltage must be applied between the STM tip and surface for electrons to tunnel into unoccupied states. In the above case a negative bias is applied to the sample with respect to the tip, and hence, the samples filled states are probed as electrons tunnel from the surface to the tip. In the low bias limit, the energetic barrier is approximated as the work function of the surface atoms.

The tunneling current is proportional to the sum of the individual probabilities (equation 2.4) over the energy range $E_f - eV \leq E \leq E_f$:

$$I_t \propto \sum_{E_f - eV}^{E_f} |\varphi(0)|^2 \exp(-2\kappa d) \qquad \kappa = \sqrt{\frac{2m\phi_s}{\hbar^2}} \tag{2.5}$$

E_f and V represent the Fermi energy and the applied bias voltage. Furthermore, the tunneling current depends on the number of states present at each energy increment across the probed energetic range. By definition, the Density Of States (DOS) at some energy, E, is the sum of the square of the wavefunctions between E - ϵ and E, per unit energy:

$$\rho(E, z) = \frac{1}{\epsilon} \sum_{E-\epsilon/2}^{E+\epsilon/2} |\varphi_n(z)|^2$$

In the low bias voltage limit the energy increment, ϵ, is equal to eV. Furthermore, if we take $z = 0$ we consider the DOS of the surface states (see figure 2.1(b)):

$$\rho_s(E_f, 0) = \frac{1}{eV} \sum_{E_f - eV/2}^{E_f + eV/2} |\varphi_n(0)|^2 \tag{2.6}$$

Combining equations 2.5 and 2.6 we obtain an expression for the tunneling current which is related to the surface DOS:

$$I_t \propto V \rho_s(E_f, 0) \exp(-2\kappa d) \qquad \kappa = \sqrt{\frac{2m\phi_s}{\hbar^2}} \tag{2.7}$$

The most important thing to note from this equation is that the tunneling current varies exponentially with d, the tunneling gap.

It is worth considering a hypothetical tip-surface system to explore the relative contribution from different surface atoms and atomic layers to the overall tunneling current. Let us consider Au(110), the first surface examined by STM. Consecutive (110) layers of gold are separated by 1.4 Å and the unit cell distance of the (110) surface is 2.8 Å. Considering that gold has a work function of 5.1 eV, $\kappa = 1.15\,\text{Å}^{-1}$. If we take a typical tip-surface distance of

5 Å the ratio of current contributions from the surface and first sub-surface layer is $I_1/I_2 \approx 25$. Similarly, the current contributions from an atom directly under the tip-apex and its nearest neighbour on the surface is $I_1/I_2 \approx 5$. These examples demonstrate that the surface sensitivity and high resolution of the STM is due to the exponential dependence of the current with the tunneling gap width. For more in depth reviews of the operating principle and theory of STM the reader is referred to [23] and [24].

2.1.2 The scanning tunneling microscope

An STM consists of an extremely sharp conducting tip, with an apex radius of curvature of tens of nanometers, which is approached to a conductive sample surface. At extremely small tip-surface distances, of the order of a nanometer or less, the tip detects the surface via the tunneling of electrons from tip to surface or vice versa when a bias is applied across the junction. Once the tunneling current is achieved the tip is rastered across the surface. Two scanning modes which are depicted in figure 2.2 are widely used; (1) Constant-Current Mode (CCM): as the tip is rastered across the surface a constant current is maintained by a feedback loop which adjusts the tip height accordingly. Atomic steps, absorbents or different atomic species can lead to an increase or decrease in the tunneling current, and hence, a change in the tip height to maintain the desired current. Therefore, in CCM a map of

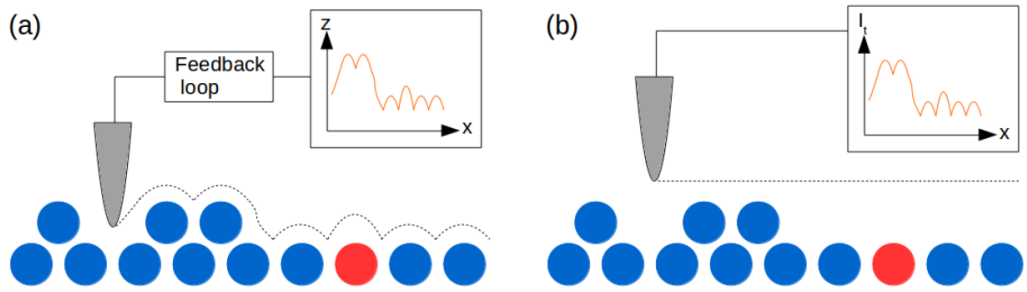

Figure 2.2: (a) Constant-current mode: the feedback loop adjusts the z-height as the tip is moved across the surface in order to maintain a desired current. (b) Constant-Height Mode: the feedback loop is turned off. The current is recorded as the tip is moved across the surface at a constant height.

the z-height provides information related to surface features. (II) Constant-height mode (CHM): the tip is rastered across the surface with the feedback loop turned off. Here, the current at each point is plotted and this three-dimensional map provides insight into structural features. In practice, prior to scanning in CHM, a CCM scan is obtained and the slope of the image is utilised in such a way that the plane of the CHM image is parallel to the surface. This reduces the likelihood that the tip will crash into the surface whilst scanning.

Each scanning mode has its advantages and disadvantages. CCM is better suited to atomically rough surfaces. The feedback loop adjusts the z-height to maintain a constant current, hence preventing the tip from crashing into the surface. However, one disadvantage is that the finite response time of the feedback loop network limits the speed at which the tip can be moved across the surface. In CHM there is no feedback loop, and hence, no limitations to the scan speed. Therefore, CHM images can minimise image distortion due to piezo creep and thermal drift. One clear disadvantage is the possibility of crashing the tip into the surface.

Extremely fine, controllable and reproducible movement of the tip is required to realise the potential of the STM. Such movement is provided by piezoelectric ceramics. Piezoelectric crystals are materials which exhibit spontaneous ferroelectricity, that is, the charge centres of the positive and negative ions of the crystals unit cell are separated. Applying an electric field along the axis of charge separation gives rise to the elongation or compression of the unit cell. Such crystals routinely exhibit a piezoelectric constant of a few Å/V. Therefore, they are ideal for the movement of an STM tip.

Scanning can be performed by a piezo tube which consists of four quadrant piezo stripes. Applying positive and negative biases to opposing stripes will result in these two quadrants expanding and compressing, respectively, the net result is the bending of the piezo tube, and hence, movement of the tip.

The STM utilised in this work makes use of slip-stick motion for course movement. If the rate at which the voltage applied to the piezo (slew rate) is above a certain threshold, the piezo can overcome the friction between it

and the body it contacts (ceramic plate) and 'slip' relative to this ceramic plate. In turn, if the slew rate is below the threshold as the voltage is reduced back to zero, the piezo will not overcome the friction and will 'stick' relative to the ceramic plate. Hence, a waveform consisting first of a high slew rate increasing the voltage to some value V, followed by a low slew rate reducing the voltage to zero can move a piezo relative to the ceramic plate it contacts.

2.1.3 The scanning tunneling microscopy system

The UHV STM chamber consists of a load-lock, preparation chamber and analysis chamber. Typical cleaning procedures such as annealing in UHV and oxygen atmospheres and ion bombardment can be performed within the preparation chamber. Low-Energy Electron Diffraction (LEED) apparatus is utilised to characterise the surface. A base pressure of 1×10^{-10} mbar is maintained by an ion pump and a Titanium Sublimation Pump (TSP), which resides inside the ion pump. The TSP is typically utilised after the chamber has been exposed to argon or oxygen atmospheres. Whilst the preparation chamber is exposed to argon or oxygen atmospheres, the ion pump valve is closed and the pressure is maintained by a turbo pump which resides in the adjoining load-lock. Argon and oxygen are introduced to the chamber via leak valves. The preparation chamber is equipped with a strain-free silica window which allows for *in-situ* optical measurements to be performed.

Sample or tip heating can be performed by resistive heating alone or by the combination of resistive heating and electron bombardment. The filament (tungsten) for restive heating resides under the sample plate (back heating). The heating stage is electrically isolated from the chamber, hence, a voltage can be applied to the heating stage. Thermally emitted electrons are accelerated towards the heating stage, and hence, the back of the sample plate. The temperature of the sample can be estimated from a K-type thermocouple. Furthermore, above 600 °C the temperature can be measured by an optical pyrometer. Electron bombardment, which is a more localised heating technique, will lead to the thermocouple drastically underestimating the temperature. Therefore, when electron bombardment is utilized to achieve

higher temperature and/or a lower base pressure, the pyrometer represents a better method of estimating the sample temperature.

For sputtering, argon is leaked directly into the gas cell of the ion gun and is ionised by electron bombardment. Ar^+ ions are accelerated through a biased ring. Typically, voltages ranging from - 0.5 to - 2 keV are applied. Depending on the bias voltage and argon partial pressure, Ar^+ currents of 10 μA to 40 μA are measured.

With the STM cooled to 78 K, a base pressure of 3×10^{-11} mbar is maintained in the analysis chamber by an ion pump and a TSP. Surface analysis is performed by a low-temperature slider-type STM from Createc. Course movement is performed by shear piezo stacks which are in contact with ceramic plates. Vibration isolation is provided by springs from which the microscope hangs from as well as by an eddy-current damping system. Furthermore, the entire chamber can be floated by a damping system which consists of four pressurised (2 bar) canisters. The STM can be operated at room, liquid nitrogen ($\sim$78 K) and liquid helium ($\sim$4 K) temperatures. The STM is positioned directly below two cryostats. The inner cryostat is a meter-tall cylinder and is surrounded by the outer cryostat. For operation at $\sim$78 K both of the cryostats are filled with liquid nitrogen. For operation at $\sim$4 K the inner cryostat is filled with liquid helium while the outer is filled with liquid nitrogen, which acts to reduce the evaporation of liquid helium. The cables of the STM run vertically in-between the two separated cryostats to connectors above the cryostats outside of the chamber. One disadvantage of this configuration is that noise can be introduced in the tunneling current due to the relatively long length of wire between the tip and the operational amplifier, which converts the small (of the order of a nanometer) tunneling current into a relatively large (of the order of a volt) voltage.

2.1.4 Tip preparation

STM tips have been prepared *ex-situ* by electrochemically etching polycrystalline and single-crystalline tungsten ingots. The electrochemically etching set-up is presented in figure 2.3. NaOH pellets are mixed with deionised

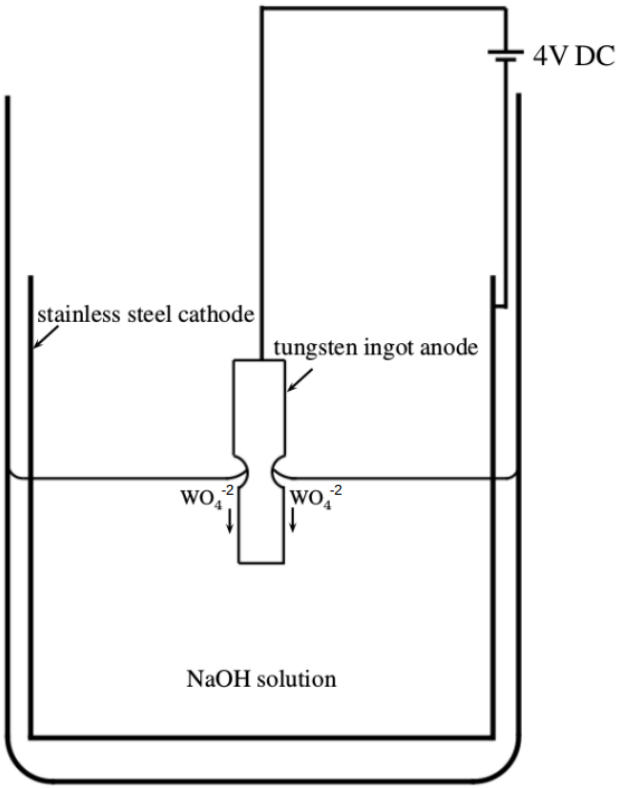

Figure 2.3: Schematic of electrochemically etching. Tungsten reacts with ionised hydroxide to form soluble tungstate ($WO_4{}^{-2}$) which falls and acts as a protective layer against etching. Therefore, etching predominately occurs at the meniscus. The ingot will break when the tungsten cross section at the meniscus can no longer support the weight of the immersed tungsten.

water at a ratio of 8 g of NaOH per 100 ml of deionised water. A cylindrical stainless-steel cathode is placed at the edge of a beaker and the tungsten ingot which serves as an anode is partially immersed in the solution at the centre of the beaker. When a direct current voltage is applied the following reaction takes place [23]:

$$\text{Cathode} : 6H_2O + 6e^- \rightarrow 3H_2 + 6OH^{-1}$$

$$\text{Anode} : W + 8OH^{-1} \rightarrow WO_4{}^{-2} + 4H_2O + 6e^-$$

$$\text{Overall} : W + 2OH^{-1} + 2H_2O \rightarrow WO_4{}^{-2} + 3H_2$$

This reaction involves the oxidation dissolution of tungsten into soluble tungstate ($WO_4{}^{-2}$) at the anode. This heavy tungsten oxide falls down and forms a protective layer around the tungsten ingot resulting in a reduced etching rate below the meniscus [25]. A cut-off current is set such that when the current drops below this value the voltage is cut-off. In the tip preparation set-up used in this work, with a cut-off of 2.5 A, the current drops below this value when the tip breaks in half. Hence, the cut-off prevents further etching of the tip apex.

Ideally, an electrochemically etched tip should have an aspect ratio of approximately 1:1, be symmetric and be as sharp as possible. The length of the ingot, which is immersed in the solution dictates the shape and length of the resultant etched tip: a greater length (and hence, weight) will lead to the ingot breaking at larger cross sectional areas (at the meniscus). To ensure the etched tip is symmetric the ingot should be perpendicular to the solution's surface. Through trial and error it has been determined that the best tips are produced by immersing ∼2.5 mm of an ingot of diameter 0.2 mm into the solution. This is judged by both the shape of the tip viewed by an optical microscope and the performance of the tip during STM experiments.

After etching the tip is dipped in isopropanol and hot water several times in order to remove any remaining NaOH solution. It is paramount that the tip apex does not rapidly breach the surface of the isopropanol or warm water as this action can alter the tip apex. After the tip is washed it is loaded in a UHV chamber as soon as possible to limit oxidation.

2.1.5 Scanning tunneling spectroscopy

STS examines of how the tunneling current varies as a function of the bias voltage or tip-surface separation. The bias voltage defines the surface and tip states which are probed. Say the bias voltage is $+V$, increasing the bias voltage by some energy increment, ϵ, leads to new surface states which reside $eV + \epsilon$ above the Fermi level being involved in the tunneling process. The change in the tunneling current as the bias voltage is increased by ϵ reflects the presence of states at $eV + \epsilon$. Hence, $\frac{\mathrm{d}I}{\mathrm{d}V}$ reflects the local DOS of the

surface. To express this mathematically, we return to equation 2.7, however the surface DOS is replaced with the local density of states, $N_s(E)$:

$$I_t \propto V \exp(-2\kappa d) \int_0^{eV_{bias}} N_s(E) dE$$

Taking the first derivative with respect to the voltage, and expressing it at $V = V_{bias}$, gives:

$$\frac{\mathrm{d}I_t}{\mathrm{d}V}(V_{bias}) \propto V_{bias} N_s(eV_{bias}) + \int_0^{eV_{bias}} N_s(E) dE \tag{2.8}$$

This derivation relies on the approximation that in the low bias limit the tunneling current is linearly proportional to the bias voltage. At larger bias the tunneling current does not exhibit ohmic behaviour; the tunneling probability of electrons is always higher closer to the Fermi level. Furthermore, the tunneling current is a convolution of the tip and surface DOS. Equation 2.8 involves the gross assumption that the tip DOS is constant.

In practice I(V)-curves can be performed on a point, a line or a grid. In line and grid measurements, initially the tip is moved to the point at which an I(V) measurement will be performed, the feedback loop is then disengaged for a period of time as the voltage is swept across some desired range. Prior to moving to the next spectroscopy point, the feedback loop is re-engaged, the tip is moved and the CCM parameters dictate the tip height at the next spectroscopy point.

2.2 Low-energy electron diffraction

The diffraction of electrons from a single crystalline sample was first observed by Davisson and Germer in 1927 [26]. The experiment was a result of an accident which resulted in a polycrystalline nickel sample being over oxidised. The subsequent prolonged high temperature annealing required to remove the surface oxide led to the formation of larger crystallites. The distribution of scattered electrons showed large variations before and after the crystal growth. It appeared that the electrons were behaving like waves incident on

a diffraction grating. Considering the lines of nickel surface atoms as lines of a diffraction grating and the electron to have a de Broglie wavelength associated with the its energy, lead to a very satisfactory agreement with the experimental scattering profiles. Such an event is depicted schematically in figure 2.4, in which wave-like electrons are back scattered from a line of atoms. This work was the first to experimentally confirm the wave-like nature of the electron hypothesised by Louis de Broglie in his PhD thesis. Hence, it represented a large step forward in the development of quantum mechanics.

2.2.1 The electron's de Broglie wavelength

The wavelength, λ, associated with an electron with momentum, p, was described as follows by L. de Broglie:

$$\lambda = h/p$$

h represent Planck's constant.
When considering an electron beam the electron's energy and momentum are related to the accelerating voltage:

$$\frac{1}{2}mv^2 = eV$$

Solving for the momentum:

$$p = mv = \sqrt{2meV}$$

Therefore, the electron's wavelength is inversely proportional to the square root of the voltage which it is accelerated through:

$$\lambda = \frac{h}{\sqrt{2meV}}$$

The wavelengths associated with voltages of 20 V and 200 V are 2.75 Å and 0.87 Å, respectively. Wavelengths of this order, which are comparable to atomic spacing, are the fundamental reason why low-energy electrons can be

diffracted by a periodic lattice. Furthermore, the inelastic mean free path of low-energy electrons ranges from 6 - 10 Å [27]. Considering we are only interested in elastically scattered electrons, the low inelastic mean free path leads to LEED being a surface sensitive technique.

2.2.2 Bragg's law

Consider a monochromatic electron beam as a plane wave at normal incidence to a uniform periodic lattice. Each of the atoms will act as scattering centres due to their high electron density. Each atom will scatter the plane wave in all directions and the back-scattered intensity will depend on the interference of the scattered waves. Let us consider a 1D chain of atoms which are separated by the lattice constant, d. Figure 2.4 depicts the condition for constructive

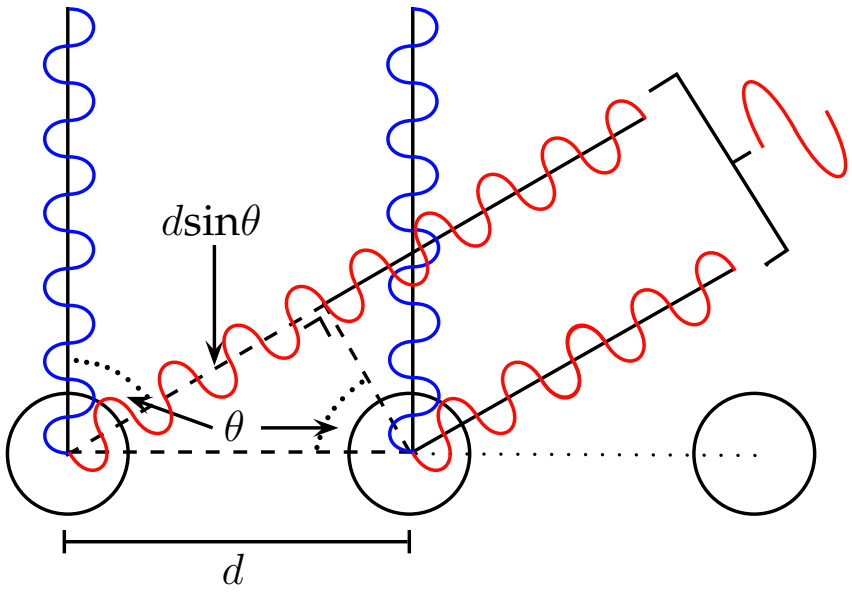

Figure 2.4: Bragg's condition for constructive interference of plane waves scattered by a 1D chain of atoms. Blue and red waves depict incident and scattered plane waves. Waves are scattered by surface atoms which are separated by the lattice constant, d. Electrons which are scattered at some angle θ will constructively interfere if their path difference is an integer times the electron's wavelength. In this example, in which constructive interference occurs, the path difference is four times the wavelength.

interference of plane waves scattered at some angle θ, by neighbouring atoms in the 1D chain. Constructive interference will occur if the path difference, $d \sin\theta$, is equal to an integer times of the wavelength, λ:

$$d \sin\theta = m\lambda \tag{2.9}$$

The important result to note is that the set of angles for which constructive interference will occur is dependent on the lattice spacing. Therefore, the diffraction pattern provides insight into the periodic lattice structure.

2.2.3 Reciprocal space

Equation 2.9 demonstrates that the sine of the scattering angle is inversely proportional to the lattice spacing:

$$\sin\theta \propto 1/d$$

Therefore, the diffraction pattern represents the reciprocal space Bravais lattice of the surface.

It is worth returning to Bragg's law, but with a different formulation, to derive Bragg's condition for constructive interference in terms of the reciprocal space lattice vectors. Let us consider two incident parallel plane waves, with wavelength λ, which are at an angle of θ_i to the surface normal. The first and second plane wave are scattered at an angle θ_s by an atom in the first and second layers, respectively[†]. The two layers are separated by the interlayer distance d. The schematic in figure 2.5 depicts such an event. Bragg's condition for constructive interference is as follows:

$$d \cos\theta_i + d \cos\theta_s = m\lambda \tag{2.10}$$

[†]For the ease of the derivation the interference of two plane waves scattered by a surface and sub-surface atom, respectively, is considered. However, the derivation is equally valid for interference of two plane waves scattered by two surface atoms.

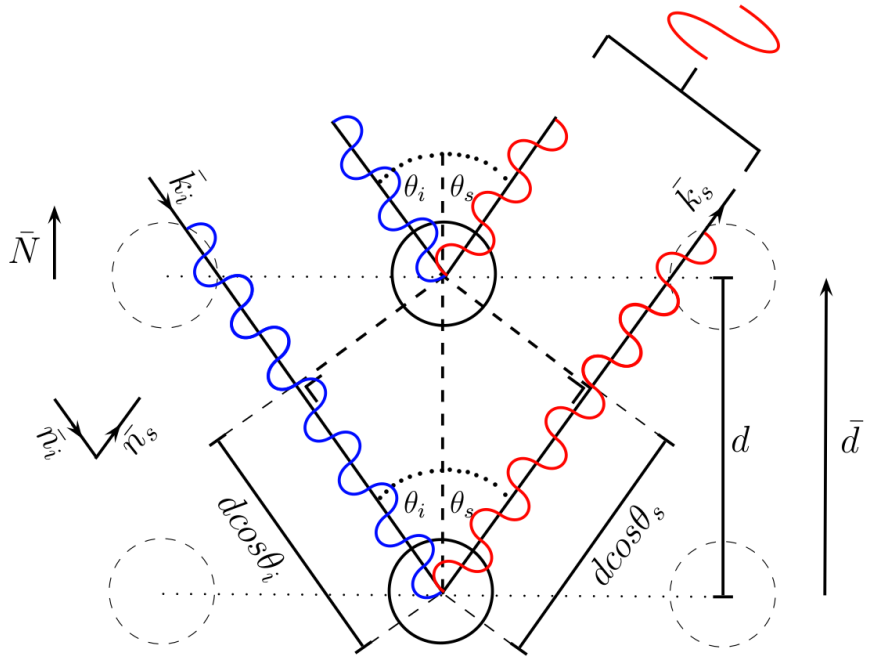

Figure 2.5: Two parallel plane waves are scattered elastically by atoms in consecutive layers of a crystal which are separated by the interlayer distance d. The incident and scattered waves forms angles relative to the surface normal, $\bar{N}$, of θ_i and θ_s, respectively. Their path difference is equal to $dcos\theta_i + dcos\theta_s$. Constructive interference will occur if the path difference is equal to some integer times the electron's de Broglie wavelength.

Taking the dot products of the interlayer vector $\bar{d}$ and the unit vectors along the incident ($\bar{n_i}$) and scattered ($\bar{n_s}$) directions yields the following:

$$\bar{n_i} \cdot \bar{d} = -|\bar{d}||\bar{n_i}| \cos\theta_i \qquad \bar{n_s} \cdot \bar{d} = |\bar{d}||\bar{n_s}| \cos\theta_s \tag{2.11}$$

Considering that $|n| = 1$, combining equations 2.10 and 2.11 gives the following expression for Bragg's condition:

$$\bar{d} \cdot (\bar{n_s} - \bar{n_i}) = m\lambda$$

Rewriting this equation in terms of the wave vector $\bar{k}$, with $\bar{k} = \frac{2\pi}{\lambda}\bar{n}$, yields:

$$\bar{d} \cdot (\bar{k_s} - \bar{k_i}) = 2\pi m$$

Finally, defining the reciprocal lattice vector as $\bar{g} = \frac{2m\pi}{\bar{d}}$, we reach Bragg's condition for constructive interference in term of the reciprocal lattice vector, $\bar{g}$:

$$(\bar{k_s} - \bar{k_i}) = \bar{g}$$

The set of vectors which satisfy this relation will give rise to constructive interference. Furthermore, the LEED pattern represents the reciprocal space lattice of the crystal.

2.2.4 Experimental apparatus

The LEED set-up, which is depicted in figure 2.6, consists of a filament, electron gun, a series of four grids and a fluorescent screen. Electrons emitted by the filament are accelerated by a voltage, V, towards the sample. The

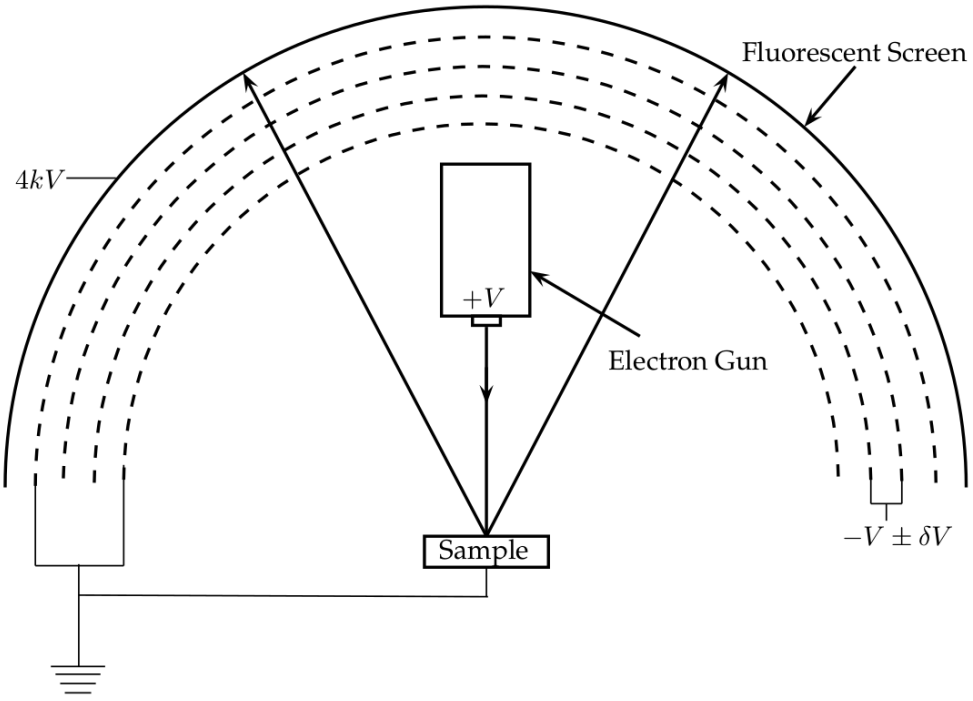

Figure 2.6: Experimental set-up of the low-energy electron diffraction apparatus. A potential difference of $-V \pm \delta V$ (V being the gun accelerating voltage) is generated between the second and third grids. This prevents undesirable inelastically scattered electrons from reaching the screen.

first and fourth grids are held at ground to eliminate stray fields. A potential difference of $-V \pm \delta V$ is generated between the second and third grids. This prevents undesirable inelastically scattered electrons from reaching the screen. The fluorescent screen, beyond the second and third grids, are held at a large positive bias in order to accelerate the transmitted elastically scattered electrons towards it.

2.3 Reflectance anisotropy spectroscopy

RAS is a non-destructive optical probe which investigates the optical anisotropy of surface region in the plane of the termination. This is achieved by illuminating the sample with near normal incidence linearly polarised light and measuring the difference in reflectance from two orthogonal surface directions:

$$\frac{\Delta r}{r} = 2\frac{(r_x - r_y)}{(r_x + r_y)} \tag{2.12}$$

The difference in the reflectance from the two orthogonal surface directions (x, y) is normalised to the total reflectance $(r_x + r_y)$. Fundamentally, the RAS signal represents the anisotropy of the electronic states along the bond axes.

Isotropic and amorphous materials as well as anisotropic materials with randomly orientated domains will not exhibit a RAS signal. RAS represents a probe which can be extremely sensitive to surface reconstructions; an anisotropic signal from a reconstructed surface of an isotropic material will be solely due to surface reconstruction and/or its influence on the near-selvedge bulk. Even in the case of (110) orientated cubic crystals, which are terminated by anisotropic planes, the stacking of orthogonal planes in the bulk sees the signal of individual planes cancel.

The initial and majority of RAS studies have been conducted on semiconducting surfaces [28–30]. The technique has been utilised to investigate semiconductor surface reconstructions and to monitor the growth of epitaxially grown semiconductor surfaces. The structure of metal absorbents on metal and semiconductor surfaces or the absorbent induced reconstruction

of the substrate has received considerable attention [28, 31–34]. RAS studies of metal oxides have received little attention, wide-bandgap ZnO [35], *ex-situ* polished $Fe_3O_4(110)$ [36] and superconducting cuprates [37] have been investigated.

2.3.1 Experimental set-up

The initial and simplest RAS setup was designed by Aspnes [38]; linearly polarised light was incident onto a rotating sample, the reflected light was passed through an analyser and subsequently a monochromator and detector. Such a set-up is not possible for many *in-situ* measurements, as the sample often cannot be rotated in the plane perpendicular to the light propagation direction. The solution is the use of a Photo Elastic Modulator (PEM). A PEM consists of a piezoelectric crystal coupled to a transparent material. Applying an alternating voltage along the polarisation axis of the piezoelectric crystal gives rise to oscillatory (in the range of 10^5 Hz) stress which is sustained in the transparent material. The transparent material is made to oscillate at its natural frequency and an oscillatory birefringence is induced. Hence, the component of the reflected beam along the oscillatory axis undergoes a time-dependent phase change while the orthogonal component remains unchanged. The RAS signal is now fully expressed as a complex quantity. At any given energy, the ratio of the second order oscillating and the time-independent intensities is directly proportional to the real part of the complex RAS quantity [28]. A standard analogue lock-in amplifier can be used to measure the second harmonic.

The standard RAS setup for *in-situ* measurements consists of a light source, polariser, window, sample, PEM, analyser, monochromator and a detector. Figure 2.7 depicts the RAS setup for *in-situ* measurements. The light emitted from a xenon lamp is linearly polarised. A strain-free fused quartz window minimises the induced birefringence in the incident and reflected beams. The sample is oriented such that its surface primitive surface unit cell directions are rotated by 45 ° with respect to the polariser orientation. The analyser and PEM oscillation axes are aligned with the samples

axis and the polarisers axis respectively. Once the reflected beam passes through the analyser it is directed to the monochromator and subsequently the detector. Two detectors are utilized, an InGaAs detector for energies between 0.8 - 1.2 eV and a Si detector from 1.2 - 5.5 eV. *Ex-situ* measurements follow a similar design. However a larger spectral range is realised using a Bentham TMc300 triple grating monochromator and three individual detectors (InAs, InGaAs and Si).

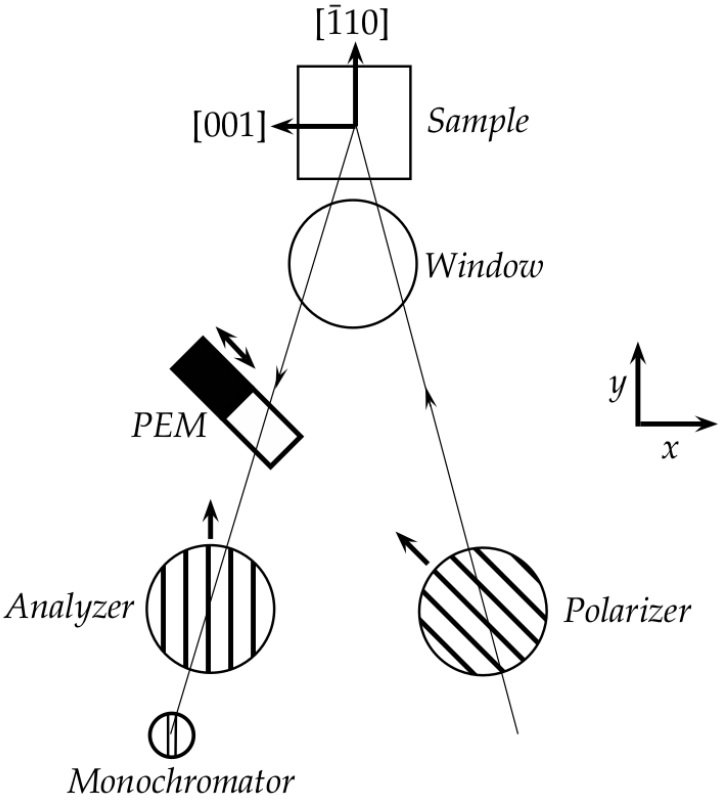

Figure 2.7: Depicted is the *in-situ* RAS set-up used in this work. Light from a xenon lamp is polarised in the x - y direction. This linearly polarised light enters the UHV chamber via a strain-free quartz window and subsequently is reflected by the sample. The primitive unit vectors of the surface are orientated at 45 ° with respect to the polarisation direction. In this schematic the surface vectors correspond to a (110) terminated cubic material. The reflected beam passes through a PEM and subsequently an analyser whose oscillation and polarisation directions are x - y and y, respectively. Finally, the beam enters the monochromator and detector.

2.3.2 The three-phase model

The reflectance anisotropy can be related to the dielectric function of the bulk and surface region. The dielectric tensor fundamentally describes the interaction of the light with a media. McIntyre and Aspnes developed the three-phase model to determine the change in reflectance when a thin-film was grown on a bulk substrate [39]. The three phases are the ambient (1), a thin-film (2) of thickness d and the substrate or bulk (3), which the thin-film is grown on. Considering the Fresnel reflections, and considering a thin-film with depth far smaller than the light wavelength, the difference between the total reflection when a thin-film of thickness d is present ($R(d)$) and the total reflection when no thin-film is present ($R(0)$), normalised to $R(0)$ is given by [39]:

$$\frac{\Delta\tilde{R}}{\tilde{R}} = \frac{\tilde{R}(d) - \tilde{R}(0)}{\tilde{R}(0)} = \frac{4\pi d\tilde{n}_1 i}{\lambda}\frac{\tilde{\epsilon}_3 - \tilde{\epsilon}_2}{\tilde{\epsilon}_3 - \tilde{\epsilon}_1} \tag{2.13}$$

Here $\tilde{\epsilon}_i$ represents the complex dielectric function of the three phases labelled above. In real systems the dielectric function does not abruptly change at the bulk–thin-film interface. Equation 2.13 can equally be defined by replacing the difference between the bulk and thin-film dielectric functions with the gradient of the dielectric function from the bulk–thin-film interface to the thin-film–ambient interface ($\Delta\tilde{\epsilon}$) [39]:

$$\frac{\Delta\tilde{R}}{\tilde{R}} = \frac{\tilde{R}(d) - \tilde{R}(0)}{\tilde{R}(0)} = \frac{4\pi d\tilde{n}_1 i}{\lambda}\frac{\Delta\tilde{\epsilon}}{\tilde{\epsilon}_3 - \tilde{\epsilon}_1} \tag{2.14}$$

The three-layer model was later used by Aspnes [38] to describe the difference in reflectance of linear p-polarised light from two orthogonal directions perpendicular to the surface normal:

$$\frac{\Delta\tilde{R}}{\tilde{R}} = 2\frac{\tilde{R}_x - \tilde{R}_y}{\tilde{R}_x + \tilde{R}_y} = \frac{4\pi di}{\lambda}\frac{\Delta\tilde{\epsilon}}{\tilde{\epsilon}_b - 1} \tag{2.15}$$

With $\Delta\tilde{\epsilon} = \tilde{\epsilon}_x - \tilde{\epsilon}_y$. $\tilde{\epsilon}_x$ and $\tilde{\epsilon}_y$ are the average dielectric functions in the surface region (thin film in the above discussion) along the orthogonal surface

directions x and y. $\tilde{\epsilon}_b$ is the dielectric function of the underlying bulk and $\tilde{\epsilon}_1$ and $\tilde{n}_1$ in equation 2.14 are replaced with unity representing the vacuum.

An extension of the three-phase model is the derivative model which relates the reflectance anisotropy to the first energy derivative of the bulk dielectric function ($\tilde{\epsilon}_b$). The reflectance anisotropy is expected to resemble the first energy derivative of $\tilde{\epsilon}_b$ if the orthogonal components of the surface regions dielectric function, $\tilde{\epsilon}_x$ and $\tilde{\epsilon}_y$, are similar in magnitude but differ slightly in broadening and/or energy shifts [40]. For example, in cubic optically isotropic materials, this shift produces a non-zero cancellation of optical transitions which are orthogonal and would otherwise cancel. Such a situation is depicted in figure 2.8. The difference of states slightly shifted into energy is analogous to the first energy derivative of $\tilde{\epsilon}_b$. Replacing $\Delta\tilde{\epsilon}$ with $\frac{\mathrm{d}\tilde{\epsilon}_b}{\mathrm{d}E}$ in equation 2.15 and extracting the real component (experimentally the real part of the complex RAS signal is measured) by taking the complex conjugate, we obtain the following expression:

$$Re\left(\frac{\Delta\tilde{R}}{\tilde{R}}\right) = \frac{4\pi d}{\lambda}\frac{(\epsilon^{'}-1)\frac{\mathrm{d}\epsilon^{''}}{\mathrm{d}E} - \epsilon^{''}\frac{\mathrm{d}\epsilon^{'}}{\mathrm{d}E}}{(\epsilon^{'}-1)^2+\epsilon^{''2}} \tag{2.16}$$

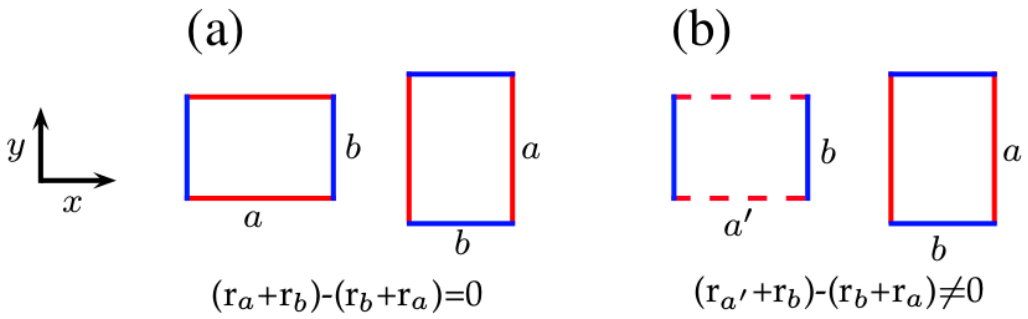

Figure 2.8: Depicted are consecutive (110) planes of a cubic material. (a) The signal from an individual anisotropic plane is cancelled by the signal from an underlying identical, but orthogonal, plane. (b) If the surface induces a small modification of optical transitions, orthogonal transitions will no longer cancel, and a net signal remains. Here the signal is due to the difference in bulk-like and slightly modified, and otherwise identical, bulk-like transitions (a′-a). This is analogous to the first energy derivative of the bulk dielectric function.

With $\tilde{\epsilon}_b = \epsilon^{'} + i\epsilon^{''}$. One must keep in mind that this expression is only valid for the transitions in the vicinity of a single critical point. Optical anisotropies originating from the modification of different states can produce signals of different width, sign and magnitude.

The derivative model has been applied to metal and semiconductor surfaces. The d-band is narrowed at the Cu(110) surface due to a reduced number of bonds. The number of dangling bonds along the orthogonal $[1\bar{1}0]$ and [001] surface directions are nonequivalent. Hence, the d-band narrowing and the related energy shift is anisotropic and generates a derivative-like RAS signal [41]. In the case of isotropic silicon, derivative-like structures are induced by mechanically applying strain. The magnitude of the induced RAS signal varies linearly with the applied stress [42].

2.3.3 Drude model

It has been demonstrated that RAS signals can originate from anisotropic conductance. This was first realised in the case of metallic islands on semiconducting substrates [43]. The experimental RAS signal showed good agreement with the calculated RAS signal which considered anisotropic Drude-like dielectric functions within the three-layer model.

The dielectric function of a free-electron gas can be described using the Drude-Lorentz formulas for an oscillator with eigen frequency $\omega_0 = 0$:

$$\epsilon^{'} = 1 - \frac{{\omega_p}^2}{\omega^2 + \gamma^2}, \qquad \epsilon^{''} = \frac{{\omega_p}^2 \gamma}{\omega(\omega^2 + \gamma^2)}$$

where $\tilde{\epsilon} = \epsilon^{'} + i\epsilon^{''}$ and γ is the scattering rate. In the Drude theory, ω_p is given by $\omega_p^2 = \mathrm{N}_c \mathrm{e}^2 / \mathrm{m}_e \epsilon_0$, were N_c is the free-electron density and m_e the free-electron mass. Although originally derived for non-interacting electrons in 3D, the Drude dielectric function nevertheless agrees well with the measured dielectric function of bulk metals.

The RAS quantity is calculated within the framework of the three-phase model from equation 2.14 whereby $\Delta\tilde{\epsilon}$ is the difference between the orthogonal Drude dielectric functions in the surface region. Optical anisotropy can

arise from anisotropic effective masses (and hence plasma frequencies) and/or anisotropic scattering rates.

2.4 X-ray photoelectron spectroscopy

The underlying principle of XPS and Ultraviolet Photoelectron Spectroscopy (UPS) is the photoelectric effect, which is depicted in figure 2.9. Heinrich Hertz discovered the effect in 1887 and Albert Einstein was awarded the Nobel prize for its explanation in 1905. The photoelectric effect represents an important milestone in modern physics. The energy of electrons emitted from an illuminated metal surface was observed to increase only when the light's frequency was increased. Increasing the amplitude only increased the number of emitted electrons. Furthermore, electron emission was only observed if the light's frequency was above some threshold value. These observations were

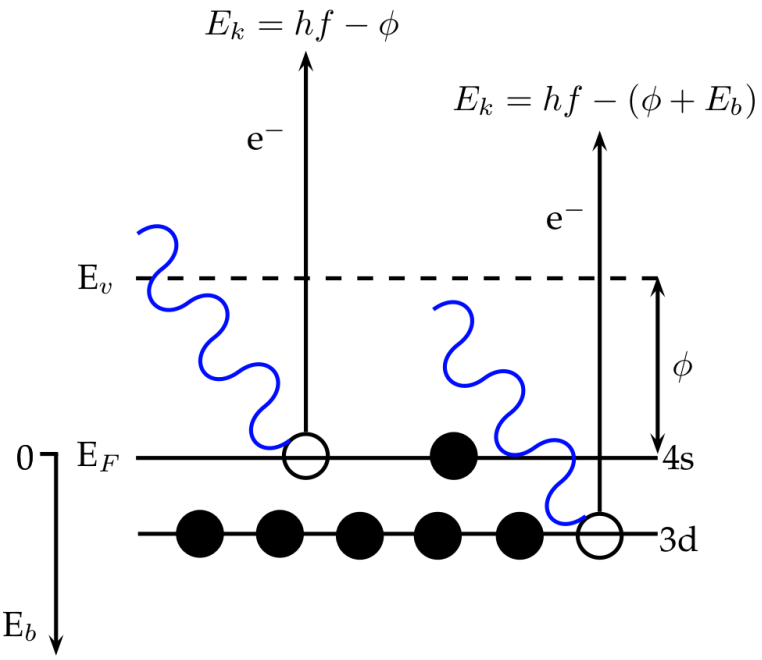

Figure 2.9: Schematic of the photoelectron effect taking iron as an example. At the Fermi level the kinetic energy of photoelectrons is the difference between the photon energy, hf, and the workfunction, ϕ. For electrons beneath the Fermi level, the binding energy is subtracted from the kinetic energy.

directly contradictory to Maxwell's equation. Einstein solved this problem by describing light as individual quanta - in this case the photon - which had a discrete amount of energy. Individual photons are absorbed by the electrons, and if the photon energy is greater than the metal's work function, electron emission occurs. The energy of a photoelectron, which prior to photon absorption has a binding energy E_B relative to the Fermi level, is as follows:

$$E_k = hf - (\phi_m + E_B)$$

The electron's kinetic energy can be directly related to the binding energy of the orbital it resided in prior to photoemission.

XPS and UPS involves a monochromatic, collimated beam of X-rays or UltraViolet (UV) light incident on a samples surface. An electron energy analyser allows for the flux of photoemitted electrons at specific kinetic energies to be measured by a spectrometer. XPS can identify elements and their valence state. Furthermore, the cross section for absorption of photons at some energy increment depends on the number of electrons available to absorb such photons, hence, XPS can provide elemental ratios. UPS can provide information about the valence band states.

The incident x-ray flux can induce the emission of Auger electrons. Although this phenomena can provide important information about the electronic orbitals an Auger electron's energy is not related to the binding energy. Hence, peaks in XPS spectra due to Auger processes need to be attributed as such.

Due to the short inelastic mean free path of electrons XPS & UPS represent surface sensitive techniques. In this work, XPS and UPS measurements were performed using a laboratory-based Omicron MultiProbe-XPS system using monochromated Al-K X-rays ($h\upsilon = 1486.7\,eV$), a He(I) UV-lamp and an EA125 analyzer.

2.5 Density functional theory

DFT is a computational quantum mechanics modelling method used to perform calculations of materials' physical and chemical properties on the atomic scale. It is an *ab-initio* approach which makes use of reasonable approximations (which will be outlined in this chapter) to perform calculations, which would otherwise require an unreasonable amount of memory and time.

Determining physical and chemical properties of a system requires solving the Schrödinger's equation for all the electrons and nuclei of the system:

$$\hat{H}\Phi(\vec{R}_a;\vec{r}_i) = \varepsilon\Phi(\vec{R}_a;\vec{r}_i)$$

$\hat{H}$, ε and Φ represent the Hamiltonian, Hamiltonian energy and the system's wavefunction. R_a and r_i correspond to the nuclei and electrons' positions, respectively. The Hamiltonian contains terms describing electron and nuclear motion and terms describing electron-nuclei, electron-electron and nuclei-nuclei interactions:

$$\hat{H} = -\sum_i \frac{\hbar^2}{2m}\nabla_i^2 - \sum_\alpha \frac{\hbar^2}{2M}\nabla_\alpha^2 - \frac{e^2}{2}\sum_{i,\alpha}\frac{Z_\alpha}{|\vec{r}_i - \vec{R}_\alpha|} + \frac{e^2}{2}\sum_{i,j}\frac{1}{|\vec{r}_i - \vec{r}_j|} + \frac{e^2}{2}\sum_{\alpha,\beta}\frac{Z_\alpha Z_\beta}{|\vec{R}_\alpha - \vec{R}_\beta|}$$

m, M and Z correspond to the electron mass, nuclear mass and nuclear atomic number. A system which contains N electrons and M nuclear has $3(N+M)$ variables. For even the simplest of systems, this results in a problem which is impossible to solve in practice.

The Born-Oppenheimer (BO) approximation allows for the simplification of the Hamiltonian. Considering Newton's third law, the electronic momenta change, mv_i, is equal and opposite to the nuclear momenta change, MV_α, during an interaction between them. Hence, the ratio of the velocities is equal to the inverse ratio of the masses, $\frac{v_i}{V_\alpha} = \frac{M}{m} = 1836$. The BO approximation states that the kinetic energy of the 'slow' nuclei can be ignored. Furthermore, on the timescale of the nuclear motion the electrons will rapidly relax

into their ground state. Therefore, we can assume that no transitions occur due to the nuclear motion. The nuclear positions, R_α, enter the Hamiltonian as external parameters and are therefore decoupled from the electronic dynamics. The electrons experience a constant external potential.

Applying the wavefunction to the Hamiltonian and describing the wavefunction of the system in terms of Slater determinants, which account for the electron's antisymmetric nature, leads to the following expression:

$$\begin{aligned} < \Phi_n|\hat{H}|\Phi_n >= & \frac{-\hbar^2}{2m}\sum_i \int \mathrm{d}^3 r \phi_i^*(\vec{r})\nabla^2\phi_i(\vec{r}) \\ & -\frac{e^2}{2}\sum_i \int \mathrm{d}^3 r \phi_i^*(\vec{r_i})\phi_i(\vec{r_i}) \sum_{i,\alpha}\frac{Z_\alpha}{|\vec{r_i}-\vec{R}_\alpha|} \\ & +\frac{e^2}{2}\sum_i \int \mathrm{d}^3 r \phi_i^*(\vec{r})\phi_i(\vec{r}) \sum_{i\neq j}\int \mathrm{d}^3 r' \frac{\phi_j^*(\vec{r'})\phi_j(\vec{r'})}{(\vec{r}-\vec{r'})} \\ & +\frac{e^2}{2}\sum_{i,j}\delta_{\chi_i\chi_j}\int \mathrm{d}^3 r \phi_i^*(\vec{r})\phi_i(\vec{r}) \int \mathrm{d}^3 r' \frac{\phi_j^*(\vec{r'})\phi_j(\vec{r'})}{(\vec{r}-\vec{r'})} \end{aligned} \tag{2.17}$$

The first term accounts for the kinetic energy of the electrons. Bare in mind that, based on the BO approximation, the nuclei motion is omitted. The second term describes the energy due to electron's electrostatic interaction with the static nuclei (external potential term). The third term describes electron-electron electrostatic interaction (Hartree term). Finally, the fourth term accounts for repulsion of like-spins (Pauli exclusion principle). Consid-

ering that $n(r) = \sum_i \phi_i^*(\vec{r})\phi_i(\vec{r})$ equation 2.17 can be rewritten as follows:

$$\begin{aligned} < \Phi_n|\hat{H}|\Phi_n >= \frac{-\hbar^2}{2m}\sum_i \int \mathrm{d}^3 r \phi_i^*(\vec{r})\nabla^2\phi_i(\vec{r}) \\ - \int \mathrm{d}^3 r n(\vec{r})V_{ext}(\vec{r}) \\ + \int \mathrm{d}^3 r n(\vec{r})V_H(\vec{r}) \\ + \frac{e^2}{2}\sum_{i,j}\delta_{\chi_i\chi_j}\int \mathrm{d}^3 r \phi_i^*(\vec{r})\phi_i(\vec{r})\int \mathrm{d}^3 r' \frac{\phi_j^*(\vec{r'})\phi_j(\vec{r'})}{(\vec{r}-\vec{r'})} \end{aligned}$$

Here, $V_{ext}(\vec{r}) = \frac{e^2}{2}\sum_{i,\alpha}\frac{Z_\alpha}{|\vec{r}_i - \vec{R}_\alpha|}$ and $V_H(\vec{r}) = \frac{e^2}{2}\int \mathrm{d}^3 r' \frac{n(r')}{(\vec{r}-\vec{r'})}$. The Hartee term, $V_H(\vec{r})$, can be calculated from the full charge density. This leads to the key idea of DFT: each of the electron wavefunctions, $\phi_i(r)$, does not need to be solved for. Instead, it is sufficient to solve for the full charge density, $n(\vec{r})$, directly. This was first proposed by Hohenberg and Kohn in 1964 [44].

Hohenberg and Kohn's theorems [44] are as follows:

1. The external potential, V_{ext}, is uniquely determined by the ground state density, $n(\vec{r})$. There cannot exist two potentials which give the same $n(\vec{r})$. All ground state properties are uniquely determined by $n(\vec{r})$.

2. An energy functional, $E(n)$, exists, such that the exact ground state is the minimum of $E(n)$. Furthermore, the ground state density minimises $E(n)$.

The second theorem can be expressed as follows:

$$\begin{aligned} E_{GS} = \min_n[E[n]] = \min_n[< \phi|\hat{T} + \hat{V}_{ee} + \hat{V}_{ext}|\phi >] \\ = \min_n[F[n] + \int \mathrm{d}^3 r n(\vec{r})V_{ext}(\vec{r})] \\ F[n] =< \phi|\hat{T} + \hat{V}_{ee}|\phi > \end{aligned}$$

$F[n]$ (density functional including electron kinetic and electron-electron interaction terms) is uniquely determined by the interacting particles, and does not depend on the external potential. Furthermore, by the first theorem, the density which minimises $F[n]$ uniquely determines the external potential.

Solving for the exact form of the density functional is unpractical, it would require a constrained search over all of the electrons within the system. In 1965, Walter Kohn and Lu Jeu Sham developed a method to determine the ground state density by solving a non-interacting problem, with the same density and ground state energy as the interacting case [45]. The energy functional which is minimised to obtain the ground state energy can be expressed as follows:

$$E[n] = \hat{T}[n] + \int \mathrm{d}^3 r n(\vec{r}) \Big(V_{ext}(\vec{r}) + V_H(\vec{r}) \Big) + \tilde{E}_{xc} \tag{2.18}$$

$\tilde{E}_{xc}$, the "exchange-correlation" term, contains all interactions not included in the electron-electron term ($V_H(\vec{r})$). The exact form of the kinetic energy term is unknown. However, the kinetic energy term for a non-interacting case ($\hat{T}_0$[n]) is known exactly. Equation 2.18 is written in terms of the kinetic energy of the non-interacting case:

$$E[n] = \hat{T}_0[n] + \int \mathrm{d}^3 r n(\vec{r}) \Big(V_{ext}(\vec{r}) + V_H(\vec{r}) \Big) + E_{xc}$$

Here, $E_{xc} = \tilde{E}_{xc} + (T[n] - T_0[n])$. Additionally, the energy functional of the non-interacting case is as follows:

$$E_0[n] = \hat{T}_0[n] + \int \mathrm{d}^3 r n(\vec{r}) V_{eff}(\vec{r})$$

The effective potential, V_{eff}, is chosen such that the ground state charge density of the non-interacting system is equal to that of the interacting one.

At the ground state charge density, the rate of change of the energy functional with respect to the charge density is zero. By definition, the effective potential of the non-interacting system yields the same ground state

charge density as the interacting system. Hence:

$$\frac{\delta E_0[n(r)]}{\delta n(r)}\Big|_{n_{GS}(r)} = \frac{\delta E[n(r)]}{\delta n(r)}\Big|_{n_{GS}(r)} = 0$$
$$\therefore V_{eff}(\vec{r}) = V_{ext}(\vec{r}) + V_H(\vec{r}) + V_{xc}(\vec{r})$$

Here, $\frac{\delta E_{xc}}{\delta n(r)} = V_{xc}[n(r)]$. The ground state of the interacting system can be found by solving for the ground state of the non-interacting problem in a self-iterative fashion.

What remains to be chosen is an approximation for the exchange-correlation term. This term can be split into two independent exchange and correlation components. The exchange component is due to Pauli's exclusion principle and the correlation component takes into account effects which are not accounted for in equation 2.17. The two commonly utilised approximations for the exchange-correlation term are the Local Density Approximation (LDA) and the General Gradient Approximation (GGA). LDA approximates the electron density to be homogeneous:

$$E_{xc}[n] = \int \mathrm{d}^3 r n(\vec{r}) V_{xc}[n(\vec{r})]$$

With $V_{xc} = V_x + V_c$. The exchange component is known exactly from equation 2.17 and the correlation can be numerically calculated by quantum Monte-Carlo methods [46]. GGA additionally considers the gradient of the electron density:

$$E_{xc}[n] = \int \mathrm{d}^3 r n(\vec{r}) V_{xc}[n(\vec{r}), \nabla n(\vec{r})]$$

The LDA has been proved to be sufficient for calculations of band structure and total energy in solid state physics [47]. However, LDA is not widely used in quantum chemistry: the approximation does not provide sufficiently accurate results to quantitatively discuss chemical bonds in molecules. GGA provides an improved approximation to calculate chemical bonds. However, GGA is known to underestimate lattice constants.

The core idea of DFT is to consider the density of the entire system, and calculate all quantities from this density. Within this framework, each particle-particle interaction doesn't need consideration. One issue that arises from DFT is that a single particle, for example an electron, is influenced by the charge density in its neighbourhood. However, this electron is part of this density. This leads to electron self-interaction and delocization, which gives rise to a non-physical homogeneous charge density [48]. To account for this, an energetic penalty is applied to the electrons in the system [48]. This parameter, termed U, is often used as a free parameter to fit an experimental observable. The questions arises: what quantity should the calculation be fit with respect to. In this work the U parameter for Fe_3O_4 has been taken from work conducted by Anisimov *et al.* [49, 50], who choose a U parameter to fit the experimental magnetic moments. It is noted, that the best approach is to explicitly calculate the U parameter, in a self-consistent manner, for the given system (see for example [51]).

Chapter 3

Iron Oxides & Perovskites

3.1 Iron oxides

Iron and oxygen are among the four most abundant elements on the planet. Due to iron's wide range of available oxidation states, it forms a number of different compounds with oxygen. Under ambient conditions iron oxidises to form rust which consists of hydrated α - Fe_2O_3. This iron oxide, known as hematite, forms a hexagonal unit cell, which differs from the other naturally occurring iron oxides which are cubic. Magnetite (Fe_3O_4) forms when iron is oxidised at high temperatures. Maghemite (γ - Fe_2O_3) is very similar in structure to magnetite, it is essentially magnetite with cation vacancies. It can be formed by the oxidation of magnetite and can be transformed into hematite at high temperatures. Wüstite ($Fe_{1-x}O$) can be formed by the reduction of any of the aforementioned iron oxides. The temperature-pressure phase diagram of the iron oxides is presented in figure 3.1 [52].

Iron oxides exhibit a variety of magnetic and electronic properties. Fe_3O_4 and γ - Fe_2O_3 are ferrielectric and exhibit the largest magnetisation among minerals. On the other hand, $Fe_{1-x}O$ and α - Fe_2O_3 are antiferromagnetic. The oxides' electric properties are also diverse; γ - Fe_2O_3 is insulating, α - Fe_2O_3 is a poor conductor, $Fe_{1-x}O$ has a reasonably high conductivity, and Fe_3O_4 is metallic.

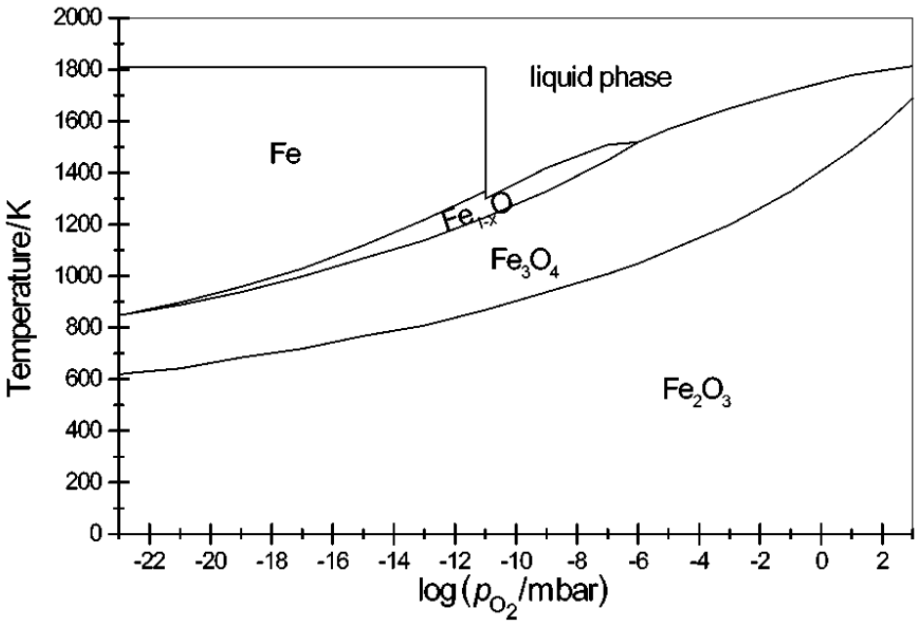

Figure 3.1: Calculated temperature-pressure phase diagram of the iron oxides taken from [52].

Iron oxides find industrial relevance in a variety of fields [53]. They display a number of attributes desirable for pigments: a range of colours, highly resistant to acids and bases and can be used in water and organic-based paints. Maghemite finds use as a magnetic pigment in electronic recording devices. Although magnetite has a higher magnetisation, maghemite is cheaper and more chemically and magnetically stable. Hematite is used as a starting material in the production of hard ferrites, for example, barium and strontium ferrites. Finally, magnetite and hematite are used as catalysts for several industrial syntheses such as the synthesis of ammonia [2], methanol [3], the water-gas shift reaction [4] and the Fischer-Tropsch synthesis [53].

3.1.1 Magnetite, Fe_3O_4

Magnetite forms upon the slow cooling of silicate material high in iron and magnesium content. This cooling is required to be sufficiently slow such that

small crystals of magnetite can agglomerate. Magnetite can also form during the metamorphism of impure iron-rich limestone.

As the story goes, the magnetic material lodestone, which is natural magnetised magnetite, was discovered roughly 4000 years ago in an area of modern day Turkey called Magnesia which was inhabited by Magnates. Magnetite and the class of material which produce a magnetic field, i.e magnets, were named after the Magnates. It is believed that lodestone was the first discovered magnet. Furthermore, it is a rare example of a strongly magnetic, naturally occurring mineral and is utilised by organisms for navigation [54].

Fe_3O_4 exhibits an extremely interesting range of properties such as half-metallic conductivity, high Curie temperature ($858\,K$) ferrimagnetism and undergoes a Verwey transition (simultaneous electronic and structural phase change) at $\sim 120\,K$. These properties have lead to extensive research on the possibility of utilising magnetite in applications such as spin sources in spintronic devices [55], magnetic storage of information [56] and magnetic sensor applications [57]. Magnetite is an industrially relevant material; it is utilized in the cores of electromagnets, microwave resonant circuits, computer memory cores and in high density magnetic recording media [53].

The structure of magnetite, whose unit cell is depicted in figure 3.2, is that of an inverse spinel structure [58] with a lattice constant of 0.8398 nm. Iron atoms occupy both octahedral (denoted Fe_{oct}) and tetrahedral (denoted Fe_{tet}) coordination with a ratio of 2:1. The oxygen atoms form a face-centred cubic (FCC) sublattice.

Fe_{oct} atoms are formally divalent or trivalent with a ratio of 1:1, while Fe_{tet} atoms are all formally trivalent. Taking into account the valency the formula unit can be written as $Fe^{3+}_{tet}Fe^{2+}_{oct}Fe^{3+}_{oct}O^{-2}_4$. Magnetite has an electrical conductivity of around $250\,\Omega^{-1}\,cm^{-1}$ [59][60] at room temperature and is predicted to be a half-metallic conductor, which means the electrons at the Fermi level are 100% spin polarised. This half-metallicity has been predicted by DFT calculations [61] and observed experimentally by spin-resolved photoelectron spectroscopy [62]. The majority spin channel is semiconducting, while the minority spin channel is conducting. The Fermi level is based at the 3d band of the octahedral iron, and hence, the conductivity arises from the

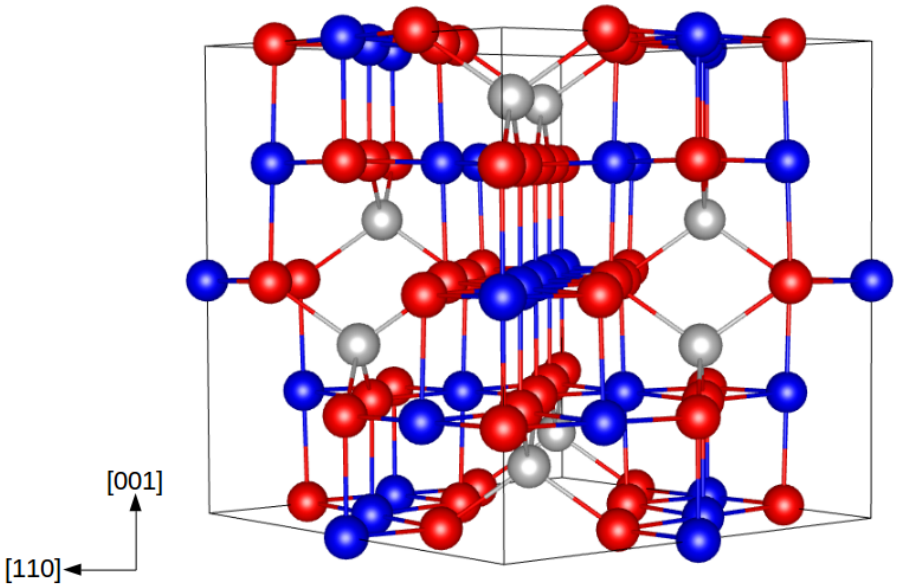

Figure 3.2: Magnetite unit cell. Oxygen, Fe_{oct} and Fe_{tet} are coloured red, blue and silver, respectively. The (110) plane is approximately perpendicular to the page.

continuous hopping of delocalised electrons between divalent and trivalent Fe_{oct} sites [63][64].

Néel used magnetite to demonstrate his theory of ferrimagnetism. A ferrimagnetic material is antiferromagetic, however the magnitude of the up and down moments differ, and hence, a net magnetisation remains. Néel proposed that the octahedral and tetrahedral sites of magnetite were antiferromagnetically aligned, hence, the trivalent octahedral and tetrahedral magnetic moments cancel. Therefore, the magnetism arises solely from the octahedral divalent site. Divalent iron has a valence state of $3d^6$. Crystal field theory predicts that the d-level will split as depicted in figure 3.3. There are three possible configurations of the six 3d Fe_{oct} electrons which are depicted in figures 3.3(b), 3.3(c) and 3.3(d). Magnetite has a magnetic moment per formula unit of $4\,\mu_B$, and therefore the configuration depicted in figure 3.3(d) is in agreement with experiment. This configuration is energetically favourable due exchange splitting of $\sim$3.5 eV which is greater than the

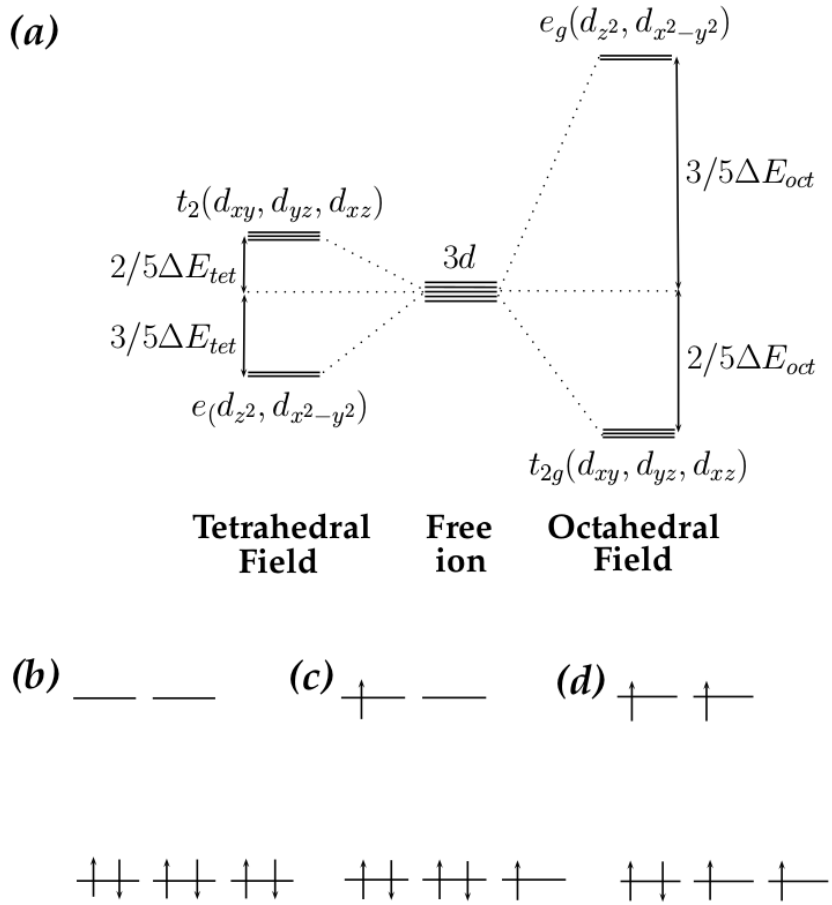

Figure 3.3: (a) The five energetically equivalent d-levels of the free ion are split by the tetrahedral and octahedral crystal fields. The Fe_{oct} site is further split by the asymmetry of the octahedral cell (not shown here). (b), (c) and (d) illustrate the possible configurations that the six valence electrons of the divalent octahedral site can occupy. The configuration in (d) is in agreement with the experimentally observed magnetic moment of $4\,\mu_B$ per formula unit.

crystal field splitting (ΔE_{CF} in figure 3.3(a)). Therefore, the five majority 3d levels have are lower in energy than all of the minority levels and are filled first (Hund's rule).

In 1926 Parks and Kelley discovered, via heat capacity measurements, that magnetite exhibited a phase change at ∼120 K [65]. The phase change lead to a reduction in symmetry from cubic to monoclinic [66]. The monoclinic phase space group is Cc and its unit cell has dimensions $\sqrt{2}\mathrm{a}_c \times \sqrt{2}\mathrm{a}_c \times 2\mathrm{a}_c$ relative to the $\mathrm{Fd}\bar{3}\mathrm{m}$ cubic inverse spinel unit cell.

In 1939, Verwey discovered that this phase transition is accompanied by a drop in the conductivity by two orders of magnitude [59]. The class of transition in which both a structural and electronic change occurs are termed Verwey transitions, and the temperature at which the transition occurs is called the Verwey transition temperature (T_V). $\mathrm{Fe_{oct}}$ atoms are considered as either divalent or trivalent at room temperature. However, due to their delocalised nature their formal oxidation state is 2.5+. Verwey proposed that below T_V these electrons became localised, with an oxidation state of either 2+ or 3+ [59]. Verwey believed this phenomenon, known as charge freezing which localises the electrons, leads to the sharp drop in conductivity and a structural change.

Although the Verwey transition was discovered nearly 80 years ago, the mechanism behind the proposed charge ordering and its relationship with the structural phase change is still debated. For the most part charge freezing has been accepted and research has focused on determining the nature of the charge ordering. Several models have been proposed [67–71]. Alternatively, Pasternak *et al.* [72] proposed that the charge ordering is not confined to the octahedral sites; charge is transferred from the tetrahedral to octahedral sites, which results in the tetrahedral and octahedral sites being divalent and trivalent, respectively. Some studies have entirely refuted the occurrence of charge ordering; lattice distortions have been suggested to lead to an opening of a gap at the Fermi level [73] and García *et al.* argued that there is no strong experimental evidence that charge ordering occurs at all [74]. Recently, Liu and Di Valentin have preformed hybrid DFT+U calculations, which show that there is charge disproportionation (0.3 e) between two evenly occupied

Fe_{oct} sites in the high temperature phase, leading to a small bandgap (0.2 eV) [75]. This would suggest that the Verwey transition in a semiconductor-to-semiconductor transition. Clearly, the remains no clear consensus on the nature of the Verwey transition within the community.

3.1.2 Maghemite, γ - Fe_2O_3

Maghemite's name originates from it similarities to both magnetite and hematite. The iron to oxygen ratios of hematite and maghemite are identical, however their crystal structures are certainly not. The structure of maghemite is very similar to that of magnetite, both being inverse spinel. However, maghemite's space group is $P4_332$, compared to the $Fd\bar{3}m$ space group of magnetite. The octahedral sites of γ - Fe_2O_3 are all 3+. This is achieved by introducing Fe_{oct} vacancies. If we consider magnetite's formula unit - $Fe^{3+}_{tet}(Fe^{2.5+}_{oct})_2(O^{-2})_4$ - it is clear that the oxygen atoms accept eight electrons. Rewriting this formula for maghemite with Fe_{oct} vacancies and with the remaining Fe_{oct} sites trivalent we obtain: $Fe^{3+}_{tet}(V_{Fe_{oct}})_x\ (Fe^{3+}_{oct})_{2-x}(O^{-2})_4$. Oxygen atoms now gain their 8 electrons from the trivalent tetrahedral and octahedral sites, that is: $8 = 3 + 3\,(\,2 - x\,) \therefore x = 1/3$. Therefore, to form maghemite from magnetite, one sixth of the Fe_{oct} sites are vacant and the remainder are trivalent. The vacancies are predicted to be fully ordered [76].

Like Fe_3O_4, γ - Fe_2O_3 is a ferrimagnet, with a magnetic moment of $3.\dot{3}\,\mu_b$ per formula unit. Its high Curie temperature of $\sim$950 K has seen maghemite utilized in recording media [53]. Due to the absence of 2+ octahedral sites, hopping is not possible and maghemite is insulating. DFT+U calculations, which reproduce the experimentally observed gap of $\sim$2 eV, predict that the gap is different for each spin orientation [76], making γ - Fe_2O_3 potentially useful as a spin-filter in spintronic devices.

Maghemite can be formed by oxidising magnetite. In ambient conditions the surface region of magnetite is transformed into maghemite, although this is a very slow process [43]. It is metastable against the formation of hematite due to the oxygen sublattices of maghemite and hematite being FCC and Hexagonal Close-Packed (HCP), respectively.

3.1.3 Hematite, α - Fe_2O_3

Hematite, commonly known as rust, is the most abundant of the iron oxides. It can be formed from γ - Fe_2O_3 at elevated temperatures. α - Fe_2O_3, with its hexagonal ($R\bar{3}c$) unit cell ($a = 0.5034\,nm$ and $c = 1.375\,nm$), is the only iron oxide whose unit cell is not cubic. The oxygen atoms form a HCP sublattice and two thirds of the octahedral positions are occupied by Fe^{3+} cations. Along the c-axis the stacking sequence is O-Fe-Fe repeating.

3.1.4 Wüstite, $Fe_{1-x}O$

Wüsite crystallises into a rocksalt (Fm3m) structure (the lattice constant ranges from 0.428 - 0.430 nm) with oxygen and iron forming FCC sublattices. $Fe_{1-x}O$ is always defective in reality, the common defect is a Fe^{3+} cation which resides in a tetrahedral position [77]. This interstitial is accompanied by iron vacancies: the four neighbouring Fe^{2+} sites are vacated. The defects can cluster to form regions with up to four interstitials and thirteen vacancies [77]. Wüsite can be formed at high temperatures in heavily reducing conditions from any of the other iron oxides [52]. If $Fe_{1-x}O$ is quenched after being exposed to such conditions it can exist as a metastable phase. On the other hand, if it is cooled slowly, it will form Fe and Fe_3O_4.

$Fe_{1-x}O$ displays reasonably good conductivity [78], the conductivity increases with the defect density [79]. At room temperature wüstite is paramagnetic and below its Néel temperature of 200 K it exhibits antiferromagnetism. The defects also affect wüstite's magnetic and electrical properties [80].

3.2 Perovskites

Calcium titanate, $CaTiO_3$, was discovered in the Ural mountains in 1839, and was named "perovskite" after the Russian mineralogist Lev Perovski. Further ABX_3 materials were subsequently discovered and their common crystal structure was termed the perovskite structure. A and B are cations of different sizes, while the X anion is for the most part oxygen, although

perovskites with N, F, or I anions exist. Bridgmanite, (Fe,Mg)SiO_3, is the most abundant solid phase within the earth's interior, however it is only stable at high temperature and pressure and so is not found at the earth's surface. The unit cell is very flexible and perovskites crystallise into structures ranging from cubic to hexagonal. Furthermore, inverse perovskites can be synthesised which exhibit an A_3BX formula. The ideal perovskite structure, illustrated in figure 3.4, is cubic and is adopted by $SrTiO_3$. Sr and Ti form cubic sublattices. At the centre of each Sr and Ti cube sits a Ti or Sr atom, respectively. The oxygen atoms reside at the centre of the Sr cube faces. The unit cell can be considered as a TiO_6 octahedron in the middle of a Sr cube. Sr^{2+} and Ti^{4+} are bonded to 12 and 6 oxygen atoms, respectively. ABX_3 perovskites in which the A and B cations are both trivalent are also common (e.g. $LaAlO_3$). The symmetry breaking shift of the Ti atom from the centre of the TiO_6 octahedron or the tilt of the entire octahedron gives

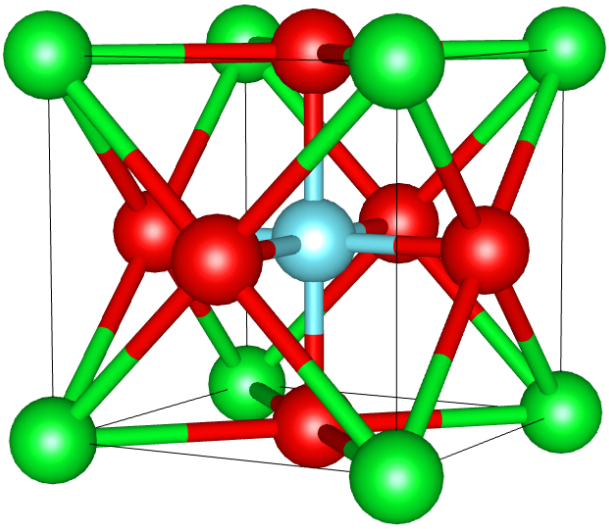

Figure 3.4: Ideal cubic perovskite structure. Here, $SrTiO_3$ is illustrated. Green, cyan and red represent strontium, titanium and oxygen, respectively. Sr and Ti form cubic sublattices. Oxygen atoms reside on the faces of the Sr cube and form a TiO_6 octahedron.

rise to the tetragonal and orthorhombic symmetry displayed by, for example, $BaTiO_3$ and $LaTiO_3$, respectively.

Intense research into the perovskites was stimulated in the 1940s, when barium titanate's ferroelectric properties were discovered. $BaTiO_3$ was readily employed in capacitors and transducers. It represented an important moment is the understanding and use of ferroelectrics, as $BaTiO_3$ was the first ferroelectric material not to contain hydrogen. The proceeding decades saw a dramatic increase in the number of synthesised perovskites and hundreds of perovskite compounds exist today. In recent times, perovskites continue to see substantial research interest. Most notable is the magnetic [17, 18] and conducting [16] properties which form at the interface of insulating, non-magnetic perovskites. Furthermore, some of the highest T_c superconductors consist of layered material containing slabs of perovskites and copper oxide [81].

Oxide perovskites with transition metals at the B site show a diverse range of electronic properties, for example: superconducting (Cu or Bi at the B site) to dielectric (Ti at the B site) and magnetic (Mn $\rightarrow$ Ni at the B site). Focusing on the titanates, the insulating nature and the relative ease at which perovskites can sustain cation shifts and octahedron tilt gives rise to the host of interesting dielectric properties and the phase strongly influences the dielectric properties. For example, $BaTiO_3$ is cubic above $\sim$400 K, however at room temperature the titanium atom shift from the centre of the TiO_6 octahedron resulting in a phase change to tetragonal symmetry and associated ferroelectricity.

Industrial application of titanate perovskites include piezo ceramics, microphones, high voltage capacitors, transducers and thermal cameras which all make use of dielectric properties. $PbZr_xTi_{1-x}O_3$ (PZT) ceramics are utilized in STM as they exhibit piezo constants in the range of a few Å/V.

3.2.1 Strontium titanate, $SrTiO_3$

Strontium titanate was first synthesised, along with several other perovskite titanates, in the 1940s. It was long thought to only exist in its synthesised

form. However, its naturally occurring counterpart, tausonite, was discovered in Siberia in the 1980s. Figure 3.4 displays the cubic unit cell. Below 105 K $SrTiO_3$ undergoes a transition to the ferroelectic tetragonal phase [82].

$SrTiO_3$ is transparent and insulating with a direct and indirect bandgap of 3.25 eV and 3.75 eV, respectively [83]. The conductivity can be drastically improved by doping with a small percentage of Nb. Unsurprisingly, this doping also reduces the transparency of pure $SrTiO_3$. Alternatively, high temperature annealing in a reducing environment can induce oxygen vacancies which increases the conductivity and opacity [84]. Interestingly, $SrTiO_3$ single crystals display persistent photoconductivity: when exposed to sub-bandgap light the free electron contribution increases by a factor of two. Once the illumination is removed, the increased conductivity persists with negligible decay. The photoconductivity has been related to excitation of an electron from titanium vacancies to the conducting band, with an extremely high decay time [85]. Reduced strontium titanate was the first oxide found to be superconducting, with the critical temperature in the range of 0.25 K [86]. The defect chemistry, whether it be in the form of anions or cations, clearly plays a vital role in the conductivity of $SrTiO_3$.

Strontium titanate is commonly used as a substrate for the growth of oxide perovskites, high temperature superconductors and oxides in general. Its lattice constant of ~ 3.9 Å makes it suitable for the growth of many oxides. Furthermore, Nb:$SrTiO_3$ is a rare commercial conducting oxide substrate.

The $LaAlO_3/SrTiO_3$ interface displays interesting properties such as a Quasi-2-Dimensional Electron Gas (Q2DEG) [16], magnetism [17] and even superconductivity [87]. The majority of studies involve the growth of (001) oriented $LaAlO_3$ on $SrTiO_3$(001) substrates [16, 17, 87–91]. However, the $LaAlO_3/SrTiO_3$(110) heterostructure, depicted in figure 3.5, has also been investigated and the interface displays an anisotropic Q2DEG [92].

Ohtomo *et al.*, who discovered the Q2DEG at the (001) interface, concluded that it was a result of charge transfer to the interface, which compensates for the polar nature of $LaAlO_3$(001) [16]. It was later demonstrated that the high-mobility was not present until the $LaAlO_3$ reached some critical thickness [88, 89]. This in is line with the polarity compensation in-

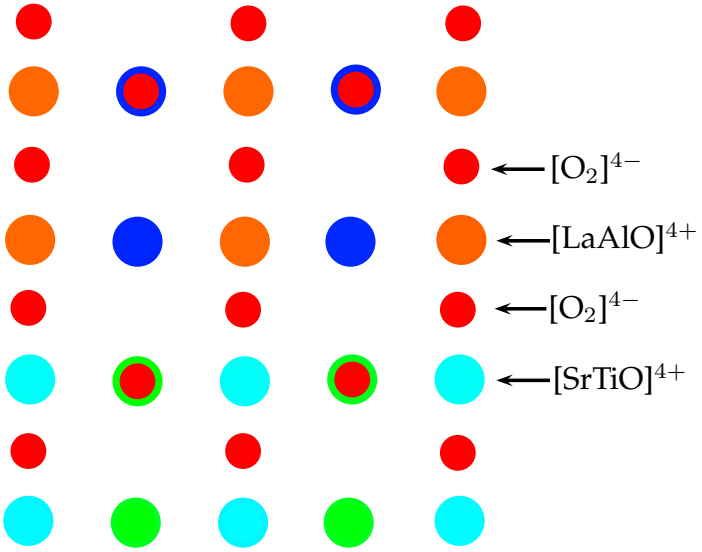

Figure 3.5: The $SrTiO_3/LaAlO_3(110)$ heterostructure. Sr, Ti and O are depicted as cyan, green and red. La and Al are depicted as blue and orange. Here, $SrTiO_3(110)$ is terminated by the oxygen plane. The terminating plane plays an important role in the formation of the electron gas at the interface. Pre-treatment is often applied to the $SrTiO_3$ substrate in order to form a titanium oxide termination. Oxygen vacancies in the $SrTiO_3$ substrate, which can form during $LaAlO_3$ growth, and charge transfer to the interface to compensate for the polarity of $LaAlO_3$, have also been inferred as the mechanism behind the formation of the Q2DEG at the (001) and (110) interfaces.

terpretation: the oppositely charged LaO and AlO_2 layers generate a dipole perpendicular to the surface, and the stacking of these dipoles results in an unphysical surface potential. At some critical thickness charge transfer to the interface, which removes the diverging surface potential, is energetically favourable over sustaining the surface potential. These studies could not rule out the possibility that strontium titanate oxygen vacancies near the interface contribute to the increased mobility: oxygen vacancies which form during UHV annealing, and hence heterostructure growth [90, 91], are accompanied by an increase in the mobility which is comparable to that of the heterostructure [93]. Several studies conclude that these vacancies are the main contributor towards the high-mobility [90, 91]. Varying the oxygen

partial pressure during growth alters the mobility [91] and pulsed-laser deposition, which is the growth technique used throughout, is suggested to preferentially remove oxygen from the strontium titanate substrate [90]. However, this does not account for the dramatic increase in mobility at some critical $LaAlO_3$ thickness [88, 89]. It is evident that oxygen vacancies have a role to play, however, the entire picture remains unclear.

An additional factor influencing the formation of the Q2DEG is the $SrTiO_3$ termination. Recently, in the case of the (001) interface, it has been demonstrated that if the $SrTiO_3$ is SrO-terminated the formation of the electron gas is suppressed. While if the $SrTiO_3$ substrate is TiO_2-terminated, the heterostructure exhibits good conductivity. Finally, a Ti-rich termination produces the highest conductivity heterostructure [94]. Evidently the $SrTiO_3$ termination plays a crucial role. Many studies employ *ex-situ* precleaning techniques, such as chemical etching, to produce titanium oxide terminations [92, 94, 95]. However, the influence of the growth conditions, which may change the surface structure of the $SrTiO_3$ substrate, appears to be overlooked.

Chapter 4

Metal Oxide, Fe_3O_4 & $SrTiO_3$ Surface Science

4.1 Metal oxide surface science

The vast majority of metals oxidise in ambient conditions. As a result, metal oxides play a pivotal role in processes such as friction, catalysis, lubrication and corrosion. Hence, the importance of understanding metal oxide surfaces' physical and chemical properties is clear. Metal oxides form a diverse range of crystal structures resulting in them exhibiting a wide variety of properties, such as superconductivity [96], semiconductivity [97], magnetoresistance [98], as well as acting as some of the best insulators. They can be inert enough to protect against corrosion but also act as catalysts. Metal oxide surfaces find industrial relevance in heterogeneous catalysis and modern-day electronics to name a few.

The field of oxide surface science has seen rapid growth in the last couple of decades. This was prompted by the emergence and combination of STM and DFT-based calculations which allow for the oxide surface to be examined on the atomic scale. Research initially focused on the atomic structure of oxides. STM provides unrivalled information about the features within the surface unit cell and the comparison between experimental and simulated images can be of great value. Furthermore, DFT calculations can provide

insight into the relative energetic stability of different terminations. The combination of STM and DFT remains the most commonly used method of determining surface structure, and combining them with techniques which average over larger surface areas, such as LEED, XPS and optical techniques, is clearly advantageous. In recent years, focus has shifted from the determination of the surface structure to the deposition of single-atoms and molecules on the oxide surface, so that absorption properties, dynamic behaviour and atomic-scale catalytic processes can be examined [9, 12–15, 99].

Metal oxides surface reconstructions are extremely common. Furthermore, the nature of the reconstruction is linked strongly to the preparation procedure [100–106]. Metal oxides surfaces have been utilized as templates for the deposition of single atoms and molecules [14, 107, 108]. Absorbents range in structure from 2D nanostructures [7] to stable single atoms [109]. The stoichiometry of the oxide template can dictate the size and shape of the nanoclusters, and hence, the electronic properties [7]. Furthermore, single atoms and molecules can nucleate in distinct sites or as clusters depending on the conditions [10]. This allows for the study of both catalysis of single atoms and the size effect.

In this chapter important concepts such as surface energy and surface polarity will be introduced and the importance of the cleaning procedure will be discussed. Surface reconstructions of magnetite and strontium titanate are discussed with the focus on STM studies.

4.1.1 Surface reconstructions

In the bulk of a material, an atom will have neighbours in all directions, and so its three-dimensional interactions define the crystal structure. However, creating a surface removes some of these neighbours, and hence breaks some bonds, changing the surface's intrinsic structure. This inequivalence means that the energetically favourable structure of a truncated plane may not be, and most likely wont be, the same structure that exists in the bulk. Hence, surface reconstructions are extremely common. Furthermore, in the case of polar terminations, such as those investigated in this work, bulk truncated

terminations cannot exist and therefore surface reconstructions form. This is explored in length in the next subsection.

A wide range of diverse reconstructions on metal oxides surfaces have been observed, for example: missing oxygen chains lead to a row reconstructed $MoO_2(100)$ surface [103], onefold oxygen caps the subsurface layer which contains rows of missing atoms on the (1×2) reconstructed $TiO_2(110)$ surface [110] and nanosized triangular and hexagonal islands stabilise the (0001) and $(000\bar{1})$ surfaces of ZnO, respectively [111]. Recently, a quasicrystal perovskite barium titanate ($BaTiO_3$) surface structure has been observed [112]. This structure remarkably exhibits mosaic- or tiling-like order, from which the surface structure over relatively large distances (on the atomic scale) can be extrapolated from, but does not exhibit a reducible surface unit cell.

The nature of the observed surface reconstruction can often depend on how the surface is prepared. Common preparation procedures utilized in oxide surface science include sputtering (with argon or neon ions) and annealing in UHV or oxygen environments. Sputter-anneal cycle are commonly used when the sample is introduced to the UHV chamber in order to produce an ordered, flat and clean surface. Generally speaking these cycles preferentially remove oxygen resulting in a reduced surface (see for example [104, 108, 113–115]). Oxygen annealing can increase the O/Fe surface ratio.

There are several surfaces which serve to demonstrate the importance of the cleaning procedure. For example, (111)-terminated magnetite, which will be discussed in detail in 4.2.2, contains six different surface layers, three of which have been observed experimentally and the cleaning procedure is determined to be crucial factor in determining which termination is present [104, 105, 116]. The (110) surface of TiO_2 is unsurprisingly reduced by UHV annealing, progressive annealing can transform this reduced surface from a (1×1) to a (1×2) reconstruction [100]. Additionally, sputtering can induce specific reconstructions: the (1×4) reconstruction of the $MoO_2(100)$ surface can be changed to a (2×1) reconstruction by sputtering and subsequent annealing [103].

Reconstructed surfaces often induce strain in the sub-surface region. This is unsurprising as the terminating layer differs in geometry and/or stoi-

chiometry from the sub-surface bulk truncated planes. In the case of the biphase superstructure formed on $Fe_3O_4(111)$, which contains $Fe_{1-x}O(111)$ and $Fe_3O_4(111)$ regions, a mosaic structure is formed whose geometry is dictated by the misfit, and hence the strain between the $Fe_{1-x}O(111)$ termination and the underlying $Fe_3O_4(111)$ [102]. On $SrTiO_3(110)$, the (4×1) reconstruction is entirely Sr deficient, as a result the surface can be considered as a titanium oxide complex on an $SrTiO_3$ substrate [117]. The mismatch produces strain which is reduced by the deposition of Sr which form adatom chains [118].

4.1.2 Surface polarity

An important concept to consider when dealing with surface reconstructions and especially metal oxide terminations is surface polarity. In 1979, Tasker classified surfaces into three groups defined by the charge distributed throughout the planes which truncate the crystal [119]. Type I surfaces are charge neutral and bear no dipole moment perpendicular to the surface. Type II surfaces are not charge neutral, however the repeating units bear no dipole moment perpendicular to the surface. Type III surfaces are not charge neutral and there exists a dipole moment perpendicular to the surface. Each of these classifications are depicted in figure 4.1. In the case of a type III surface two adjacent planes can be considered as a capacitor, and the sequence of capacitors leads to a diverging electrostatic energy [6]. Therefore, a type III surface, or a polar surface, must reconstruct to avoid this diverging electrostatic energy.

If one considers the type III periodic unit as a parallel plate capacitor, the electrostatic potential generated by planes with charge per unit area σ is given by:

$$\delta V = 4\pi\mu = 4\pi\sigma R$$

R is the distance between the oppositely charged planes. The energy stored in such a capacitor is given by:

$$\delta E = \frac{1}{2} C \delta V^2 = 2\pi\sigma^2 R$$

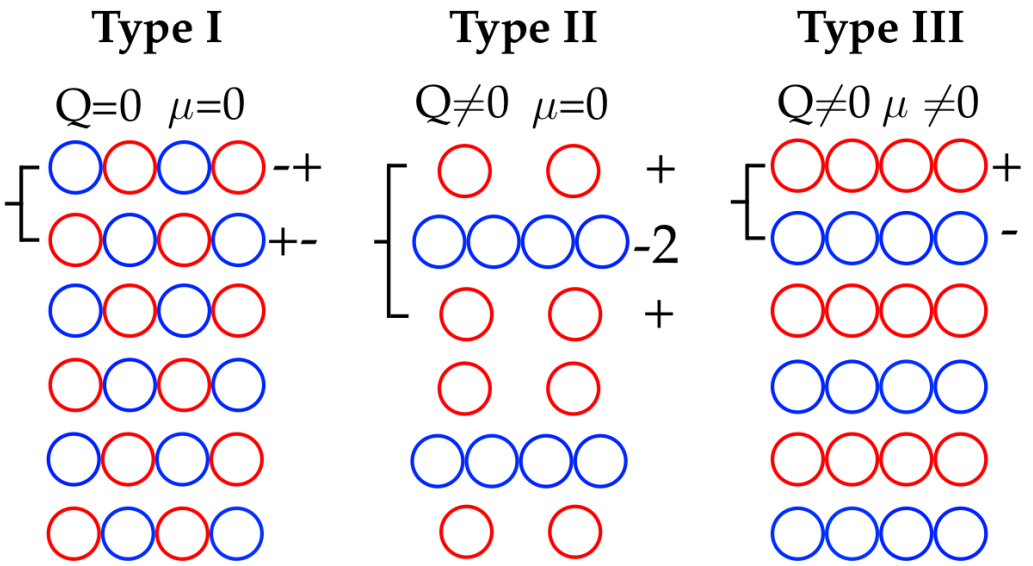

Figure 4.1: Tasker's classification of surfaces. Type I: each layer contains zero net charge and the repeating unit (illustrated by the bracket) bears no dipole moment. Type II: each layer (or at least one of them within the repeating unit) contains non-zero net charge but the repeating unit bears no dipole moment. Type III: each layer contains non-zero net charge and the repeating unit exhibits a non-zero dipole moment. Hence, type III surfaces are termed polar.

A series of M capacitors generates an electrostatic energy:

$$\delta E = 2M\pi\sigma^2 R \tag{4.1}$$

Therefore, a type III "polar" termination exhibits a diverging electrostatic energy. This polar catastrophe can be mitigated by modifying the charge of the terminating layers. In the case where the distance between each plane is identical this is achieved by reducing the charge of the terminating plane to $\frac{1}{2}\sigma$ [119]. Alternatively, is we choose a repeat unit such that it exhibits no dipole moment, the polar catastrophe is avoiding if the surface region above the final repeat unit bears no net charge [120].

Several polarity compensation mechanisms can stabilise polar oxide surfaces: presence of vacancies [121–123], adsorption of foreign species [124],

charge redistribution [125], increased surface covalent character [126, 127] or faceting [122]. In some cases, the combination of multiple mechanisms has been observed to stabilise oxide surfaces [122, 123].

4.1.3 Surface energy

The nature of the surface termination is strongly influenced by the relative stability of different terminations. In the frame work of this chapter it is therefore imperative to define the surface energy and discuss the benefits of its calculation. The following discussion describes how to calculate the surface energy of a magnetite surface from a DFT calculation. The surface energy, σ, of a slab is defined as follows [128]:

$$\sigma = (E_{surface} - N_O\mu_O - N_{Fe}\mu_{Fe})/2A \tag{4.2}$$

μ_O and μ_{Fe} represent the chemical potentials of the oxygen and iron atoms, N_O and N_{Fe} represent the number of oxygen and iron atoms in the slab, $E_{surface}$ is the total energy of the fully relaxed DFT calculation and A is the area of the surface. In the above equation we divide by $2A$ as there exists two surfaces, one each at the top and bottom of the slab. Of course, in this formulation both surfaces must be free to fully relax. If the bottom of the slab is fixed and passivated by hydrogen, $2A$ would be replaced by A. The chemical potential of the bulk magnetite unit is equal to the sum of its seven elemental chemical potentials [128]:

$$\mu_{Fe_3O_4} = 3\mu_{Fe} + 4\mu_O \tag{4.3}$$

The chemical potential of bulk magnetite can be obtained from a bulk DFT calculation. Therefore, by relating equations 4.2 and 4.3 one can obtain an expression for the surface energy, whose only variable is the oxygen chemical potential:

$$\sigma = \Big(E_{surface} + \big((\frac{4}{3}N_{Fe} - N_O)\mu_O - \frac{N_{Fe}\mu_{Fe_3O_4}}{3}\big)\Big)/2A \tag{4.4}$$

The lower limit of the oxygen chemical potential is defined as the point at which oxygen is prevented from entirely leaving the slab, and hence taken to be the heat of formation of magnetite at 0 K. Beyond this limit the slab would decompose into metallic iron and oxygen gas. The upper limit is defined as the point at which gas phase oxygen is prevented from condensing on the slab's surface, and hence taken to be half the total energy of a free, isolated O_2 molecule at 0 K. The upper and lower limits are defined as oxygen-rich and oxygen-poor regimes.

Calculating the surface energy provides insight into the relative stability of different terminations and the surface energy at particular chemical potentials provides insight into the relative stability for certain growth conditions, i.e. oxygen-poor or oxygen-rich environments.

4.2 Magnetite surface science

4.2.1 $Fe_3O_4(001)$

$Fe_3O_4(001)$ consists of two alternating planes, the first contains Fe_{tet} atoms while the second contains Fe_{oct} and oxygen. The Fe_{tet} plane is clearly positively charged, and hence, (001) terminated magnetite is polar.

The (001) surface of magnetite exhibits a $(\sqrt{2} \times \sqrt{2})R45\,^\circ$ reconstruction. STM images reveal that the features form buckled rows. This structure was initially interpreted to be terminated by a O-Fe_{oct} plane which contained oxygen vacancies [129]. There exists alternative interpretations of the reconstruction: charge ordering of Fe_{oct} sites which gives rise to Fe^{2+}-Fe^{2+} and Fe^{3+}-Fe^{3+} dimers [130] and a Jahn-Teller Stabilisation [131].

The structure of the $(\sqrt{2} \times \sqrt{2})R45\,^\circ$ reconstruction was not resolved until a detailed investigation of its absorption properties was performed. Single metal atoms, such as gold, bind exclusively in just one of the two available bulk continuation* Fe_{tet} sites per unit cell. The inequivalence of these sites was not accounted for in the understanding of the reconstruction at

*Bulk continuation site refers to a position above the surface, in the vacuum, which would be occupied if the vacuum is replace by the continued bulk.

the time. Furthermore, cobalt atoms were observed to be incorporated into the lattice upon deposited at room temperature and if one cobalt atom was deposited per unit cell (1×1) LEED spots were observed [132]. These observations indicated that subsurface cation vacancies were present. A model was developed which contains both subsurface Fe_{oct} vacancies and interstitial Fe_{tet} atoms. This model is energetically favourable over the entire range of oxygen chemical potentials accessible in UHV and accounts for the observed absorption dynamics [99]. Finally, the comparison between experimental and calculated LEED *IV* spectra for this model provides strong agreement [99].

Pioneered by the Diebold group in Vienna, the absorption properties of metals and small molecules deposited on the $(\sqrt{2} \times \sqrt{2})$R45 $^\circ$ surface has been extensively studied: gold atoms are preferentially located at one site in the unit cell and are either found as single atoms or as clusters [15]. Another example shows the formation of palladium clusters and the existence of isolated palladium adatoms. When carbon monoxide is introduced to the palladium adsorbed on the surface, palladium clusters form and the presence of surface hydroxyls results in palladium atoms becoming isolated as adatoms [9]. Furthermore, the surface has been utilized as a template for the study of single atom catalysis; water dissociates upon absorption: one of the hydrogen atoms adsorbs preferentially at a site within the unit cell which leads to the breaking of the H-O bond [12].

4.2.2 $Fe_3O_4(111)$

(111) orientated magnetite consists of six planes. Each plane solely contains oxygen, Fe_{oct} or Fe_{tet} atoms. The six planes form a O-Fe_{oct}-O-Fe_{tet}-Fe_{oct}-Fe_{tet} sequence. The two oxygen and two Fe_{tet} planes are identical in the bulk, while the two Fe_{oct} planes are not. However, all six bulk truncated surfaces are nonequivalent due to the different planes directly beneath them.

Considering the ionic model the six planes of (111) oriented magnetite form a O^{-8}-$Fe_{oct}^{+7.5}$-O^{-8}-Fe_{tet}^{+3}-$Fe_{oct}^{+2.5}$-Fe_{tet}^{+3} charge sequence, therefore (111) truncated magnetite is polar. The most common surface termination reported in the literature is interpreted to be the Fe_{tet} bulk truncated termination which

sits atop an oxygen sub-surface layer (termed Fe_{tet1}) [101, 104, 127]. LEED intensity calculations also favour this termination, although rather large relaxations (up to 41%) in the surface layers are observed [116, 127]. The agreement is improved if the considered model contains some Fe_{tet} surface vacancies [116] and STM images reveal missing protrusions from the perfect bulk truncated Fe_{tet1} lattice [104]. Further evidence for this termination is provided by DFT calculations: the Fe_{tet1} termination is energetically stable across all chemical potentials which correspond to UHV accessible conditions except for highly reducing conditions [133, 134]. At highly reducing conditions an Fe_{oct} termination, which sits atop an oxygen sub-surface layer, is energetically favourable (termed Fe_{oct1}). The Fe_{oct1} termination has been observed to coexist with the Fe_{tet1} termination in oxygen poor conditions [104].

The surface structure of $Fe_3O_4(111)$ appears to be very sensitive to the preparation procedure. The coexistence of different terminations is common and hard to avoid [101, 104, 105]. The Fe_{oct1} termination which forms under reducing conditions has not been observed to cover the entire or even the majority of the surface. Oxygen deficient $Fe_3O_4(111)$ single crystal surfaces can exhibit a superstructure [102, 104, 105, 116] which can coexist with the Fe_{tet1} termination [104, 116]. The reduction of the surface can be due to several sputter/anneal cycles without an oxygen anneal step [102] or the O/Fe surface ratio may reduce over time if the sample is held in UHV [104]. The superstructure consists of triangular islands which are approximately 5 nm in length and is interpreted to be a result of biphase ordering of $Fe_3O_4(111)$ and $Fe_{1-x}O(111)$ regions [102].

Compared to the (001) surface very few studies of the absorption properties have been reported. The deposition of gold and iron on the Fe_{tet1} and superstructure surfaces, respectively, have been reported. Au atoms adsorb initially as single adatoms and then nucleate into clusters [135]. Iron forms one monolayer high clusters on the biphase superstructure, the size and separation of these clusters are defined by the superstructure [136].

4.2.3 $Fe_3O_4(110)$

(110)-terminated magnetite consists of two alternating planes, namely, the A and B planes, which are illustrated in figure 4.2. The oxygen atoms in each plane form consecutive (110) planes of the oxygen FCC sublattice. The A plane contains both coordinations of iron while the B plane only contains Fe_{oct} iron. Considering that oxygen, Fe_{oct} and Fe_{tet} have ionic oxidation states of 2-, 2.5+ and 3+ the A plane unit cell, which contains four oxygen, two Fe_{oct} and two Fe_{tet} has a charge deficit of $3e^-$. Similarly, the B plane with four oxygen and two Fe_{oct} has a charge excess of $3\,e^-$. Hence, like magnetite's two other low index surfaces, (110) terminated magnetite is polar.

Although magnetite has been studied extensively by STM, the (110) surface has received little attention. Jansen first studied the (110) surface of single crystal magnetite in 1994 [137–139]. Later, Maris *et al.* investigated the (110) surface of thin films grown on a MgO substrate [140–142]. These investigations all revealed a (1×3) row reconstruction. However, differences in the number of rows within the (1×3) unit cell were reported. The rows were observed to run in the $[1\bar{1}0]$ direction.

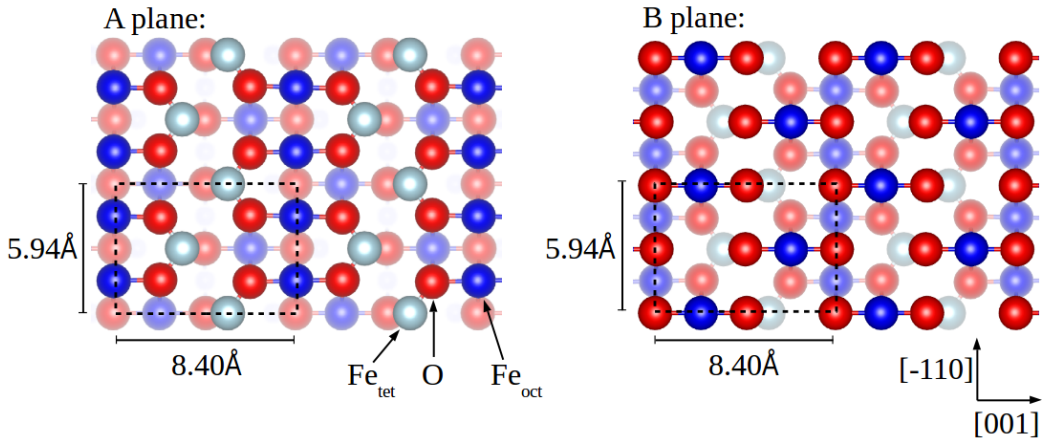

Figure 4.2: Magnetite terminated in the (110) direction consists of two alternating planes. The A plane contains oxygen (red) and both octahedral (blue) and tetrahedral (silver) coordinated iron. The B planes contain oxygen and octahedral coordinated iron.

Recently, Parkinson *et al.* [143] concluded that the row reconstruction was a result of periodic nanofaceting which exposed {111}-like planes; the reconstruction consists of rows with depressions, or troughs, in between, the slope from the ridge to trough were concluded to be {111}-type planes. This was determined on the basis of Reflection High-Energy Electron Diffraction (RHEED) measurements and STM line profiles. The RHEED measurements, in which the electron beam was perpendicular to the surface, exhibited reflection spots separated by 35 ° to the surface normal, which corresponds to the angle between (110) and (111) planes. (111) terminated magnetite is considerably more energetically stable relative to the (110) termination [144], and hence the faceting acts to reduce the surface energy.

To the author's knowledge, there are no STM investigations of the absorption properties of $Fe_3O_4(110)$. The determination of the surface structure of (110)-terminated magnetite is pivotal to potential future investigation of the surface's absorption properties.

4.3 Strontium titanate surface science

4.3.1 $SrTiO_3(001)$

(001)-truncated strontium titanate consists of two alternating planes: SrO and TiO_2 which are both charge neutral. Therefore, $SrTiO_3(001)$ is not polar and in theory a (1×1) termination should be possible. Indeed, a TiO_2 (1×1) termination has been reported [145]. A wide range of surface reconstructions have been reported such as (2×1), (2×2), $c(4 \times 2)$, (4×4), $c(4 \times 4)$, $c(6 \times 2)$, $(\sqrt{5} \times \sqrt{5})R26.6°$ and $(\sqrt{13} \times \sqrt{13})R33.7°$ [146–149].

Prior to introducing (001) strontium titanate single crystals to UHV, wet etching is often used as a pre-treatment[†]. The wet etching procedure [150, 151] consists of initially soaking the surface in hot or room temperature deionised water. Strontium oxide reacts with water more strongly than titanium oxide, forming strontium hydroxides. Subsequent wet etching (HCl-

[†]Buffered HF is a more commonly used wet etching pre-treatment. The HCl-HNO_3 wet etching technique is discussed here as it is employed in this work.

HNO_3 3:1) easily removes these hydroxides producing a titanium oxide-rich surface region. Finally, the crystal is annealed in air to facilitate recrystallisation. The annealing temperature is chosen such that is does not allow diffusion of Sr from the bulk. This pre-treatment strongly influences the resultant surface structure, even after vacuum annealing is performed.

UHV annealing of pre-etched surfaces produces (2×1) [146], (2×2) [147] and $c(4 \times 4)$ [146, 147] reconstructions, depending on the temperature. Sputtering, which results in titanium enrichment [152, 153], causes the formation of a $c(4 \times 2)$ reconstruction [146, 148]. The deposition of Sr sees this reconstruction transform to (2×2) and the subsequent deposition of Ti sees the surface return to $c(4 \times 2)$ periodicity [148]. These reconstructions have been interpreted to be TiO_x terminated. This is unsurprising as sputtering and wet etching produce Ti enriched and Sr deficient surface regions, respectively. Furthermore, Sr diffusion is reported to only occur above 1300 °C [154].

4.3.2 $SrTiO_3(111)$

(111)-truncated strontium titanate consists of two alternating planes: SrO_3 and Ti. Considering the ionic model, the unit cells bear charges of -4 and +4. Therefore, the (111) termination is polar. The reconstructions reported on the (111) termination are all of the form $(n \times n)$. These reconstructions can be split into two groups: (1) those which form after sputtering and annealing and (2) those which form after annealing alone. Reconstructions formed after sputtering range from $n = 9/5, 2, 3, 4, 5, 6$ depending on the annealing environment [155]. Annealing in UHV without an initial sputter results in the formation of co-existing $(\sqrt{7} \times \sqrt{7})R19.1°$ and $(\sqrt{13} \times \sqrt{13})R13.9°$ reconstructions [156]. The sputtered surfaces are Ti enriched, as is the case for the (110) and (001) terminations.

4.3.3 $SrTiO_3(110)$

(110)-truncated $SrTiO_3$ consists of two alternating planes: the SrTiO and O_2 planes. Considering the ionic model, the units cells bear charges of +4 and -4, respectively. Therefore, $SrTiO_3(110)$ is polar. The two alternating

planes are depicted in figure 4.3. Unlike the other two low index surfaces, the $SrTiO_3(110)$ unit cell is anisotropic. In the literature, reconstructions are defined such that the first integer represents the multiple of the periodicity in the [001] direction and the second integer represents the multiple of the periodicity in the $[\bar{1}10]$ direction. Unfortunately, this is opposite to that which has been adopted for $Fe_3O_4(110)$.

Brunen *et al.* [157] performed one of the first studies detailing $SrTiO_3(110)$ surface reconstructions: (2×5), (3×4), (4×4) and (6×4) reconstructions were reported. The most common and most studied reconstructions are those of the form $(n \times 1)$. Russell *et al.* [158] observed a (3×1) reconstruction upon annealing at 875 °C in a UHV environment. Annealing at temperatures of 1100 °C and 1275 °C transformed the reconstruction to (4×1) and (6×1), respectively. STM images revealed that the step edges of the (3×1) and (6×1) reconstructions were often decorated with (2×4) and (1×2) reconstructions. The $(n \times 1)$ reconstructions are clearly related as they can coexist [117] and it is widely regarded that the terminating planes are formed of TiO_x complexes [117, 159]. The TiO (SrTiO with Sr removed) termination is the energetically favourable surface termination [159]. Enterkin *et al.* proposed that the fundamental building block of the reconstruction is the TiO_4 tetra-

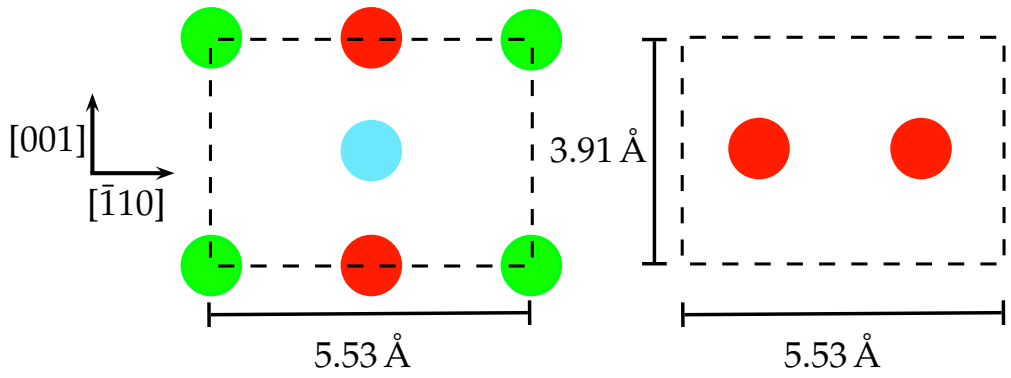

Figure 4.3: The SrTiO and O_2 planes of (110) terminated $SrTiO_3$. Green, cyan and red represent strontium, titanium and oxygen, respectively. The SrTiO and O_2 planes exhibit ionic charges of +4 and -4, respectively. Hence, (110) terminated strontium titanate is polar.

hedron. Removal of different numbers of tetrahedrons generates unit cells of greater size [117]. However, this model does not consider the role of Sr, which cannot be ignored; Li *et al.* [159] demonstrated that the (4×1) reconstruction was transformed to the (5×1) reconstruction via the evaporation of Sr. The reverse transformation is observed via the deposition of Ti [160].

Additional reconstructions included (2×4), (6×4) and (1×5). The (1×4) reconstruction can be formed by sputtering or evaporating Ti at elevated temperature onto the (4×1) reconstruction [161]. Further Ti evaporation or sputtering sees the formation of a (6×4) reconstruction. Finally, aggressive sputtering causes the (2×4) reconstruction to transform to a (1×5) periodicity [162].

We now turn to how the stoichiometry is influenced by different preparation procedures and its relation to the reconstructions. Sputtering causes a relative increase in Ti/O and Ti/Sr ratios [162]. Furthermore, XPS/UPS investigations of the influence of sputtering on each of the low index surfaces indicate that the relative Ti enrichment is accompanied by Ti^{3+} and Ti^{2+} states, and a metal state [152, 162, 163]. Annealing in UHV does not appear to be as straightforward a picture: for the $(n \times 1)$ series of reconstructions, $n = 3$ is formed at relatively low temperatures (875 °C) and shows relative Ti enrichment and Sr depletion [158]. With increasing temperature (1100 °C - 1275 °C), which sees the unit cell progress from $n = 4$ to $n = 6$, the relative Sr content is enriched and Ti is depleted [158, 159, 161]. Indeed, deposition of Ti [160] or Sr [159] at elevated temperature sees n change from $6 \rightarrow 4$ or $4 \rightarrow 6$, respectively. The $(n \times 1)$ reconstructions do not display lower titania oxidation states or the associated metallic state [158, 164]. The (110) reconstructions which display lower titania oxidation states and a metallic state are the (2×4), (6×4) and (1×5) reconstructions [162] which are formed by sputtering or Ti deposition which increases the relative Ti content in the surface region.

In conclusion, $SrTiO_3$(110) displays a zoo of reconstructions, which are extremely sensitive to both the *ex-situ* and *in-situ* preparation procedures. The annealing temperature, environment and duration can dictate which reconstruction(s) are present. Sputtering and the deposition of Ti or Sr can

transform the surface structure. The stoichiometry in the surface region can be dramatically altered and Ti rich terminations are dominant. Strontium is preferentially removed by sputtering and wet etching but begins to diffuse from the bulk at high temperatures. Unsurprisingly different terminations are reported to exhibit different stoichiometries in the surface region. Furthermore, it very common for multiple reconstructions to coexist and it appears to be difficult to isolate one reconstruction.

Chapter 5

Optical Anisotropy of (110) Terminated Fe_3O_4 & $SrTiO_3$

RAS studies of metal oxide surfaces are rare; investigated materials include ZnO [35], superconducting cuprates [37] and Fe_3O_4[36]. The latter was conducted in our research group and consisted of an *ex-situ* study of the single crystalline and thin film Fe_3O_4/MgO (110) surfaces.

RAS is a versatile tool, sensitive to surface and interface structures, providing the underlying bulk material is isotropic [28]. It represents a technique which can characterise surface and electronic structure, can monitor changes in surface structure and identify specific surface terminations in real-time. Despite this, to the best of the author's knowledge, RAS has not been employed in the investigation of metal oxide surface reconstructions. In this chapter the anisotropic optical responses of the (110) terminations of single crystalline, bulk isotropic, Fe_3O_4 and $SrTiO_3$ are investigated. Their surface reconstructions, which arise from the relative ease at which their stoichiometry is altered and the need to compensate for their polarity, will dictate any anisotropic optical response.

RAS spectra have been recorded with two in-house built systems following the Aspnes design [38]. One system with a broad spectral range of 0.35 - 5.5 eV was used primarily for studying *ex-situ* surface preparation. A second more compact system was used for *in-situ* measurements in the spectral range

of 0.8 - 5.2 eV. Details on the two spectrometers are found in section 2.3.1. The real part of the complex RAS response in presented throughout.

5.1 Optical anisotropy of $Fe_3O_4(110)$

In this section a RAS study of $Fe_3O_4(110)$ is presented. Initially the anisotropic optical response of the *ex-situ* polished single crystal is revisited. Subsequently the anisotropic optical response of the {111}-nanofaceted row reconstruction is presented and discussed.

The spectra of both the polished and reconstructed crystal show a strong comparison to the three-layer derivative model (see section 2.3.2). This indicates a small shift in energy of magnetite's bulk-like optical transitions due to the influence of an anisotropic surface region. The RAS response is concluded to be a result of anisotropic strain in the terminating layers.

5.1.1 Experimental details

The single crystals studied were float zone grown (Moscow State Steel and Alloys Institute). The previous RAS study conducted by Fleischer *et al.* [36] initially polished the single crystal using sandpaper. Subsequently, diamond and cerium oxide suspensions with a final grain size of 0.01 μm were used for further polishing until an optically flat surface was achieved. During the polishing process, the sample was moved in a figure of 8 pattern and rotated occasionally in order to ensure that the polishing was smooth and did not cause any preferential direction which might influence any measurement of the samples anisotropy. In this work, a single crystal from the same batch was polished in a similar fashion.

Electrical measurements of T_V in a helium cryostat with a closed cycle refrigerator, resulted in a T_V of 122 ± 1 K. The samples resistance was measured with a Keithley 2400 source meter [36]. Stoichiometric magnetite is expected to have a T_V of around 120 K [165]. As magnetite becomes cation deficient T_V decreases, and the transition eventually disappears. The Verwey transition has been observed to disappear if the iron content is reduced by

less than 1% [165]. T_V is therefore a very good indicator of the quality of the sample.

For the preparation of the {111}-nanofaceted row reconstruction, initially several sputter/anneal cycles were performed to remove bulk contaminants. The crystal was subsequently exposed to atmospheric conditions prior to being placed back in the UHV chamber. This avoids the possibility that sputtering influencing the surface structure, which is shown to occur in chapter 7. The crystal was then out-gassed and subsequently annealed at 600 °C for 9 h. Finally, the crystal was UHV flash annealed at 900 °C for 10 s, twice. The presence of the {111}-nanofaceted row reconstruction is confirmed by STM and LEED. The preparation of this reconstruction, and the motivation behind the aforementioned procedure, is detailed at length in chapter 6.

The RAS unit, $\Delta r/r$, is equal to $2\frac{r_x - r_y}{r_x + r_y}$. In the presented RAS spectra, x and y correspond to the [001] and [$\bar{1}$10] directions, respectively. This is the same formalism as that used in [36].

5.1.2 As-polished surface

The RAS spectra of the polished crystal is identical to that observed in [36] and is depicted in figure 5.1 (—). The anisotropic optical response in [36] was suggested to originate from anisotropic strain; the lineshape resembled the derivative of magnetite's dielectric function, indicating that small shifts in energy of the optical transitions, such as those associated with anisotropic strain, were likely responsible for the anisotropic response. However, the possibility that a thin maghemite overlayer, which forms in ambient conditions [166], may contribute to the anisotropic response was not ruled out.

Here, the crystal has been UHV annealed *in-situ* stepwise at 200 °C, 350 °C, 550 °C and 800 °C. The RAS spectra for each of these steps are depicted in figure 5.1 alongside that of the polished surface. Evidently, each of the anneal steps reduces the magnitude of the large derivative-like feature. The lineshape remains largely the same, although the maxima and minima located at 1.1 eV and 1.6 eV are progressively shifted to lower energies. The spectrum after heating to 800 °C shows the greatest deviation from the pol-

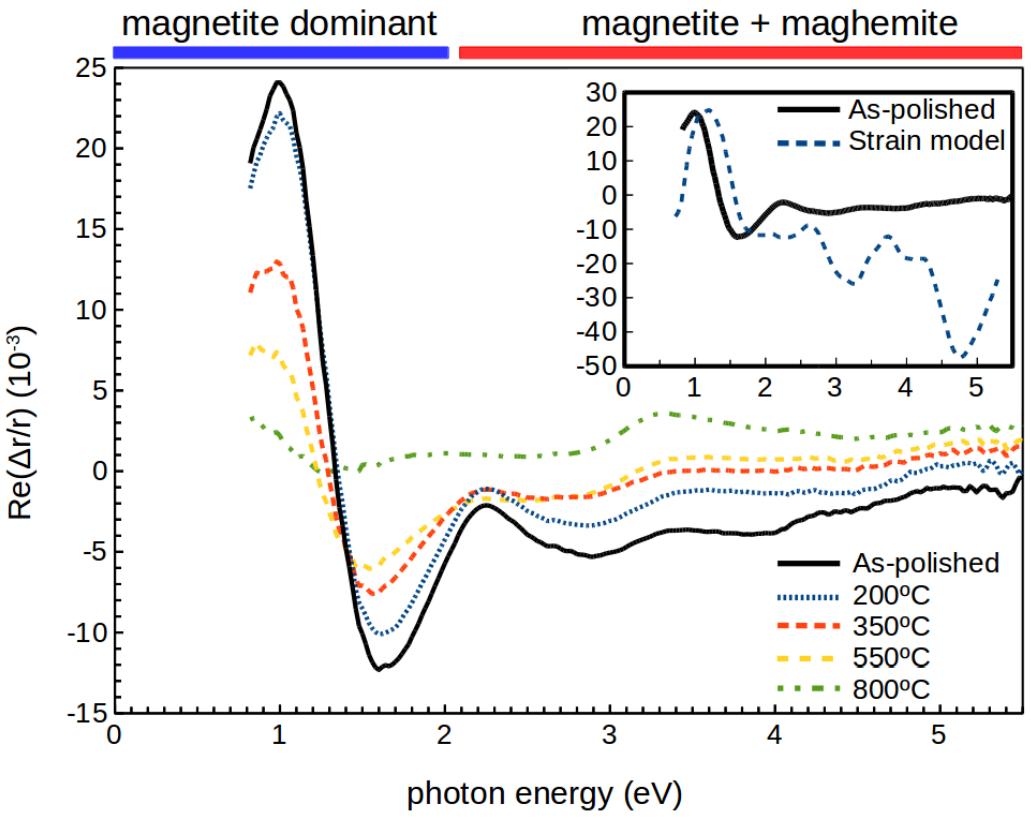

Figure 5.1: RAS of the polished surface (—) which is identical in shape to that reported by Fleischer *et al.* [36]. The crystal was annealed progressively at increasing temperatures in a UHV environment. Clearly, the magnitude of the maxima/minima feature is progressively reduced with each anneal step. Inset: RAS of the polished surface (—) is compared to the strain model (---) calculated from equation 2.16. In the spectral region below around 2 eV, where magnetite's optical transitions dominate, there is good agreement with the strain model indicating a modification of magnetite's bulk-like states. $\tilde{\epsilon}_b$ is taken from experimental work conducted by Schlegel *et al.* [167].

ished surface lineshape; the maxima at 2.3 eV is removed entirely and a broad feature at 3.3 eV is enhanced.

LEED measurements of the 800 °C annealed crystal are indicative of a poorly-ordered row reconstruction, while LEED images after lower temperature anneals are indicative of an entirely disordered surface. In ambient conditions the magnetite surface region is transformed into maghemite (for

example, 2 nm maghemite surface layer after two months [43]). While in an extremely low molecular oxygen partial pressure environment, such as UHV, magnetite is the stable iron oxide above approximately 600 °C (see figure 3.1, taken from [52]). Therefore, annealing the crystal at significantly higher temperatures, such as 800 °C, is expected to transform the surface region from maghemite to magnetite. The penetration depth of light for magnetite varies from just 30 nm in the UV to a maximum of 160 nm around 1.4 eV [36]. Hence, considering after prolonged exposure (two months [43]) the maghemite overlayer formed on thin-film Fe_3O_4 is only 2 nm in depth [43], RAS will probe both anisotropies in the maghemite overlayer and the underlying magnetite.

The lineshape of the polished surface exhibits a derivative-like feature below around 2.0 eV. As discussed in detail in section 2.3.2, the reflectance anisotropy is expected to resemble the first energy derivative of the bulk dielectric function if the orthogonal components of the surface region's dielectric function are similar in magnitude but differ slightly in energy. In the case of a (110) terminated cubic material, the most reasonable source of the anisotropic shifts in energy of the optical transitions is anisotropic strain. The inset of Figure 5.1 depicts the strain model (**---**) for bulk magnetite which is compared to the as-polished RAS lineshape (**—**). $\tilde{\epsilon}_b$ is taken from experimental work conducted by Schlegel *et al.* [167], which is depicted in figure 5.2. A value for d of 22 nm was chosen to fit the maxmima-minima feature. The lineshape is in good agreement at low-energies with the maxima-minima feature reproduced. This derivative-like structure below 2.0 eV cannot be attributed to a maghemite overlayer, as maghemite only shows distinct peaks in its absorption spectra above 2.0 eV [168]. Indeed, optical transitions below 2.0 eV in magnetite are known to only involve Fe^{2+}_{oct} sites [169, 170] and maghemite contains Fe_{oct} vacancies which results in the absence of the Fe^{2+}_{oct} site.

The maghemite-magnetite interface will likely induce strain gradients in both materials and the resultant strain gradient can induce small anisotropic shifts in energy of magnetite's optical transitions, producing a RAS signal comparable to the strain model below 2 eV where magnetite dominates. The comparable electronic structures of magnetite and maghemite - both being

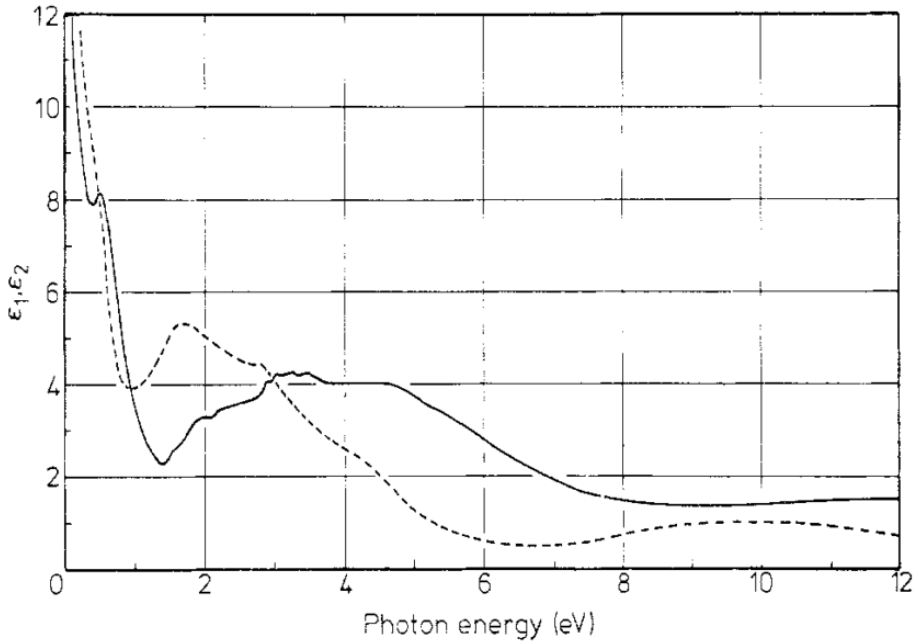

Figure 5.2: Real (---) and imaginary (—) components of the complex dielectric function of bulk magnetite as it results from the Kramers-Kronig analysis of the reflectivity spectrum. Taken from [167] and used to calculated the strain model (see equation 2.16).

inverse spinel - will likely result in RAS features at spectral energies above around 2.0 eV being a linear combination of anisotropies in both magnetite and maghemite. Progressive annealing, which reduces the magnitude of the derivative-like structure, may progressively relieve the strain. For example, the magnitude of the RAS response of mechanically strained silicon is proportional to the applied strain [42]. The low temperature anneals, which reduce the magnitude of the derivative-like structure, are not expected to transform a maghemite overlayer to magnetite [52]. However, annealing may provide energy to relieve strain, and hence, alter the magnitude of a strain induced RAS response.

5.1.3 {111}-nanofaceted row reconstruction

Presented in figure 5.3 is the RAS spectra of the Fe_3O_4(110) {111}-nanofaceted row reconstruction*. The corresponding STM and LEED image which are indicative of a clean, well ordered {111}-nanofaceted row reconstruction are displayed in figure 5.4. The RAS spectra is characterised by a minima-maxima feature below around 2 eV and a broad feature at higher energies with peaks at 4.1 eV and 5.2 eV.

The vertical dashed lines in figure 5.3 signify energetic positions of optical transitions, taken from [169, 170]. In figure 5.3, the octahedral sites are split into 2+ and 3+ sites. All optical transitions probed by RAS are interband, as intraband transitions of magnetite are below 0.2 eV [170]. Therefore, RAS features are expected to be broad in shape. Below around 2.2 eV optical transitions are exclusively between Fe_{oct} sites. The transitions above 2.2 eV also involve Fe_{tet} and oxygen sites and are considerably broad as a result [169]. In this region above 2.2 eV, it is important to note that the vertical dashed lines in figure 5.3 indicate the peaks of these broad transitions.

The RAS lineshape is often the linear combination of optical anisotropies from different structures or mechanisms, e.g. a reconstructed surface or residual structural effects of the near-surface region. In order to determine the contribution to the RAS signal from the surface reconstruction, the following experiments have been performed: the {111}-nanofaceted row reconstruction was prepared and a RAS measurement was performed, subsequently the reconstruction was destroyed by aggressive sputtering and a second RAS measurement was performed. The row reconstruction was prepared by the following procedure: sputtered with Ar^+ ions of energy 0.5 keV for 1 h, annealed in an oxygen atmosphere at 800 °C for 1.5 h and finally annealed in an UHV atmosphere at 800 °C for 1.5 h. The reconstruction was destroyed by sputtering with Ar^+ ions of energy 1.5 keV for 0.5 h. Figure 5.5 displays

*It is noted that RAS spectra in figure 5.1(- · - · -), which was observed after annealing the as-polished crystal at 800°C, does not corresponds to the RAS spectra of the {111}-nanofaceted row reconstruction (figure 5.1(——)), which forms after flashing to 900°C. Prolonged outgassing is required, prior to flashing at elevated temperatures, to form the {111}-nanofaceted row reconstruction.

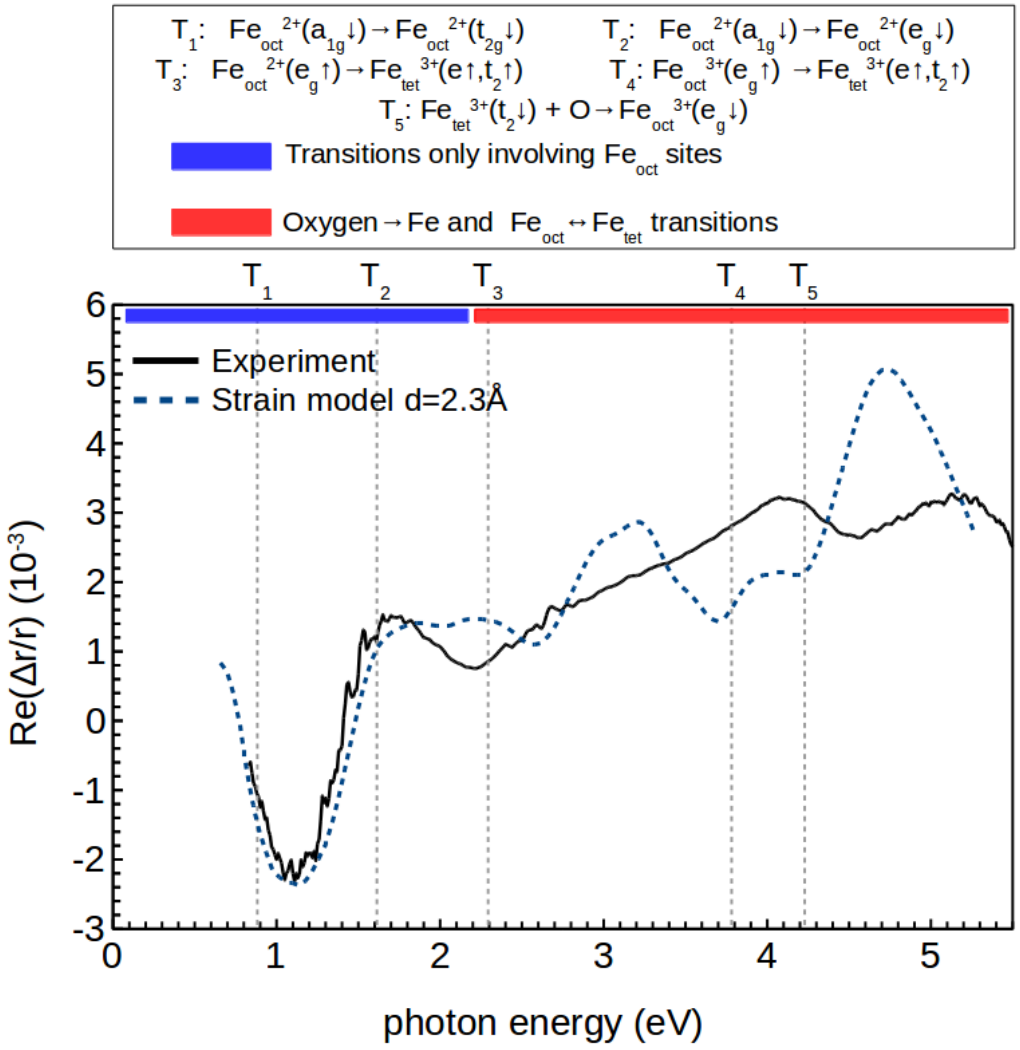

Figure 5.3: RAS of the {111}-nanofaceted (1×3) row reconstruction (—). The surface was prepared by two 10 s UHV flash anneals at 900 °C. Vertical dashed lines denote energy positions of optical transitions taken from [169] and [170]. Below around 2.2 eV, transitions only involve Fe_{oct} sites, while above around 2.2 eV oxygen and Fe_{tet} sites are also involved. The strain model (---, equation 2.16) and experimental RAS spectra (—) are in excellent agreement below 2 eV indicating a modification of magnetite's bulk-like states. The experimentally measured dielectric function of magnetite ($\tilde{\epsilon}_b$) is taken from [167].

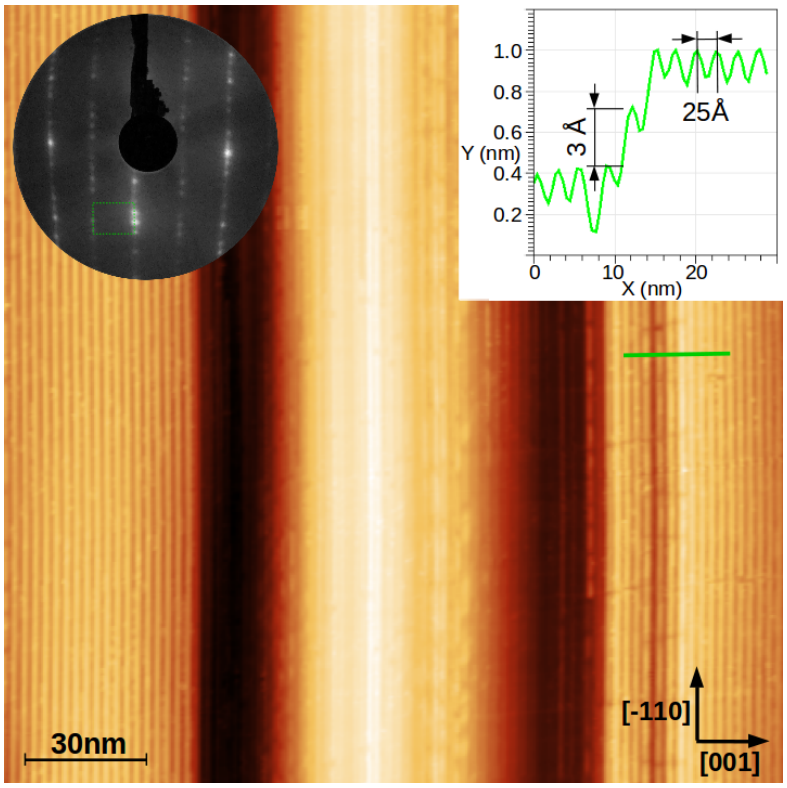

Figure 5.4: 205 nm × 205 nm STM image. The same surface for which RAS measurements, depicted in figure 5.3, were performed. The LEED image and the line profile illustrating the row periodicity of 25Å and the step height of 3Å are indicative of the {111}-nanofaceted row reconstruction.

the two RAS spectra and their corresponding LEED images. The row reconstruction exhibits reasonably good order while the LEED image of the sputtered surface indicates that the row reconstruction is destroyed, as expected. However, undefined LEED spots indicate some residual order remains.

The difference spectra (blue dashed line in figure 5.5) illustrates that the row reconstructed and disordered surface show similarities, especially beyond 2 eV, both displaying peaks at 4.2 and 4.9 eV and the general lineshape is very similar. The only considerable difference between the two spectra occurs below around 2 eV: the energetic positions of the maxima and minima are shifted in energy and the shape is altered slightly. The difference beyond 2 eV is a difference in slope, which is likely related to slightly different sample

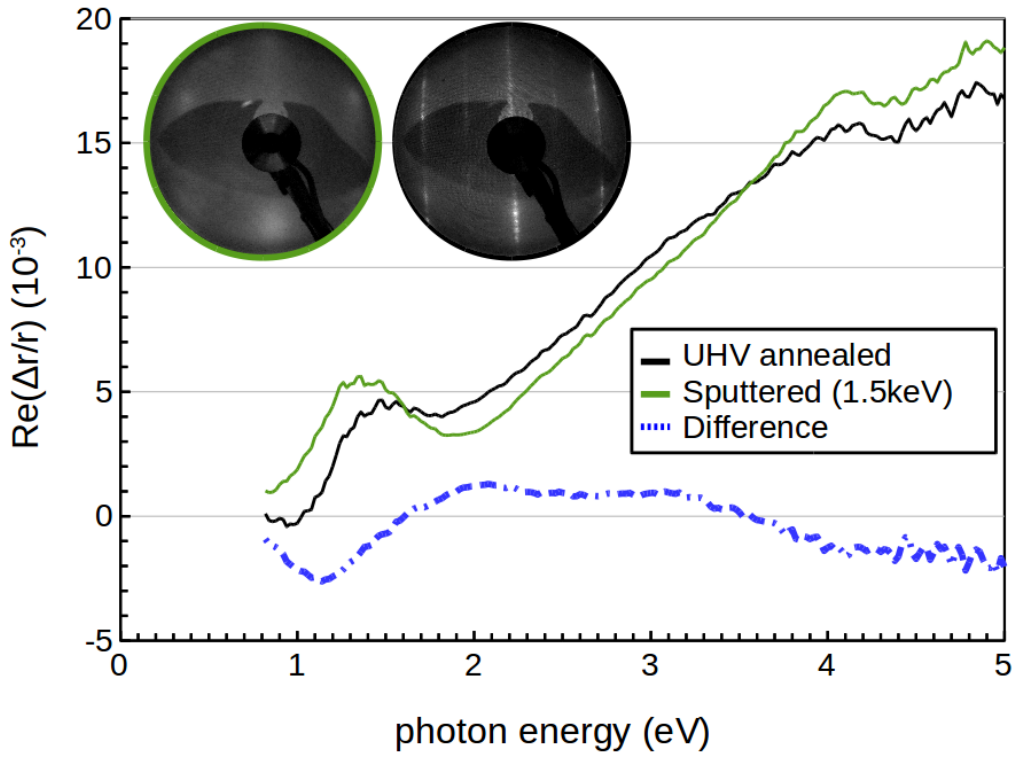

Figure 5.5: RAS spectra of the {111}-nanofaceted row reconstruction (—) and the sputtered surface (—). LEED images indicate that the sputtering destroys the row reconstruction although some residual order remains. The only considerable difference in the spectra is seen below around 2.0 eV. The difference beyond 2 eV is a difference in slope, which is likely related to slightly different sample position and/or or beam path through the window between measurements.

position and/or or beam path through the window between measurements. The {111}-nanofaceted row reconstruction gives rise to a considerable optical anisotropic response only below 2 eV. Henceforth, focus will be on this spectral region.

Similarly to the the polished crystal, the RAS lineshape of the {111}-nanofaceted row reconstruction exhibits a derivative-like feature below 2.0 eV. However, there is a sign reversal. In figure 5.3 depicts the RAS spectra (—) is compared to the three-layer derivative model (---, equation 2.16). Below 2.0 eV, in the spectral range where this reconstruction produces significant

optical anisotropy, the minima/maxima feature is reproduced and the general shape is in excellent agreement.

The comparison presented in figure 5.3 strongly indicates that the surface induces anisotropic energy shifts of bulk-like states. The optical transitions which are modified in this energy regime are inter Fe_{oct} sites, as below 2.2 eV optical transitions only involve these sites. In the case of the examined {111}-nanofaceted row reconstruction, the most likely explanation for the surface-induced modification of bulk-like states is anisotropic strain. In the plane of the surface, the row reconstruction exhibits 1D broken bonds. Figure 5.6(a) aids in visualising these broken bonds, which are in the [001] direction. Derivative-like RAS structures have been shown to be induced by mechanically applying strain to e.g. optically isotropic silicon [42]. In the case of silicon, the derivative-like structure can be very sharp. This can be expected for a response involving equally well defined interband transitions. The complex interband transitions of magnetite will give rise to broader features.

DFT calculations have been performed to examine whether this surface reconstruction induces a strain gradient. The model, which is depicted in figure 5.6(a), corresponds to a stoichiometric slab terminated by {111} Fe_{tet1}- and {110} B-planes. This model is the same as that proposed by Parkinson *et al.* [143] in all aspects apart from the {110} termination[†]. For details of the DFT calculation the reader is directed to section 7.2, as the parameters are identical to the calculations discussed there. Figure 5.6(a) and (b) depict the side-on initial and relaxed geometries. No significant relaxations along the $[\bar{1}10]$ direction (into the page) are present. The terminating layer sees significant relaxation along the [001] direction and the layers beneath see reducing relaxations in the [001] direction until the structure is bulk-like. Therefore, DFT predicts an anisotropic strain gradient. It is important to note that the atomic structure of the {111}-nanofaceted (1×3) row reconstructed remains to be determined, and the model illustrated in figure 5.6 is not suggested to be its solution. Nevertheless, minor changes are unlikely to remove the

[†]Section 6.2.1 examines the structure of this reconstruction: it is concluded that the ridge of the reconstruction is likely B-terminated.

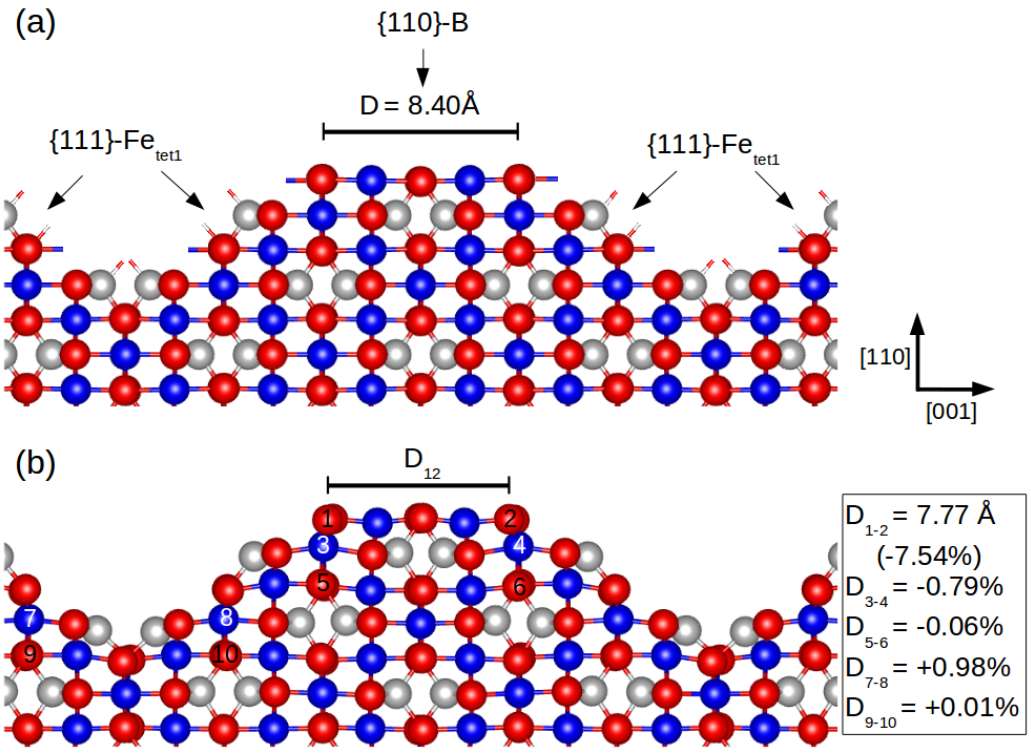

Figure 5.6: Initial (a) and (b) relaxed geometries of a {111}-nanofaceted row reconstruction model. Dangling bonds in the [001] direction are illustrated in (a). The black box provides examples of the percentage compressive (negative) and tensile strain, relative to the bulk distance, within different layers. D_{12} corresponds to the distance between the two atoms labelled 1 and 2 in (b). Along the [$\bar{1}$10] direction (into the page) no significant relaxations are observed. The calculation predicts an anisotropic strain gradient along the [110] direction (surface normal).

anisotropic strain, as it is suggested to exist due to the row structure which remove bonds anisotropically.

Jeng *et al.* have performed a DFT investigation of the influence of strain on bulk magnetite's electronic structure [171]. Uniaxial strain was applied in the [001] direction, the same direction for which DFT calculations predict uniaxial strain in the terminating layers of the {111}-nanofaceted row reconstruction. It was found that under both compressive and tensile strain, Fe_{oct} 3d sites saw the considerable modification while other sites remained largely

unchanged. Specifically, the $Fe^{3+}_{oct}(e_g)$ majority band near the Fermi level and the $Fe^{2+}_{oct}(e_g)$ minority band between 1.0 and 2.5 eV above the Fermi level were modified. The strain induced both band dispersion and band broadening. Turning our attention to the optical transitions, the first transition involving a $Fe_{oct}(e_g)$ band occurs at 1.6 eV. This transition is between $Fe^{2+}_{oct}(a_{1g})$ and $Fe^{2+}_{oct}(e_g)$ minority bands. In the energy range in which the experimental and strain model RAS are comparable (see figure 5.3) this transition is the only one involving a $Fe_{oct}(e_g)$ band. If the strain in the surface region modifies the minority $Fe_{oct}(e_g)$ band it is reasonable to see a good agreement between the experimental and calculated RAS signals in the vicinity of 1.6 eV.

Several broad transitions involving $Fe_{oct}(e_g)$ bands have been reported to occur beyond 2.0 eV as depicted in figure 5.3. The broad feature observed experimentally in the UV may be related to strain induced modification of $Fe_{oct}(e_g)$ bands. However, it is noted that the three-phase derivative model is only valid for analysing transitions around one critical point. If a feature is the result of anisotropies of multiple transitions, which may produce RAS signals of different sign, magnitude and width, the three-phase derivative model should not be employed.

5.1.4 Conclusions & outlook

The agreement of the {111}-nanofaceted row reconstruction and polished crystal's RAS spectra with the strain model strongly suggests the modification of bulk-like states. The fully relaxed DFT calculation of the {111}-nanofaceted row reconstruction indicates that the reconstruction exhibits an anisotropic strain gradient. It is concluded that this anisotropic strain gives rise to small anisotropic shifts in energy of bulk-like states which produces the anisotropic optical response. The modification of magnetite's bulk-like states of the polished crystal is suggested to originate from anisotropic strain induced by the maghemite overlayer, which forms in ambient conditions.

Further DFT calculations and the subsequent simulations of RAS spectra can provide insight into the atomic structure of the {111}-nanofaceted row reconstruction and also provide quantitative insight into the bands which are

affected by the strain. Such calculations are out of the scope of the current work as accurately simulating RAS spectra is extremely computationally expensive and time consuming. It would require, for example, a high density of k-points to accurately calculate the band structure, and hence, the optical transitions.

5.2 Optical anisotropy of $SrTiO_3$(110)

$SrTiO_3$ substrates are important for heteroepitaxy and superlattices of multiferroic, perovskite oxides. One particularly interesting aspect is the formation of a Q2DEG at the interface of insulating $SrTiO_3$ and $LaAlO_3$. The work to date exploring the nature of the Q2DEG is detailed in length in section 3.2.1. The treatment of the substrate is a critical step which can influence the interface structure in any hetero-epitaxial system.

For these reasons an investigation of the anisotropic optical response of different $SrTiO_3$(110) surface terminations has been conducted. $SrTiO_3$ and $LaAlO_3$ are both wide-bandgap materials and the Q2DEG is expected to result in transitions appearing in the InfraRed (IR) spectral region [172]. Therefore, RAS has the potential to measure the formation of the Q2DEG *in-situ* during the heteroepitaxy. IR-ellipsometry has already confirmed that the Q2DEG at the $LaAlO_3/SrTiO_3$(110) interface is anisotropic with respect to the [001] and [$\bar{1}$10] directions [92].

As a first step towards such an experiment here the RAS spectra of $SrTiO_3$(110) terminations prepared by different methods is investigated. The preparation procedure includes *ex-situ* chemical cleaning, *ex-situ* annealing in oxygen atmosphere and *in-situ* UHV annealing. It will be shown that different $SrTiO_3$(110) terminations have distinctly different RAS spectra, dominated by surface modified bulk states above the $SrTiO_3$ bandgap. In the

case of the (1×4)[‡] reconstruction a strong IR response originating from a metallic surface state is observed.

An additional motivation is to characterise the optical anisotropy of distinct surface reconstructions. The future simulation of RAS spectra and the comparison to experimental spectra can provide quantitative insight into the structure of specific surface reconstructions.

5.2.1 Experimental details

Undoped $SrTiO_3(110)$ single crystal substrates (MTI Corp.) were used throughout this study. The aim is to investigate the surface optical anisotropy of well defined $SrTiO_3(110)$ surfaces. One difficulty is that a wide range of $SrTiO_3(110)$ surface reconstructions have been observed depending preparation conditions and a single domain reconstruction is difficult to obtain (see section 4.3.3).

Due to the restriction of the experimental setup, only surface reconstructions found by *ex-situ* pre-cleaning procedures and subsequent *in-situ* sputter/anneal cycles and/or UHV annealing from 500 to 1100°C are discussed. The pre-cleaning preparation procedures include UHV annealing of as-received substrates, pre-annealing at 950°C in air and finally chemical cleaning in water (80°C) and HCl(37%):HNO_3(67%) 3:1 mixed acid prior to pre-annealing at 950°C in air [150]. The latter procedure, detailed further in section 4.3.1, produces a well ordered TiO_2 terminated surface region in the case of $SrTiO_3(001)$. Table 5.1 summarises the various treatments, lists the reconstruction observed based on their LEED pattern, as well as gives each preparation a unique naming identifier to be used in the figures showing the corresponding RAS spectra.

The RAS unit, $\Delta r/r$, is equal to $2\frac{r_x-r_y}{r_x+r_y}$. In the presented RAS spectra, x and y correspond to the $[\bar{1}10]$ and $[001]$ directions, respectively.

[‡]STM measurements of the so-called (1×4) reconstruction has revealed that it exhibits (2×4) periodicity. However the '2' LEED spots are extremely dim. Considering that LEED measurements are presented throughout this section, the reconstruction will be named (1×4) for clarity.

ID	Preparation	LEED	Contaminants
No pretreatment, sample as received from supplier			
S1-asreceived	as received	too insulating	C, OH
S1-vac500	500°C UHV annealing, 1h, $<1\times10^{-9}$ mbar	(2×1), c(2×2)	C
S1-vac800	800°C UHV annealing, 1h, $<1\times10^{-9}$ mbar	c(2×2)	C
Sample annealed in air at 950°C for 2h prior loading into the UHV chamber			
S2-air950	as loaded	too insulating	residual C
S2-air950-vac500	500°C UHV annealing, 1h	$\mathbf{(3\times1)}$	
S2-air950-vac750	750°C UHV annealing, 1h, $<1\times10^{-9}$ mbar	(3×1),(1×4)	
Sample etched at 75°C in HCl(37%):HNO_3(67%) 3:1 mixed acid and annealed in air at 950°C for 2h			
S3-chem	as loaded	too insulating	residual C
S3-chem-vac750	750°C UHV annealing, 1h, $<1\times10^{-9}$ mbar	(1×4), (3×1)	
S3-chem-vac850	850°C UHV annealing, 1h, $<1\times10^{-9}$ mbar	(1×4), (3×1)	
S4-chem	as loaded, repeat of S3-chem on new sample	too insulating	
S4-chem-vac500	500°C UHV annealing, 1h, $<1\times10^{-9}$ mbar	(1×4), (3×1)	
S4-chem-Ar-vac1100	$3\times$ Ar sputter/anneal cycle, final UHV anneal at 1100°C, 1h	$\mathbf{(1\times4)}$	
Specific additional modifications to previous samples			
S5-chem	Repeated chemical etch and air anneal of sample S3-chem-vac850	too insulating	
S5-chem-vac500	500°C UHV annealing, 1h, $<1\times10^{-9}$ mbar	(1×4),(3×1)	
S5-chem-vac1000	1000°C UHV annealing, 1h, $<1\times10^{-9}$ mbar	(1×4),(3×1)	
S5-exposed	exposure of sample S5-chem-vac900 to air	disordered	
S5-exposed-vac500	500°C UHV annealing, 1h, $<1\times10^{-9}$ mbar	(1×4),(3×1)	

Table 5.1: Overview of the different sample preparations and achieved surface terminations (from LEED). The ID will be used in the following to refer to individual samples, the colour of the ID corresponds to the colour of the RAS spectra in Figures 5.7-5.14. Conditions which resulted in a single domain surface have been highlighted.

Residual instrumental anisotropies from polarizer nonidealities and strain-related signals from UHV windows have been numerical removed by subtracting averaged zeroline signals from isotropic MgO(001) and Si(111) reference surfaces. There is a remaining uncertainty in the zero line of 0.2×10^{-3} due to sample alignment reproducibility and is indicated as an error bar on the zero line in all figures. XPS, UPS and LEED have been recorded in the Omicron XPS system. All $SrTiO_3$(110) substrates were insulating prior to UHV annealing. Consequently XPS measurements were performed using an low energy electron flood gun (CN10) for charge compensation. In these cases LEED and UPS measurements are missing due to substrate charging issues.

5.2.2 Direct surface de-oxidation

As a first step the direct surface decontamination by UHV annealing was investigated by RAS and XPS (see figures 5.7 and 5.8). As-received substrates already show a distinct RAS spectra with a characteristic minima and maxima at 3.85 eV and 4.45 eV. Due to the insulating nature of as-received substrate, LEED measurements to analyse any residual surface symmetry were not possible at this step. UHV annealing at 500 °C for 1 h creates enough bulk oxygen vacancies, which increase the conductivity [173], to prevent substrate charging and a weak LEED pattern is observed. However, the (2×1) LEED pattern is not well defined and coexists with a superimposed $c(2 \times 2)$ structure. XPS measurements, depicted in figure 5.8, reveal significant carbon contamination remains, with the only substantial change being the removal of a second component in the O 1s core level typically associated with the presence of hydroxide or carboxide groups in the surface region. However, the RAS spectra clearly changes, with a change of the prominent 4.45 eV maxima.

The intrinsic anisotropy of the (110) surface unit cell, combined with potential electric field gradients, strain gradients, coherent uniaxial strain, or localised surface states can all induce a small optical anisotropy in an otherwise optically isotropic material. A strain related RAS signal typically creates structures in the vicinity of a materials bulk critical points. The relationship

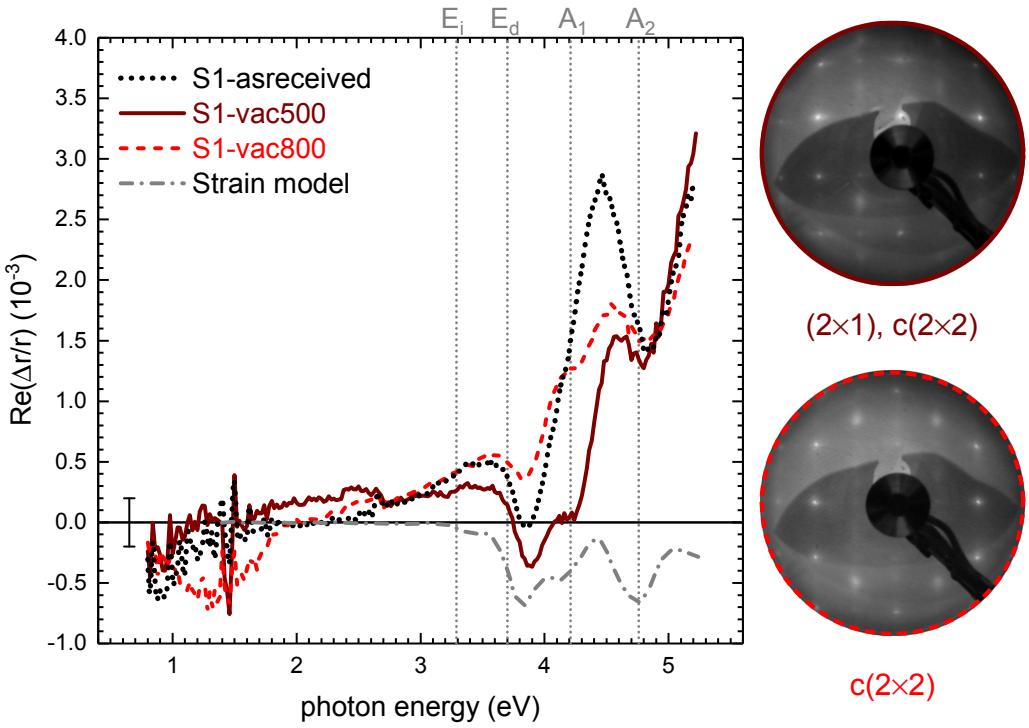

Figure 5.7: RAS spectra of an as-received $SrTiO_3$(110) substrate (••••) and after subsequent UHV annealing for 1 h at 500 °C (——) and 800 °C (- - -). The gray curve (-·-·) estimates the strain induced anisotropy using equation (2.16).

between the bulk dielectric function and RAS structures have been extensively discussed in terms of bulk strain, but also surface and step induced strain in silicon [42, 174]. For the Si(110) surface the resulting spectra are found to be combinations of strain and other effects, and also hydrogen can play a crucial role [38, 174, 175]. For the $SrTiO_3$(110) surfaces investigated here, no detailed calculation on the optical properties of various surfaces, nor detailed adsorption studies exist. Hence we can only discuss spectra with qualitative models, in particular the possible effect of surface induced strain. Within a crude strain model, one can simulate the spectral shape of such strain induced structures via equation 2.16 which relates the real part of the complex RAS quantity to the bulk dielectric function. The bulk dielectric function of the $SrTiO_3$ ($\tilde{\epsilon}_b = \epsilon^{'} + i\epsilon^{''}$) was measured by ellipsometry (Sopra

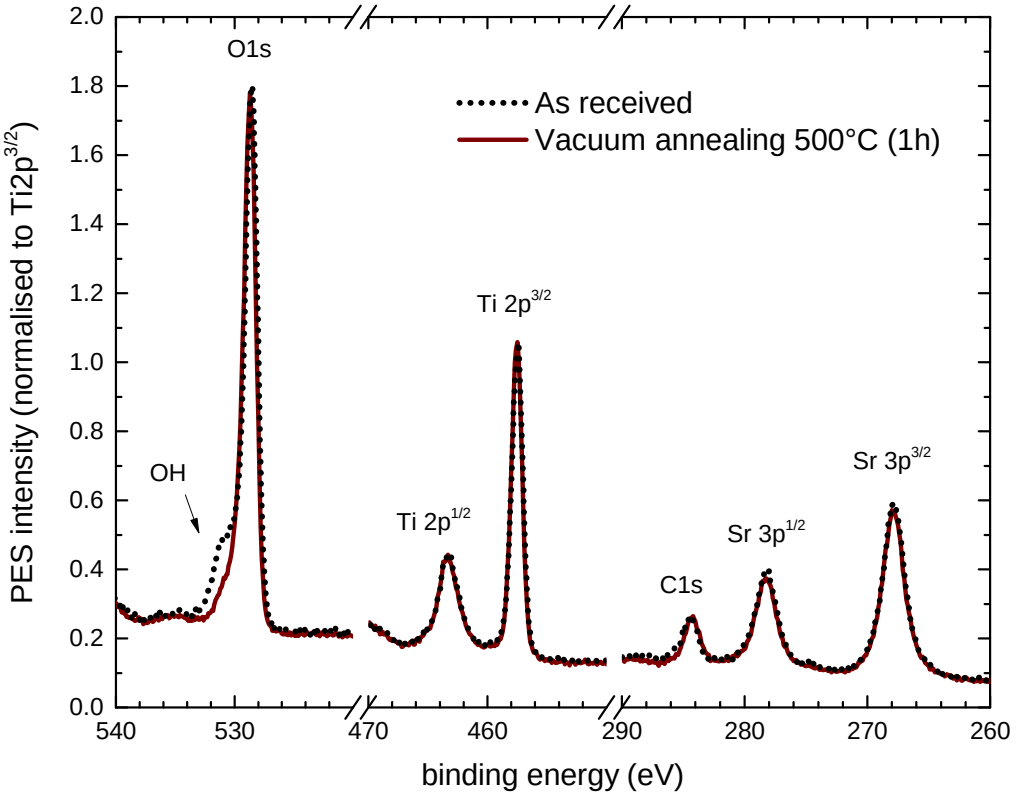

Figure 5.8: XPS spectra of the as-received and 500 °C UHV annealed substrate showing a removal of hydroxide groups.

GESP5) and the measurement is depicted in figure 5.9. The result of this simulation is shown in Fig. 5.7, using a value for d of 12 nm. The latter was chosen to reproduce the amplitude of the minimum structure at 3.9 eV. The simple strain models shows some similarities with the measured structure, particularly just above the direct band gap of $SrTiO_3$ at 3.7 eV. However it fails to describe the structures at other transitions, such as the indirect gap at 3.25 eV and higher energy transitions (A_1, A_2). There are also considerable variations in the reported dielectric function of $SrTiO_3$ due to the ternary nature and variations in oxygen stoichiometry in bulk crystals [83]. Here we use the terminology to label transitions following the work of van Benthem *et al.* [83], while the energetic positions have been determined by analysing the second derivative of ellipsometric measurements of the bulk crystals used in

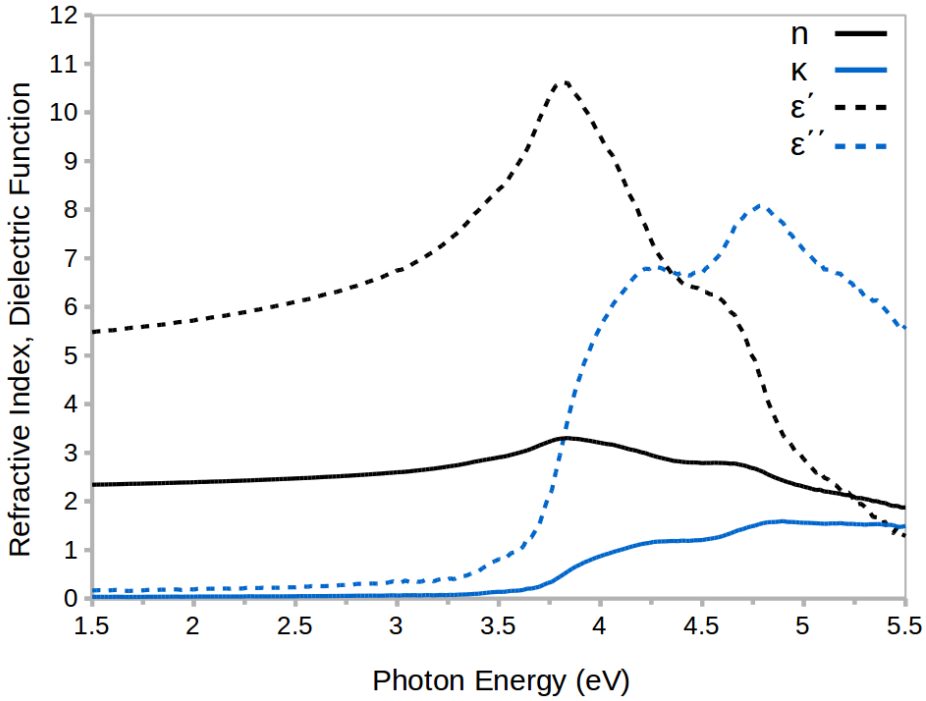

Figure 5.9: Ellipsometry measurement of the $SrTiO_3$ substrate. The real ($\epsilon' = n^2 - \kappa^2$) and imaginary ($\epsilon'' = 2n\kappa$) components of the complex dielectric function are numerically calculated from the the real (n) and imaginary (κ) components of the measured complex refractive index.

this work. They are found to be broadly consistent with those in [83], giving an indirect gap $E_i = 3.29\,eV$; direct gap $E_d = 3.70\,eV$; transition $A_1 = 4.21\,eV$; and transition $A_2 = 4.76\,eV$. These energies are included as vertical lines to guide the eye in all shown RA spectra.

Further UHV annealing at 800 °C for 1 h does not produce a surface with significantly better order, although a weak c(2 × 2) dominates. The RAS shows a further modification of the UV structure and a broad minimum within the bandgap, indicating an increase in point defects within the surface region. To the author's knowledge a c(2 × 2) structure has not been investigated, but the surface is not well ordered, and a significant carbon contamination identified by XPS measurements remains. Sputter/anneal cycles may remove the contamination and produce a surface with a better degree

of order. Sputtering, which preferentially remove Sr, may gave rise to the formation of a different surface structure. This could be mediated by annealing in an oxygen atmosphere. Attempting to achieve a clean, well ordered $c(2 \times 2)$ termination, and subsequent surface characterisation by STM, is a subject of future work. It is noted that the substrate may be too insulating to perform STM experiments. In such an event doped $Nb:SrTiO_3(110)$ substrates, which display significantly higher conductivity, will be investigated.

5.2.3 *Ex-situ* surface pre-cleaning

The family of $(n \times 1)$ reconstructions have previously been prepared by air or oxygen annealing substrates in the temperature range of 900 - 1000 °C for 30 min to several hours [157, 158]. Here, the substrates have been air annealed at 950 °C for 2 h. In addition to the air annealing step a chemical pre-cleaning method, described in the experimental details, has been employed.

RAS spectra after the air annealing show clear differences, depending on whether the chemical etchant step prior to annealing was performed (see figures 5.10(••••) and 5.11(••••)). The substrates were fully insulating at this step and LEED measurements were only possible after a gentle UHV anneal at 500 °C. Figure 5.12 depicts the RAS spectra of the chemically etched and air annealed substrate and subsequent 500 °C UHV anneal. There are no significant changes in the RAS spectra before and after this gentle UHV annealing, indicating the only change is the bulk conductivity, which allows for a LEED pattern to be obtained, and not the surface termination. Therefore, this gentle 500 °C UHV anneal was performed on the insulating chemically etched and air annealed substrate to induce sufficient conductivity so that a LEED pattern could be obtained.

Substrates which were only air annealed only show small changes after the 500 °C UHV anneal (see figures 5.10(••••): the magnitude of the peaks is altered, especially around 4.5 eV. However, the line shape is largely the same. The small changes are likely related to desorption of physisorbed carbon and/or hydrogen residues (see also XPS data in figure 5.8) rather than alterations of the surface reconstruction. The substrates which have

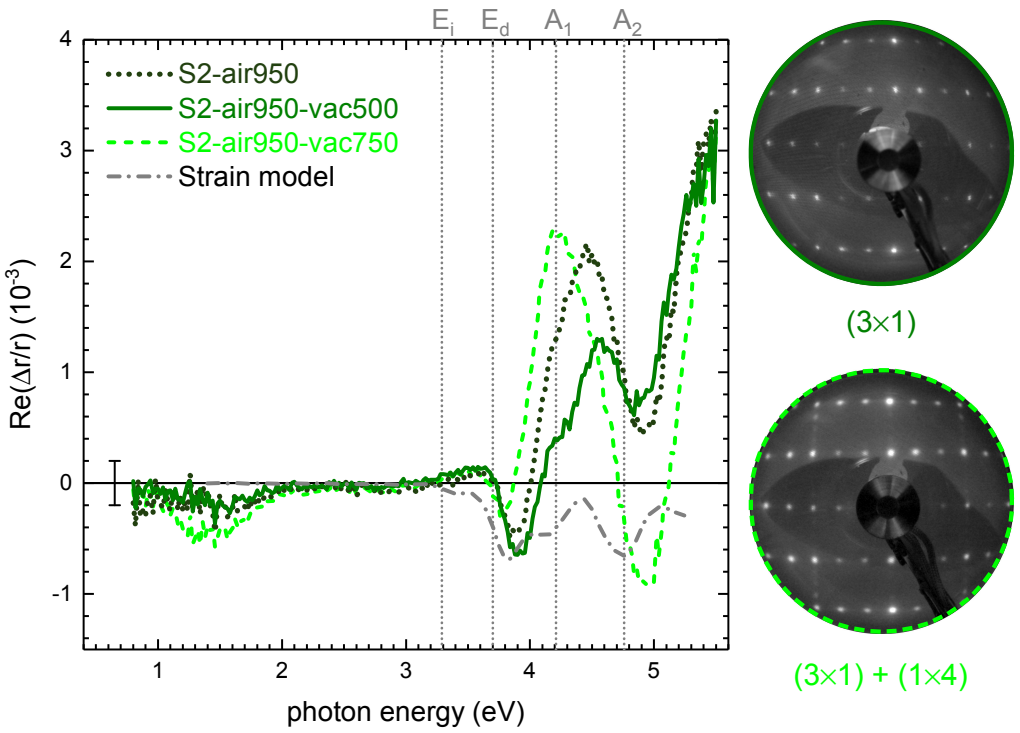

Figure 5.10: RAS spectra of a $SrTiO_3$(110) substrate (••••) after air annealing and subsequent UHV annealing for 1 h at 500 °C (——) and 750 °C (- - -). The gentle 500 °C UHV anneal causes small changes in the RAS signal, with the magnitude of the maxima at 4.5 eV being reduced and shifted slightly. Further annealing at 750 °C results in the shift of the aforementioned maxima and the enhancement of the minima at 4.9 eV. This is correlated to the appearance of dim (1×4) spots in LEED images alongside the (3×1) which is single domain after the gentle 500 °C UHV anneal. LEED images were taken at 60 eV.

only been annealed in air at 950 °C are therefore suggested to be (3×1) terminated and exhibit a single domain.

The (3×1) RAS spectra is characterised by a sharp minima at 3.90 eV and strong positive signal above around 4.1 eV (figure 5.10(——)). Enterkin *et al.* [117] concluded that the $(n \times 1)$ reconstructions $(n = 1\text{-}6)$ are all related. Indeed there is very little difference in the RAS of the sharp (3×1) and the mixed $(2 \times 1)/c(2 \times 2)$ surface (S2-air950-vac500, S1-vac500). Only the level around the A_1 transition differs. Both spectra show the characteristic

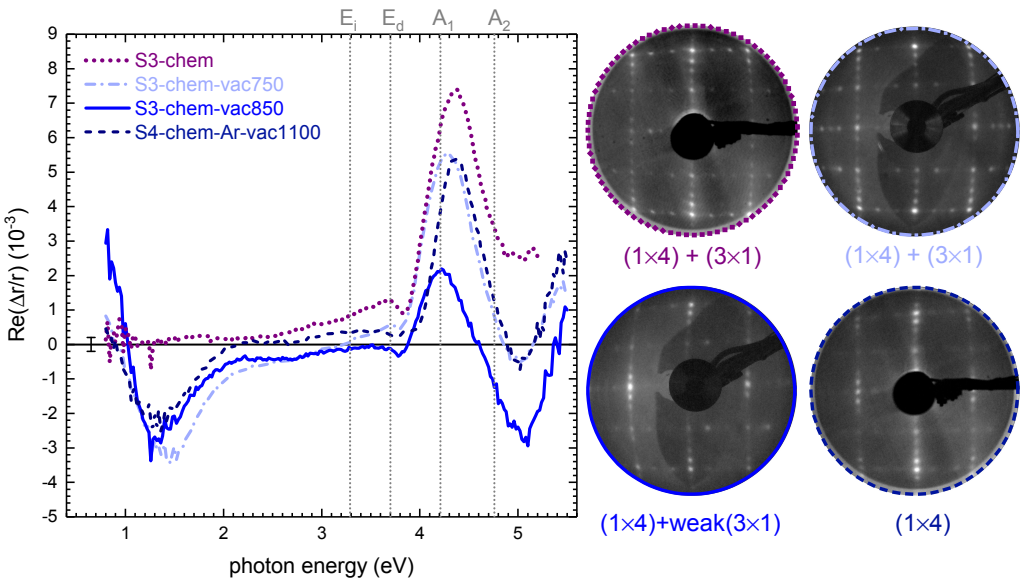

Figure 5.11: RAS spectra of an air annealed substrate which was pre-etched by an HCl(37%):HNO_3(67%) 3:1 mixed acid (••••) and further stepwise annealed at 750 °C (-·-·-), 850 °C (——), and finally after combined Ar^+ sputtering and 1100 °C anneal (- - -). Annealing progressively reduces the UV structure while the Ar^+ sputtering and annealed substrate displays an intermediate UV-structure. Additionally, annealed substrates exhibit a structure in the $SrTiO_3$ bandgap. The pre-etched and annealed substrate is a mixed state of (3×1) and (1×4) and progressive UHV annealing reduces the (3×1) spot intensity while the sputtered and annealed substrate shows the most dominant (1×4) pattern. The LEED images were taken at 60 eV.

minima at 3.9 eV, just above the direct gap E_d. As previous STM work and DFT studies for the (3×1) show a distinct row structure [117, 158], and the RAS fine structure within the rising slope in the UV is reproduced by the simple strain model, the RAS of these two surfaces is likely to be dominated by the anisotropic strain of the row reconstruction to the underlying $SrTiO_3$ bulk.

Further annealing in UHV at higher temperatures lead to a blurring of the (3×1) reconstruction and appearance of weak (1×4) spots suggesting a coexistence of a (3×1) and (1×4) termination. This termination has been previously referred to as "(3×4)" LEED pattern [157] and it was already

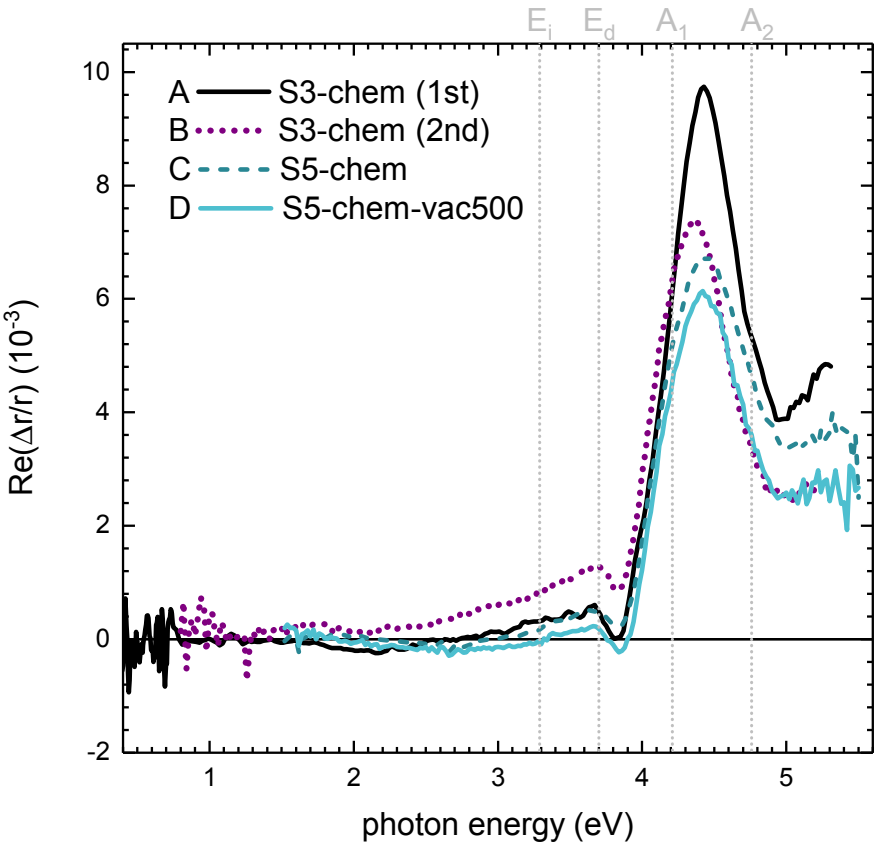

Figure 5.12: Comparison of RAS spectra after alternating etch/air anneal cycles (A, B), and an etch/air anneal cycle (C) after a UHV anneal (C), illustrating the variation in the RAS spectra caused by varying (3×1) to (1×4) area ratios and overall surface order. Spectra D was taken after a gentle UHV 500 °C anneal, showing similar variations to substrates only chemically etched and air annealed. For this substrate LEED measurements have been possible (image shown in Fig. 5.11(····)) illustrating that etch/air annealed surface have a mixed (3×1) to (1×4) termination prior to any *in-situ* UHV annealing.

suggested by STM studies of Russell *et al.* [158] that this related to two different terminations coexisting. In terms of the RAS spectra the appearance of the (1×4) spots is accompanied by an intense maxima/minima structure at the A_1 and A_2 transitions. In the following we will show that modifications of our heating stage, combined with chemical pre-treatment allows for

the preparation of a almost single domain (1×4) reconstructions and we will discuss its details in the following section.

In sharp contrast to air annealed substrates, substrates pre-etched in the HCl(37%):HNO_3(67%) 3:1 mixed acid show a mixed (3×1) and (1×4) terminated surface prior to any UHV annealing (see figure 5.11(••••)). This is likely related to the preferentially removal of Sr by the chemical etching [150]. Upon UHV annealing above 600 - 700 °C the relative intensity of the (3×1) spots gets weaker compared to the (1×4) spots, indicating a change in the area ratios of the two reconstructions. Substrates which underwent sputter/anneal cycles prior to 1100 °C UHV annealing showed the most dominant (1×4) pattern (figure 5.11(---)). This is consistent with the (1×4) reconstruction being Sr deficient as sputtering results in a Ti rich surface region [152, 162, 163]. For the sputter/anneal cycles the substrates went through three cycles using Ar-ions (0.6 kV, 1×10^{-5} mbar for 20 min and 500 °C anneal for 20 min) prior to extended UHV annealing to 1100 °C. The RAS spectra for all the etch/air annealed substrates are a linear combination of the (3×1) and (1×4) spectra with varying ratios, complicating the analysis significantly. The (1×4) contribution is dominated by a large maximum around 4.4 eV in the vicinity of the A_1 transitions. The minimum structure, dominating the (3×1) and (2×1) RAS is still present, though less dominant due to the much larger maximum at 4.4 eV (please note the significant change in scale between Figures 5.10 and 5.11).

With increasing temperature the relative contribution of the (1×4) termination increases, but LEED images also start to blur and an additional minima RAS-structure at 1.4 eV evolves within the $SrTiO_3$ bandgap. The latter is not directly proportional to the (1×4) area as it is also seen for the more disordered c(2×2) reconstruction. The below bandgap RAS features will be discussed separately below. The RAS features above the bandgap can now be understood as linear combinations of the (3×1) RAS spectra (S2-air950-vac500) and the (1×4) (S3-chem-vac850) with varying ratios between (3×1) and (1×4) contributions.

5.2.4 Below bandgap structures

For all high temperature annealed surfaces (T>700 °C) there is a non-negligible RAS minima developing in the 1.2-1.6 eV region. It initially manifests as a minimum but as it increases amplitude is also accompanied by a sharply rising slope towards the IR and we expect the signal to rise further below 0.8 eV. We link the appearance of this infrared signature with the formation of a substantial number of oxygen vacancies within the sample, creating defect states responsible for a) an effective doping of the material with electron accumulation at the surface and b) for mid-gap states leading to non-vanishing absorption below the band gap, and hence new features in this range. Indeed an absorption feature at 1.3 eV seen in $SrTiO_3$ homoepitaxial thin films, grown in oxygen poor conditions was linked to the formation of Sr-O-O vacancy complexes [176]. Already the bulk conductivity of $SrTiO_3$ itself has been related to oxygen vacancy formation [173]. Recently it was shown that oxygen vacancies in $SrTiO_3$ cluster into vacancy rows along the [001] direction [177]. It is reasonable to assume that the formation of oxygen vacancies is therefore linked to the appearance of the infrared related RAS features, and possibly even be related to the formation of the (1×4) reconstruction itself, in the same way as ordered surface or sub-surface oxygen vacancies have been found in other surface reconstructions of transition metal oxides such as TiO_2 and Fe_3O_4 [106, 110, 178].

Figure 5.13 illustrates that the appearance of the IR structure in the RAS correlates with the appearance of defect states close to the Fermi edge and changes in the Ti 2p core level. These changes are consistent with an increase in the amount of Ti^{3+} sites and possibly a small increase in Ti^{2+} sites, but no metallic Ti^0 [163, 173]. Simultaneously the high temperature annealing alters the valence band structure, which is characterised by two peaks at approximately 5 eV and 7 eV relative to the Fermi level [173]. Annealing to 850 °C (—), which increases the Ti^{3+} and metallic state contributions, is accompanied by the reduction of the valence band peak at ∼5 eV, which is correlated to almost pure oxygen state [179], and modification to the structure around 9-10 eV (indicated by the two red arrows in figure 5.13). The structure around

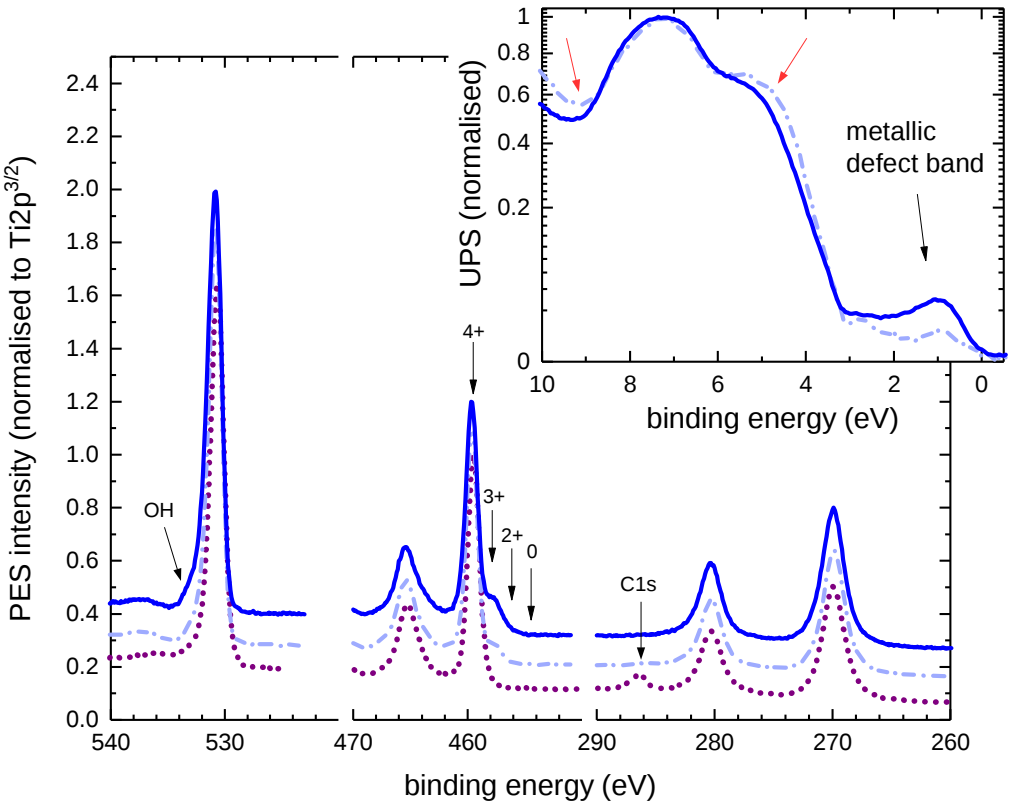

Figure 5.13: UPS and XPS spectra for a etched and air annealed substrate (····), followed by UHV annealing at 750 °C (- - -), and 850 °C (—). Corresponding LEED and RAS are depicted in figure 5.11. The creation of oxygen vacancies leads to an increased bulk conductivity and alterations in the Ti oxidation state with the spectral weight of Ti^{3+} increasing. This is correlated with the formation of a metallic defect band seen in UPS spectra (inset). The 850 °C UHV anneal (—) results in modification to the valence band structure relative to the 750 °C UHV anneal (- - -), highlighted by the red arrows. The 850 °C UHV anneal entirely removes any measurable carbon contamination but generates a small shoulder in the oxygen 1s peak, possibly related to hydroxides in the surface region.

9-10 eV is correlated to a peak at ∼11 eV, which has been attributed to a carbon 2s peak [179]. Therefore, the modification of the structure around 10 eV, in particular the lower counts for higher temperature annealing, is reasonable as the higher temperature anneal reduces the carbon 1s contribution seen in the XPS measurements. The modification of the valence band struc-

ture, as highlighted by the red arrows, has been observed via sputtering by Henrich *et al.* [173]. Furthermore, Psiuk *et al.* observed similar valence band modification, a metallic defect state in the bandgap and reduction in the Ti oxidation state upon sputtering [163]. Sputtering [163], like UHV annealing [158][§], is reported to increase the relative Ti contribution, and hence, result in reduced Ti oxidation states [163]. Finally, high temperature annealing induces a small shoulder in the O1s component, which may be due to presence of hydroxides in the surface region. Such contamination may gave rise to the slight deteriorates of the surface order, determined by LEED, observed after high temperature annealing (see figure 5.11).

For annealing steps up to 850 °C the creation of the oxygen vacancies does not directly alter the surface termination, except for a slight decrease in the (3×1) spot intensity and increased surface disorder seen by the blurring of LEED spots, however, it creates defect states and free carriers within the $SrTiO_3$. The change is significantly more dramatic in the RAS spectra, where the response below 2 eV is substantially altered, even if the defect state in the UPS spectra is still very small. In figure 5.13 a square root scaling of the normalised counts has been used to illustrate the defect band is present for the 750 °C annealed substrate as it is significantly smaller than that of further annealing steps. In contrast the RAS amplitude for the same surface at 1.4 eV is already comparable to that of further annealing steps. As RAS measures the ratio of the difference in dielectric response for the $[\bar{1}10]$ and [001] directions normalised by the average bulk reflectivity, it is difficult to directly interpret RAS amplitudes in a quantitative manner; increased density of oxygen vacancies and associated increased substrate conductivity will also alter the bulk reflectivity of the substrate. However, qualitatively it is clear that RAS is very sensitive to the formation of the electron gas.

The presence of a near surface electron gas or metallic surface states, as clearly seen in the UPS data, is also expected to directly lead to a free electron like response in the infrared region of any optical spectra. For RAS

[§]Ti is enriched by UHV annealing if the annealing temperature is below around 1200°C [158]. At higher temperatures the Sr relative concentration increases [158], which is likely related to the onset of Sr diffusion at these high temperatures [154].

measurements, in contrast to simple reflectance measurement, such a free electron response can create an apparent minimum in the difference structure related to $\varepsilon_x - \varepsilon_y$, even if both ε_x and ε_y are rising monotonically towards the IR [172]. The simulation in Fig. 5.14 illustrates a possible line shape for such a free electron response using equation (2.15) with two Drude dielectric functions, ε_x and ε_y, with the same plasma frequency but anisotropic scattering rates. The simulation is only indicative, as the spectral range was not wide enough for any form of quantitative fits, however a three times higher mobility for the $[1\bar{1}0]$ (here x) compared to the [001] direction was used, consistent with the experimentally found mobility anisotropy in the $SrTiO_3/LaAlO_3(110)$ interface [92]. The observed RAS structure is however most likely a combination of an anisotropy in the polarisability of the near surface oxygen vacancy related mid gap states and the free carrier contribution.

The question of the spatial origin of this conductance anisotropy arises. Pre-etched surfaces UHV annealed at 500 and 750 °C (see figure 5.11, (••••) and (- - - -)) have very similar LEED patterns, indicating no change in surface termination, but show significantly different IR-RAS responses. This suggests that the infrared RAS signal is more likely to originate from bulk oxygen vacancies rendering the $SrTiO_3$ conductive rather than direct surface alterations. In this case either the surface induced strain gradient leads to an anisotropic signal in the near selvedge bulk area, or carriers accumulate at the surface in a quasi two-dimensional sheet and we observe an anisotropy in the 2D carrier mobility due to the anisotropic surface termination.

In an attempt to distinguish if the IR-RAS signal originates from the surface layer or a near-selvedge modified bulk, substrates have been exposed to air and remeasured. As seen in figure 5.14, air exposure almost fully quenches the RAS minima at 1.4 eV. However, the RAS amplitude in the UV increases, and therefore it is concluded that the surface induced modification of the near-selvedge bulk is still present. The disappearance of the IR response therefore indicates that it originates from the topmost layers and not from a near-selvedge bulk as with the UV-RAS. Upon gentle annealing at 500 °C the RAS almost fully recovers. Similar annealing conditions on

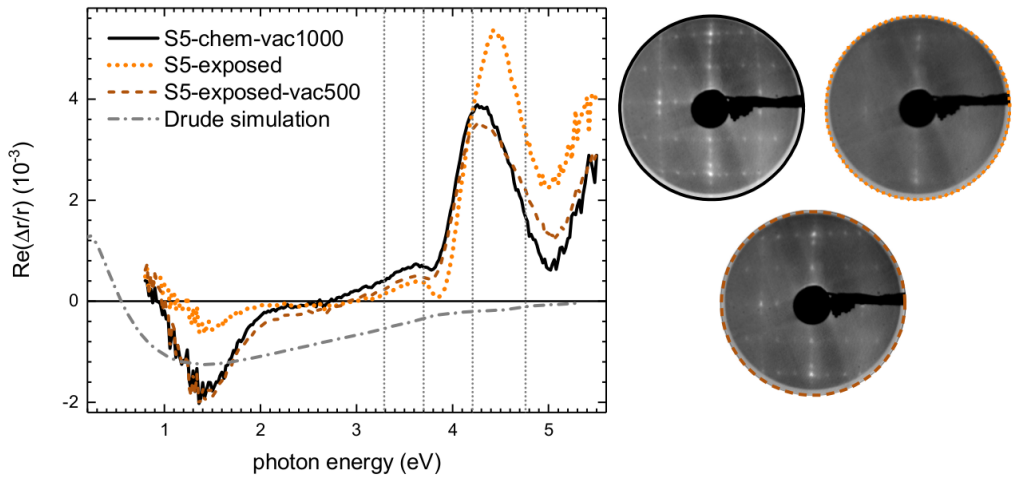

Figure 5.14: RAS spectra and LEED image of a 1100 °C UHV annealed surface prior to (—) and after (····) air exposure. After exposure the IR feature is nearly entirely quenched indicating the anisotropic conductance originates from the topmost layers. Subsequent annealing at only 500 °C (- - -), which is not a sufficiently high temperature to induce the formation of the anisotropic conductance response in the IR (see figure 5.12), causes the full recovery the original IR structure. The simulation (- · - · -) illustrates a possible free electron contribution to the overall RAS signal.

substrates without any bulk conductivity (see figure 5.12) doesn't create an IR signal, and hence, we do not increase the conductivity to form the IR signal but rather remove physisorbed species and recover the original surface symmetry and correlated anisotropic mobility in the terminating layers.

In the case of the $LaAlO_3/SrTiO_3(110)$ interface the enhanced mobility is anisotropic and is concluded to be a result of oxygen vacancies in the $SrTiO_3$ [92], in agreement with the results presented here. The Q2DEG which forms at the $LaAlO_3/SrTiO_3$ interface is the result of both interface effects (discussed below) and strontium titanate oxygen vacancies which form during the growth of $LaAlO_3$ [19]. Typically growth conditions for the $SrTiO_3/LaAlO_3$ interface exceed 750°C (approximately the temperature at which the anisotropic conductance is observed in this work), above the onset temperature for the formation of a significant number of oxygen vacancies

[180]. This is typically mitigated by a sample cool down at higher oxygen pressures (up to 200mbar), which was not possible in our system.

5.2.5 Conclusions & outlook

It has been illustrated that RAS measurements of $SrTiO_3$(110) surfaces are sensitive to the surface reconstructions and the formation of a Q2DEG present in UHV annealed substrates. Different surface treatments alter the surface order, indicated by different RAS spectra. Substrates directly annealed in air result in a single domain (3×1) seen after moderate subsequent UHV annealing, while substrates pre-etched in HCl:HNO_3 mixed acid already show a $(3 \times 1) + (1 \times 4)$ mixed surface, likely related to preferential Sr removal by the etching. Most surface termination related changes in the RAS spectra occur in the UV above the $SrTiO_3$ bandgap. The comparison of the RAS spectra with the strain model indicates that small anisotropic shifts in energy of the optical transitions, associated with anisotropic strain, are responsible for the response in the UV.

The IR signal related to the electron gas is surface localised, with RAS being even more sensitive to its formation than UPS. The IR signal is concluded to be a combination of mid-gap states due to oxygen vacancies in the surface region and a free-electron response. The sensitivity towards the electron gas is encouraging for future work on $SrTiO_3/LaAlO_3$ interfaces, as it can be employed *in-situ* during the growth of heterostructures to measure the properties of the interface localised electron gas while it is formed. The Q2DEG is reported to only form at some $LaAlO_3$ critical thickness [88, 89]. However, electrical measurements are performed *ex-situ* and oxidation may influence the interface properties especially at small $LaAlO_3$ thickness, as demonstrated by the exposure experiment depicted in figure 5.14. Additionally, the termination of the $SrTiO_3$ substrate strongly influences the electronic properties at the interface [94]. Several studies employ *ex-situ* pretreatment prior to heterostructure growth, to attain a desired termination. However, the influence of the growth conditions on the substrate termination does not appear to be considered. Many of the $SrTiO_3$ terminations have

been characterised in this work, and RAS provides a tool which can monitor the termination prior to and during growth. $LaAlO_3$ exhibits a bandgap of ∼5 eV, compared to ∼3.3 eV of $SrTiO_3$, and hence, the influence of the $LaAlO_3$ growth on the $SrTiO_3$ substrate can be monitored, as contribution to the RAS below ∼5 eV will likely be due to the $SrTiO_3$ substrate. RAS has the potential to provide insight into the dependence of the Q2DEG on the $LaAlO_3$ thickness, the $SrTiO_3$ termination and the heterostructure growth conditions and post-growth treatment.

5.3 Discussion

To the author's knowledge this work represents the first *in-situ* RAS study of oxide surface reconstructions. The investigation of the (110) surfaces of polar, bulk isotropic Fe_3O_4 and $SrTiO_3$ demonstrates that RAS is sensitive to the influence the surface structure has on the underlying near-selvedge bulk. Anisotropic strain gradients are suggested to be the root cause of the RAS signals.

The ease at which preparation procedures can alter the stoichiometry of metal oxide surface regions, and in the case of polar terminations the need to compensate for their polarity, leads to metal oxides often exhibiting non-stoichiometric and/or faceted reconstructions. Such reconstructions will alter the underlying stoichiometric bulk most simply in the form of strain.

In the case of wide bandgap $SrTiO_3$, RAS is extremely sensitive to the formation of an anisotropic conductance in the IR. As with Fe_3O_4(110) and UV-$SrTiO_3$(110), the response owes its anisotropy to the influence of the anisotropic surface termination.

Although the optical anisotropy of the {111}-nanofaceted row reconstruction of Fe_3O_4(110) is sensitive to the influence the reconstruction has on the near-surface bulk, it provides insight into surface sensitive STM observations: 1D surface states are understood in terms of the 1D compressive and tensile strain in the terminating layer (section 6.2.2) and the (1×3) periodicity opposed to larger unit cell size (which would increase the {111} coverage) is understood as the balance between energetically favourable {111} cover-

age and the associated strain energy (section 6.2.4). This work therefore demonstrates the potential of combining surface sensitive techniques with RAS measurements, which are sensitive to the influence the termination has on the bulk-region in the vicinity of the selvedge.

Chapter 6

$Fe_3O_4(110)$: {111}-Nanofaceted Row Reconstruction

The samples studied in this chapter (the same crystals are those investigated in section 5.1) were polished float zone grown single crystals with a measured T_V of 122 ± 1 K. Once the crystal was introduced to the UHV chamber, several sputter/anneal cycles were performed. Annealing can lead to the diffusion of contaminants to the surface [115, 130] and these contaminants are removed by sputtering [113, 115]. A sputter/anneal cycle consists of sputtering with argon cations ($\sim 2 \times 10^{-5}$mbar) with an energy of 0.5 - 0.7 keV for 20 minutes and subsequent annealing in vacuum at $\sim 600\,^{\circ}$C for 20 minutes.

It is noted that sputter/anneal cycles will give rise to an oxygen deficient surface region as sputtering preferentially removes lighter oxygen atoms [108, 138]. Annealing in an oxygen atmosphere can produce a magnetite-like stoichiometry. As depicted in figure 3.1, the oxygen partial pressure and temperature dictate which iron oxide phase is stable. An alternative method of forming a magnetite-like surface stoichiometry is to expose the crystal to atmospheric conditions and subsequently anneal the crystal in a UHV atmosphere. Atmospheric conditions will lead to the formation of a surface layer of maghemite [36], and annealing in UHV at temperatures between around 550 and 950 °C will cause the surface region to be converted to magnetite [52].

The following study was conducted between an XPS and STM chamber and RAS measurements have been performed in the latter chamber. Two crystals from the same batch have been used in this study; STM and XPS measurements were performed on a small crystal while RAS measurements were performed on a larger crystal, which provides a better reflection. *In-situ* temperature measurements inherently exhibit errors as the heating and temperature measurement mechanism in each chamber differs: in the XPS chamber the temperature is estimated by a K-type thermocouple. While in the STM chamber - in which heating in performed by a combination of resistive and electron beam heating - the sample temperature is estimated by a pyrometer ($\epsilon = 0.85$ throughout). LEED, which both chambers are equipped with, is used to qualitatively compare cleaning procedures. Throughout this chapter, the STM tips used were [001] orientated tungsten which were electrochemically etched in NaOH. The bias voltage is applied to the surface with respect to the tip. STM experiments were conducted at 78 K.

Recently, Parkinson *et al.* [143] concluded that the (1×3) row reconstruction was a result of periodic nanofaceting which exposed {111}-like planes. STM line profiles demonstrated a maximum height difference between the ridge and trough of 4 Å. And hence, the ridge-to-trough depth is at least 4 Å. True height differences of the reconstruction are practically impossible to probe with STM: an STM tip typically has a radius of curvature of tens of nanometers, and therefore the tunneling current when the tip is above the trough will be the sum of contributions from the trough and other segments of the reconstruction. Therefore, STM will underestimate the depth. Nevertheless, line profiles perpendicular to the row direction will shows a height difference between the ridge and trough of several Ångström.

This reconstruction has the potential to provide a template for the growth of 1D nanostructures. The understanding of its structural and electronic properties is paramount to explore this potential.

6.1 Annealing environment

In this section the influence of different annealing environments is explored. As was discussed in the previous paragraph, sputter/anneal cycles were performed to remove bulk contaminants. In chapter 7 the influence of sputtering prior to annealing is investigated. To avoid the possibility that sputtering influences the surface structure in this chapter, the crystal was always exposed to atmospheric conditions prior to annealing in the UHV chamber.

Annealing (110) terminated single crystalline and thin film magnetite in UHV [137–139, 141, 143] and oxygen [143] environments results in the formation of a (1×3) row reconstructed surface. The row reconstruction has been reported to be formed by annealing in UHV at temperatures ranging from 600 °C [143] and 930 °C [138].

XPS measurements performed by Parkinson *et al.* revealed that annealing at 630 °C in UHV and oxygen environments ($5\text{x}10^{-7}$ mbar) produces a surface region with a magnetite-like Fe^{2+}/Fe^{2+} ratio*. However, the surface with the best degree of order, which exhibits rows running for hundreds of nanometers without breaking, was prepared by annealing at 800 °C in UHV. On the basis of the aforementioned XPS and minor differences in LEED, it was commented that the oxygen and UHV annealed crystals likely exhibit different surface structures.

6.1.1 X-ray photoelectron spectroscopy

The Fe_3O_4(110) single crystal has been annealed in UHV and oxygen (3×10^{-6} mbar) atmospheres for 1.5 h at 800 °C and the corresponding XPS spectra and LEED images are depicted in figure 6.1.

By comparing the LEED images obtained in the XPS and STM chamber, the latter being calibrated†, the reciprocal space unit cell can be overlayed atop the LEED images. The green rectangle in figure 6.1 corresponds to the Fe_3O_4(110) reciprocal space unit cell, whose lengths are proportional to $\frac{1}{8.4}$ and $\frac{1}{6}$, respectively (see figure 4.2).

*This is the authors interpretation of the Fe 2p lineshape

†The LEED is calibrated by an Ag(111) surface confirmed by STM.

The greater intensity of even order rows (including zero order) is the result of the linear combination of periodicities of the unit cell length and half the unit cell length. For the [$\bar{1}$10] direction this corresponds to 6 and 3 Å. Note that oxygen atoms on both planes of (110) terminated magnetite are separated by 3 Å along the [$\bar{1}$10] direction (see figure 4.2).

Along the [001] surface direction of the UHV annealed crystal, three spots are identified within the unit cell length, indicative of the (1×3) row reconstruction. There are no defined spots along the [001] direction of the oxygen annealed crystal. The oxygen annealed surface is rougher and/or less ordered. This indicates that of the preparation procedures considered here only the vacuum anneal sees the formation of a well ordered {111}-nanofaceted row reconstruction.

The iron $2p_{3/2}$ and $2p_{1/2}$ peak positions of Fe_3O_4 are located at binding energies of 710.5 eV and 723 eV, respectively [181, 182]. The Fe $2p_{3/2}$ peak is the sum of Fe^{2+} and Fe^{3+} components whose peaks reside at 708.5 eV (blue dashed line in figure 6.1) and 710.5 eV (red dashed line in figure 6.1), respectively [181–183]. Fe_3O_4 has a Fe^{3+}/Fe^{2+} ratio of 2, hence the Fe $2p_{3/2}$ peak is positioned at the Fe^{3+} component and a shoulder resides at the Fe^{2+} component [182].

As the Fe^{2+} content is reduced the Fe $2p_{1/2}$ peak shifts to higher binding energies, with the peak residing at 724 eV for γ - Fe_2O_3 (maghemite) which contains zero Fe^{2+} ions [181]. $Fe_{1-x}O$ (wüstite) exhibits a Fe $2p_{3/2}$ satellite peak at $\sim$716 eV and its $2p_{3/2}$ peak is shifted to lower binding energies (709.5 eV) [182]. These features are attributed to the increased Fe^{2+} content of $Fe_{1-x}O$.

The spectra of the UHV and oxygen annealed surface regions correspond to raw counts without any modification. The Fe/O ratios have been calculated by integrating the O 1s and Fe $2p_{3/2}$ peaks. The two peaks were fitted with three components each. This yielded a Fe/O ratio of 0.73 for the oxygen annealed crystal (red spectra in figure 6.1), which is within the systematic error of stoichiometric Fe_3O_4. This is satisfactory as the line shape with peaks at 723.5 eV and 710.5 eV, a small shoulder at 708.5 eV and the absence of satellite peaks is indicative of stoichiometric magnetite [181, 182]. This is

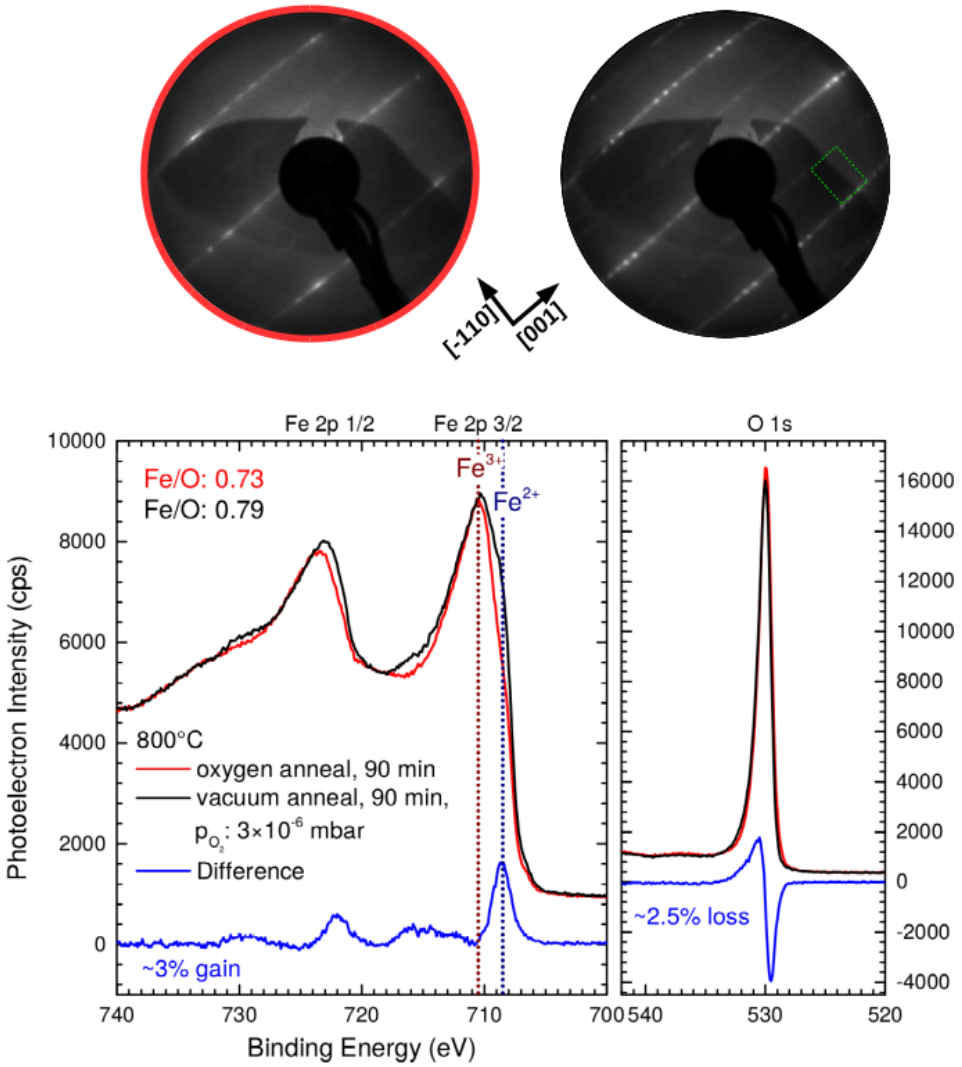

Figure 6.1: Red and black curves represent the oxygen ($3\text{x}10^{-6}$ mbar) and UHV annealed crystal at a temperature of 800 °C for 1.5 h. The blue curve represents the difference spectra, corresponding to black minus red. The Fe $2p_{3/2}$ peak consists of Fe^{3+} and Fe^{2+} components whose energies are represented by the red and blue dotted vertical lines, respectively. The Fe/O ratios of the UHV and oxygen annealed surface regions are determined to be 0.79 and 0.73, respectively. These ratios are calculated by integrating the area under the Fe 2p and O 1s line-shapes. It is clear from the peak at 709.5 eV in the difference spectra that the UHV annealed surface region has a larger Fe^{2+}/Fe^{3+} ratio. LEED images, obtained at 100 eV, indicate the vacuum annealed crystal exhibits an ordered (1×3) row reconstruction while the oxygen annealed surface exhibits a row reconstruction but with a weak degree of ordering.

extremely similar to the lineshape presented by Parkinson *et al.* [143], who annealed a single crystal at 630 °C in an molecular oxygen partial pressure of 5×10^{-7} mbar.

The Fe/O ratio of the UHV annealed crystal (black spectra in figure 6.1) is calculated to be 0.79. What is important to note is the change relative to the stoichiometric line-shape and Fe/O ratio, and not the absolute magnitude. The Fe core-level spectra exhibit three differences (highlighted by the blue difference line in figure 6.1) compared to the oxygen annealed surface region:

1. The shoulder at 708.5 eV (blue dash vertical line) is considerably larger.
2. In the range of 716 eV a small satellite peak is present.
3. The $2p_{1/2}$ peak is shifted to a lower binding energy.

(1) and (2) can be attributed to a higher Fe^{2+} content: the largest peak in the difference is clearly positioned at the Fe^{2+} contribution to the $2p_{3/2}$ peak. Secondly, the difference at $\sim$716 eV is positioned at the satellite peak position observed in $Fe_{1-x}O$ which is Fe^{2+} dominant [182]. (3) can be understood by considering the γ-Fe_2O_3 and Fe_3O_4 $2p_{1/2}$ peak positions: as γ-Fe_2O_3 is reduced to Fe_3O_4 the peak shifts to lower binding energies [181]. The Fe^{2+}/Fe^{3+} ratio for γ-Fe_2O_3 and Fe_3O_4 are zero and 1/2, respectively. Therefore, the shift of the $2p_{3/2}$ peak to lower binding energies is indicative of a shift to a higher Fe^{2+}/Fe^{3+} ratio.

The question arises as to the mechanism behind the increased Fe/O and Fe^{2+}/Fe^{3+} ratios for the UHV annealed surface region relative to the stoichiometric oxygen annealed surface region. Clearly, the Fe/O ratio can increase due to oxygen deficiencies, increased iron content or a combination of both. The bulk defect chemistry is iron defect and interstitial dominant, the oxygen FFC sublattice remains largely intact [143]. The oxygen partial pressure and temperature dictates whether defects or interstitials are dominant [184]. A magnetite reconstruction which contains interstitial iron has been reported [99]: the $(\sqrt{2} \times \sqrt{2})$R45 ° reconstruction of (001) terminated magnetite is stabilised by a combination of sub-surface Fe_{oct} vacancies and interstitial sub-surface Fe_{tet} cations [99]. XPS measurements of that termination do not

show a significant relative increase in Fe^{2+}, like that which is seen with the reconstruction discussed here. A termination composed entirely of iron is not expected to be stable at high temperatures as iron is reported to diffuse into the bulk at 227 °C, although the diffusion dynamics depend on the surface region stoichiometry [109].

Considering the faceted nature of this reconstruction, we must consider the possibility of defects on the {111} and {110} sections. Starting with $Fe_3O_4(111)$: the reported terminations include the regular termination (Fe_{tet}), a Fe_{oct} termination which coexists with the regular termination in reducing conditions, a bi-phase (Fe_3O_4 & $Fe_{1-x}O$-like) termination which forms under very reducing conditions and a $Fe_{1-x}O$-like termination which forms when the bi-phase termination is further reduced. The the best of the authors knowledge, XPS measurements (see figure 6.2, taken from Paul *et al.* [101]) have only been performed on the regular and $Fe_{1-x}O$-like terminations. The regular termination exhibits a Fe 2p lineshape comparable to the stoichiometric-like oxygen annealed crystal depicted in figure 6.1(—). While the $Fe_{1-x}O$-like termination (termed "superstructure 3" by Paul *et al.* [101] in figure 6.2) shows a strong satellite at ∼716 eV indicative of increase in Fe^{2+} contribution, a drop in intensity at ∼718 eV indicative of decrease in the Fe^{3+} contribution and a shift of the Fe 2p 3/2 & 1/2 peaks to lower energies. These features are all in line with a $Fe_{1-x}O$-like selvedge. These features are comparable to that of the UHV annealed crystal in figure 6.1(—). However, the changes relative to the stoichiometric lineshape are not as dramatic in the work presented here. For example, there is no decrease in the counts at ∼718 eV and no shift in the Fe 2p 3/2 peak. Furthermore, the $Fe_3O_4(111)$ $Fe_{1-x}O$-like termination forms under extremely reducing conditions, such as several sputter anneal cycles without an oxygen anneal [101]. These conditions are not comparable to the preparation procedure (800 °C UHV anneal performed after a 800 °C oxygen anneal) which generated the lineshape seen in figure 6.1(—). Evidently reduction of the {111} facets can contribute towards the increased Fe/O and Fe^{2+}/Fe^{3+} ratios. A $Fe_{1-x}O$-like {111} termination is ruled out on the basis of the XPS lineshape and the preparation procedure. However, other reduced terminations are candidates. The lack

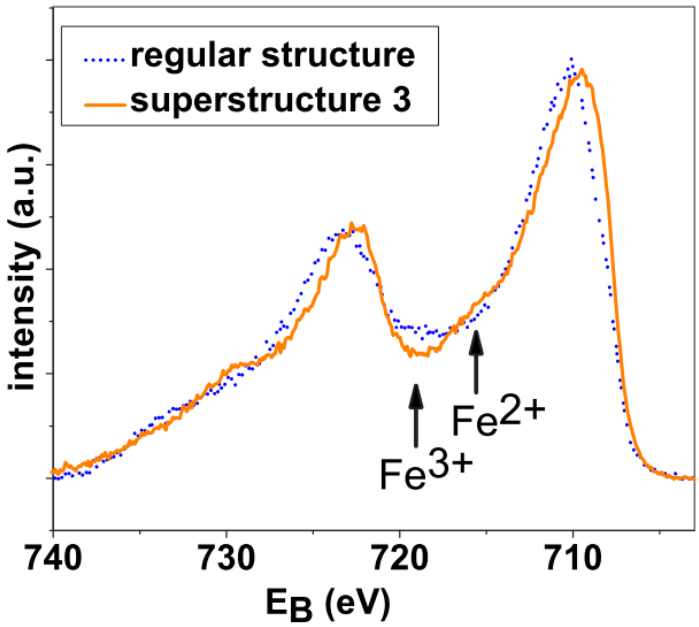

Figure 6.2: XPS measurements of the $Fe_{1-x}O$-like termination of $Fe_3O_4(111)$ taken from [101]. Superstructure 3 corresponds to the $Fe_{1-x}O$-like termination. The modification of the Fe 2p spectra, relative to the stoichiometric-like regular termination, is correlated to the $Fe_{1-x}O$-like nature of this termination.

of XPS measurements of the Fe_{oct} and bi-phase terminations, likely related to the difficultly to isolate these terminations, means relating the XPS measurements presented here to a particular {111} termination is not possible.

Turning to $Fe_3O_4(110)$. As was previously mentioned defects to the oxygen FFC lattice are unlikely. If the near-surface region is oxygen deficient - for example after sputtering which preferentially removes lighter oxygen atoms - annealing (UHV or oxygen environment) can lead to oxygen diffusion towards the surface region and the retention of the oxygen sublattice [132]. The bulk defect chemistry will not necessarily dictate the surface defect chemistry. DFT calculations predict that oxygen vacancies represent the most energetically stable surface vacancy for (110) terminated magnetite

[185]. The $Fe_3O_4(110)$ surface reconstruction discussed in chapter 7 is interpreted to contain surface oxygen vacancies. Furthermore, DFT calculations depicted in figure 7.7 illustrate that the oxygen surface vacancies give rise to an increased Fe^{2+} character. Therefore, {110} oxygen surface vacancies can contribute towards the increased Fe/O and Fe^{2+}/Fe^{3+} ratios.

In summary, the {111}-nanofaceted row reconstruction exhibits increased Fe^{2+}/Fe^{3+} and Fe/O ratios which are likely due to some combination of subsurface iron defects, {110} oxygen surface vacancies and a reduced {111} termination. Due to the greater coverage of {111} coverage relative to the {110} coverage, if the {111} termination is reduced, it will likely be the greatest contribution towards XPS spectra.

6.1.2 Scanning tunneling microscopy

STM images of the $Fe_3O_4(110)$ {111}-nanofaceted row reconstruction are depicted in figures 6.3 and 6.4. The reconstruction is characterised by rows, which run in the $[\bar{1}10]$ direction. The large scale STM image depicted in figure 6.3(a) demonstrates that the surface exhibits a terrace-like structure. Rows can run for hundreds of nanometers without breaking, as seen in figure 6.3(b), where a small percentage of the rows run the entire length of the 500 nm image.

Along the [001] direction the row frequently shift vertically up or down. The height difference is always observed to be a multiple of 3 Å (see the line profile in figure 6.4(c)), which corresponds to the difference between like-like (110) planes, i.e. A to A-plane or B to B-plane. The row periodicity along the [001] direction is equal to $\sim$25 Å (see the line profile in figure 6.4(c)). This periodicity corresponds to three times the unit cell parameter of 8.40 Å. The STM image in figure 6.4 also illustrates examples of missing rows, which are examined in detail in section 6.2.4.

The STM line profile displayed in figure 6.4(c), which is perpendicular to the row direction, shows deep (up to 3 Å) troughs between each row. This is very similar to that observed by Parkinson *et al.* [143], and is due to the

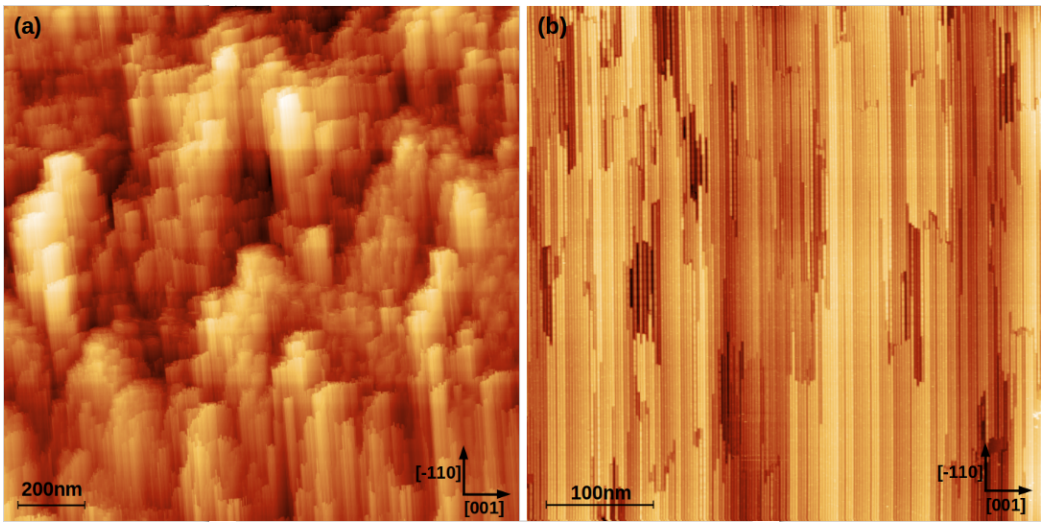

Figure 6.3: {111}-nanofaceted row reconstruction prepared by two 10 s UHV flash anneals at 900 °C. (a) 1.6 $\mu m \times 1.6\,\mu$m STM image which demonstrates the terrace-like structure. (b) 500 nm × 500 nm STM image in which rows run, in some cases, the entire length of the image.

presence of {111}-nanofacets which slope up and down relative to the rows ridges.

The reconstruction can be formed *in-situ* by annealing in UHV or oxygen atmospheres. The STM images in figures 6.3 and 6.4 correspond to a crystal which was prepared by two 10 s UHV flash anneals at 900 °C. Alternatively, the reconstruction has been prepared by annealing for 5 minutes at a temperature of 850 °C in an molecular oxygen partial pressure of 1×10^{-6} mbar. Figure 6.5 depicts the corresponding LEED and STM measurements. It is important to note that the crystals history is pivotal to the surface structure. For example, if the crystal is introduced to the chamber, outgassed and then immediately flashed, the {111}-nanofaceted row reconstruction will not be formed. There will be a tendency for rows in LEED and STM, but STM images show large corrugations and disordered areas. It is well known that a maghemite surface region forms in ambient conditions [166]. This oxide must be removed by annealing. In a UHV environment, at temperatures ranging from approximately 550 to 950 °C, magnetite is the stable iron ox-

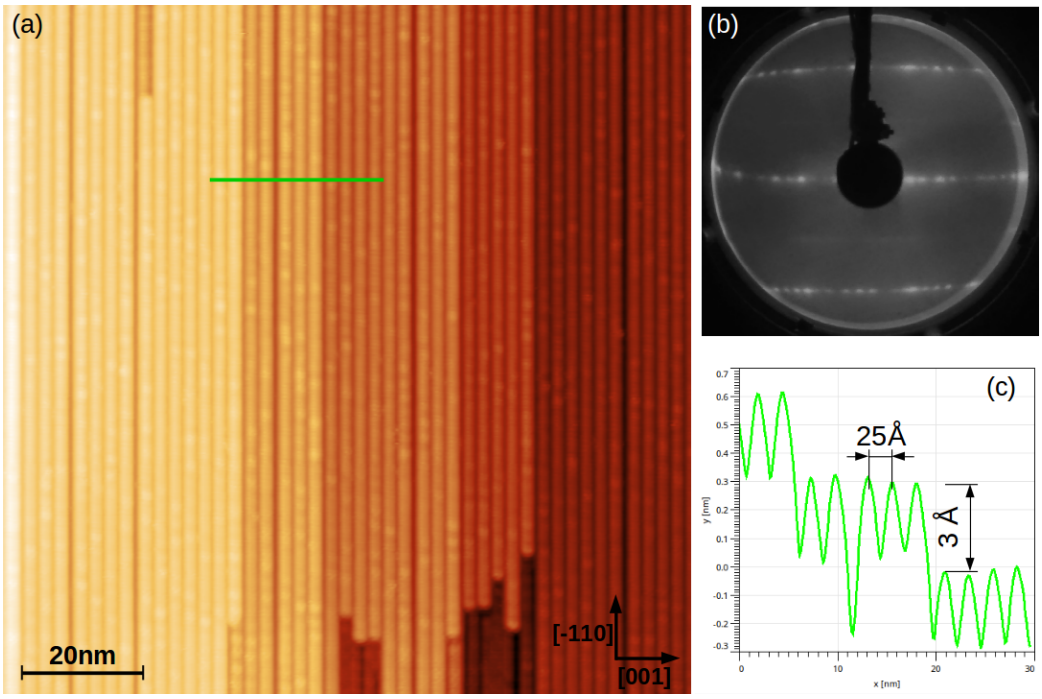

Figure 6.4: {111}-nanofaceted row reconstruction prepared by two 10 s UHV flash anneals at 900 °C. (a) 130 nm × 130 nm STM image (b) LEED image obtained at 80 eV (c) Line profile corresponding to the green line segment in the adjacent STM image. Rows are separated by ∼25 Å which corresponds to three times the unit cell parameter of 8.40 Å. Vertically, the rows ridges are separated by 3 Å, which corresponds to the difference between like-like (110) planes, i.e. A to A-plane or B to B-plane.

ide [52]. Hence, maghemite is removed by annealing in the aforementioned temperature range. High-temperature flash anneals alone will not convert the surface region to magnetite-like stoichiometry. Turning to the {111}-nanofaceted row reconstruction formed by the oxygen anneal, the crystal was UHV flashed annealed several times, and therefore likely heavily reduced (see figures 6.1 and 6.6), prior to the oxygen anneal. Evidently the faceted row reconstruction is stable at some stoichiometry or across some stoichiometry range and the formation of the reconstruction can be achieved by different preparation procedures, with the state of the surface prior to such procedures being pivotal.

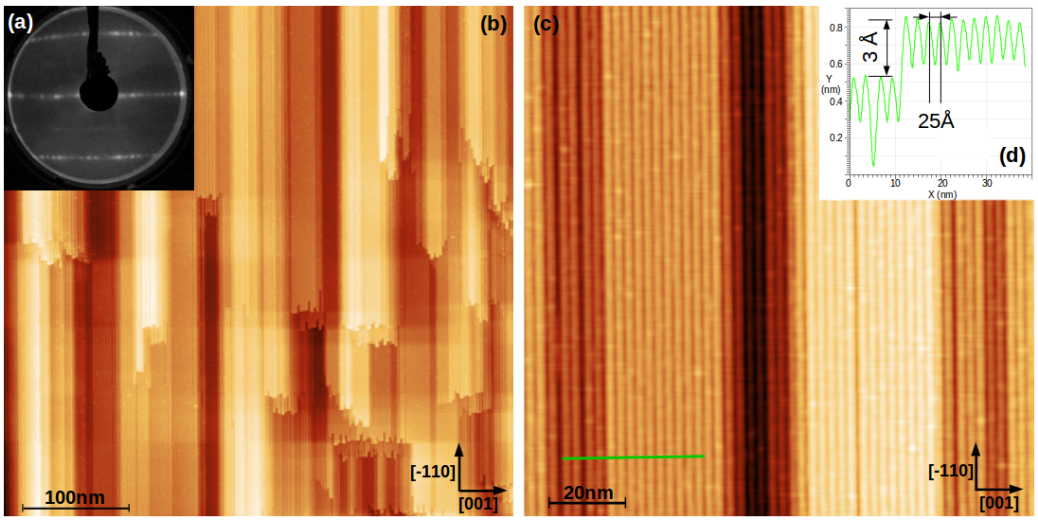

Figure 6.5: Row reconstruction prepared by annealing for 5 minutes at a temperature of 850 °C in an molecular oxygen partial pressure of 1×10^{-6} mbar. (a) LEED image obtained at an electron energy of 80 eV. (b) 500 nm × 500 nm STM image. (c) 130 nm × 130 nm STM image. (d) Line profile corresponding to the green line segment in (c), the ∼25 Å row periodicity and the deep trenches between rows are indicative of the {111}-nanofaceted row reconstruction.

Attention is now turned to the influence that slightly changing the preparation procedure has on the surface structure. This serves to highlight the sensitivity of the surface structure on the preparation procedure. Firstly the influence of multiple high temperature UHV flash anneals is discussed and secondly the influence of oxygen partial pressure is discussed.

While flash annealing in vacuum at 900 °C produces an ordered {111}-nanofaceted row reconstruction, additional flashes can change the surface structure. In figures 6.6(b) and (c) STM images are presented of the surface structure after a total of five 10 s UHV flashes at 900 °C. The large scale STM image (figure 6.6(b)) shows that the terrace size can be considerable larger (see figure 6.3(b) for comparison). Furthermore, figure 6.6(c) demonstrates that two row structures co-exist. The thicker rows correspond to the {111}-nanofaceted row reconstruction, this is determined by the left half of line profile in figure 6.6(d) which show deep trenches indicative of {111}-

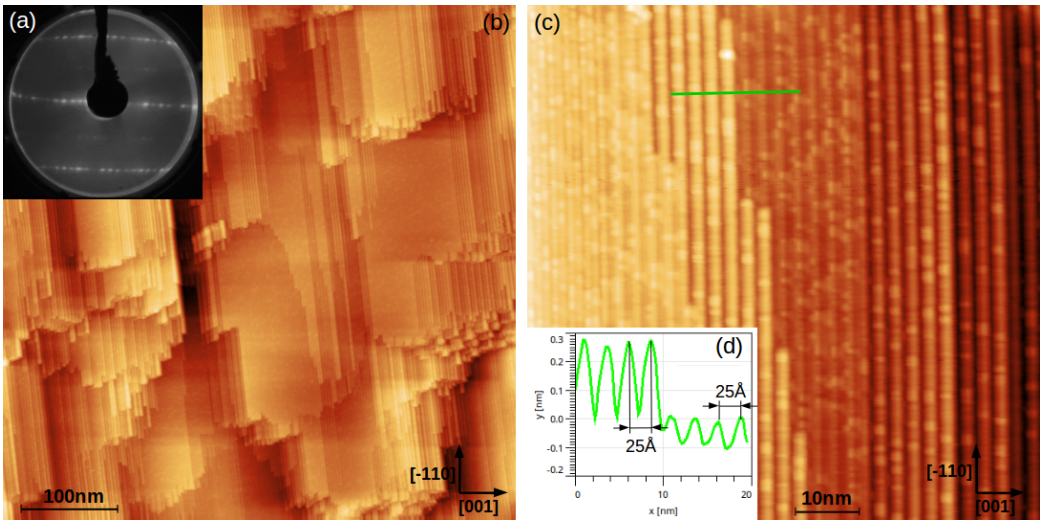

Figure 6.6: Row reconstruction prepared by five 10 s flash anneals at 900 °C. (a) LEED image obtained at an electron energy of 80 eV (b) 450 nm × 450 nm STM image. The terrace width, like that in the middle of the image, can be considerably large. (c) 75 nm × 75 nm STM image. Two row reconstructions co-exist. (d) Line profile corresponding the green line segment in (c). Both row structure have a periodicity of ∼25 Å. The left hand side of the line profile which exhibits deep trenches is indicative of the {111}-nanofaceted row reconstruction (see figure 6.4), while the right hand side exhibits a flatter structure not associated with nanofacets.

nanofacets. The rows of the second structure appear narrower in STM and the line profile (right half of figure 6.6(d)) indicates it is a far flatter structure and therefore not faceted. This structure has only been observed after multiple high temperature flash anneals. Upon scanning several areas, this different row reconstruction have been regularly observed.

Although multiple flashes gives rise to the coexistence of two row structures LEED images do not change compared to the surface which exhibits a single domain faceted row reconstruction (see figures 6.4(b) and 6.6(a) for comparison). Each of the row structures in figure 6.6(c) exhibits a 25 Å periodicity, and hence, LEED reflects the row periodicity but does not distinguish between different (1×3) row structures.

The different row structures can be understood by considering XPS measurements in figure 6.1: annealing in UHV at 800 °C produces the {111}-nanofaceted row reconstruction which is reduced (Fe/O = 0.79). Multiple UHV flashes at 900 °C which are detrimental to the surface structure likely produce a highly reduced surface which may exhibit $Fe_{1-x}O$ - like stoichiometry. STS measurements could provide further evidence of the inequivalence of these two row structures and the possibility of a $Fe_{1-x}O$ - like structure.

The influence of the molecular oxygen partial pressure on the surface structure has been examined. Figure 6.7 displays STM images of the surface prepared by annealing for 5 minutes at a temperature of 850 °C in an molecular oxygen partial pressure of 5×10^{-6} mbar. LEED images (figure 6.7(a)) are indicative of a row reconstruction. However, defined spots which indicate the row periodicity are not present. The preparation procedure and more importantly the LEED images are similar to that of the XPS mea-

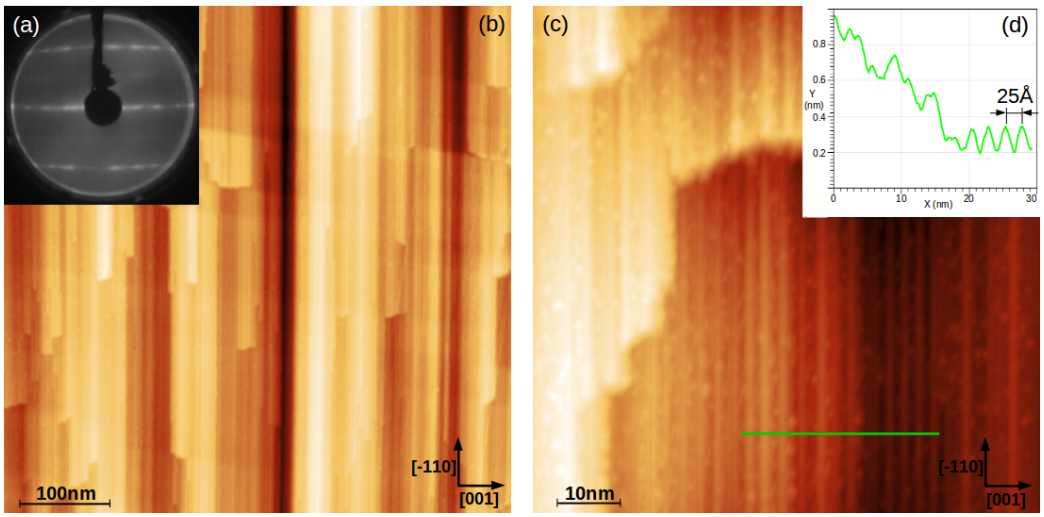

Figure 6.7: Row reconstruction prepared by annealing for 5 minutes at a temperature of 850 °C in an molecular oxygen partial pressure of 5×10^{-6} mbar. (a) LEED image obtained at an electron energy of 80 eV. (b) 470 nm × 470 nm STM image. (c) 95 nm × 95 nm STM image. (d) Line profile corresponding to the green line in (c), the right half with a row periodicity of ∼ 25 Å and deep trenches between rows is indicative of the {111}-nanofaceted (1 × 3) row reconstruction. However, the left half exhibits no periodicity.

surements (3×10^{-6} mbar, 800 °C) which produced a stoichiometric surface region. Therefore, the surface region depicted in figure 6.7 is likely close to stoichiometric magnetite. STM measurements show a row reconstructed surface, however the structure differs from the {111}-nanofaceted row reconstruction depicted in figures 6.3 and 6.5, for example. This is best demonstrated by the line profile in figure 6.7(d). The right half of the line profile exhibits the routinely observed periodicity of ~ 25 Å, however the left half displays no periodicity. Clearly this observation, along with the increased roughness of the surface, will contribute to reduced order observed by LEED. Portions of this surface may exhibit the {111}-nanofaceted row reconstruction. However, the reconstruction does not appear to be dominant.

The preparation procedures which results in the reduced and stoichiometric surface structure seen in figures 6.5 and 6.7 only differ in oxygen partial pressure. However, the partial pressure will not necessarily be the only factor: the stoichiometry and correlated surface structure will likely depend on the oxygen anneal temperature, time and partial pressure as well as the samples history.

6.1.3 Scanning tunneling spectroscopy

STS measurements have been performed in order to determine the {111}-nanofaceted row reconstruction electronic properties. The tip is held at a constant height which is determined by the chosen CCM scanning parameters (tunneling current and bias current). The bias voltage is swept across some range and the tunneling current as a function of the bias is recorded. At each individual point the spectra is averaged over 10-15 individual current-voltage (I(V)) curves and the measurements have been performed on a grid. Analysing the I(V) characteristics across many points removes the possibility of assigning electronic properties associated with absorbents or point defects to those of the reconstruction. At each I(V) measurement point, a constant current topography value is obtained. Therefore, a constant current STM image with the same resolution as the spectroscopy grid is acquired in-parallel.

Grid spectroscopy measurements on two surfaces have been performed: the UHV annealed crystal which was prepared by two 10 s flash anneals at 900 °C and the oxygen annealed crystal which was prepared at 850 °C for 5 minutes in a molecular oxygen partial pressure of 1×10^{-6} mbar. Each of these surfaces exhibit the {111}-nanofaceted row reconstruction. In fact, STM and LEED do not reveal any differences between the two surface structures. Figure 6.8 depicts the two grid spectroscopy measurements. The associated STM images of the reconstruction prepared in UHV (figure 6.8(a)) and oxygen (figure 6.8(b)) are indicative of the {111}-nanofaceted row reconstruction. In both cases the tip height prior to sweeping the voltage was 1.6 V and 50 pA. Large bias voltages and low tunneling currents increase the tip-surface distance. As a result the tunneling current does not reach high values at the boundaries of the bias sweep and therefore the likelihood of damaging or changing the tip structure is reduced. Figure 6.8(c) and (d) depict the I(V)-curves and dI(V)/dV curves of the {111}-nanofaceted row reconstruction prepared in oxygen (—) and UHV (—) environments. The numerical derivative of the I(V)-curves gives the dI(V)/dV curves. The ridge and trough segments of the row reconstruction exhibit different I(V) characteristics and this is detailed in depth in section 6.2.2. Therefore, the spectra are averaged over 100 individual points on the ridge of the reconstruction. There is a clear inequivalence between the reconstruction prepared in UHV and oxygen environments with the UHV and oxygen annealed prepared reconstructions exhibiting semiconducting gaps of $\sim$1.00 eV and $\sim$1.50 eV, respectively.

Fe_3O_4 semiconducting surfaces are reported throughout the literature [109, 138, 141]. Novotny *et al.* performed DFT calculations of Fe_3O_4(001) terminations with increasing Fe/O surfaces ratios. The Fe/O ratios ranged from stoichiometric (bulk-truncated plane) to FeO - like. Each of the terminating layers were semiconducting. However, the sub-surface layers were conducting. The Fe-dimer termination of Fe_3O_4(001) is predicted by DFT calculations to be semiconducting and display an increased Fe^{2+}/Fe^{3+} surface ratio and XPS measurements reveal increased Fe/O and Fe^{2+}/Fe^{3+} ratios [109]. The {111}-nanofaceted row reconstruction examined in this work dis-

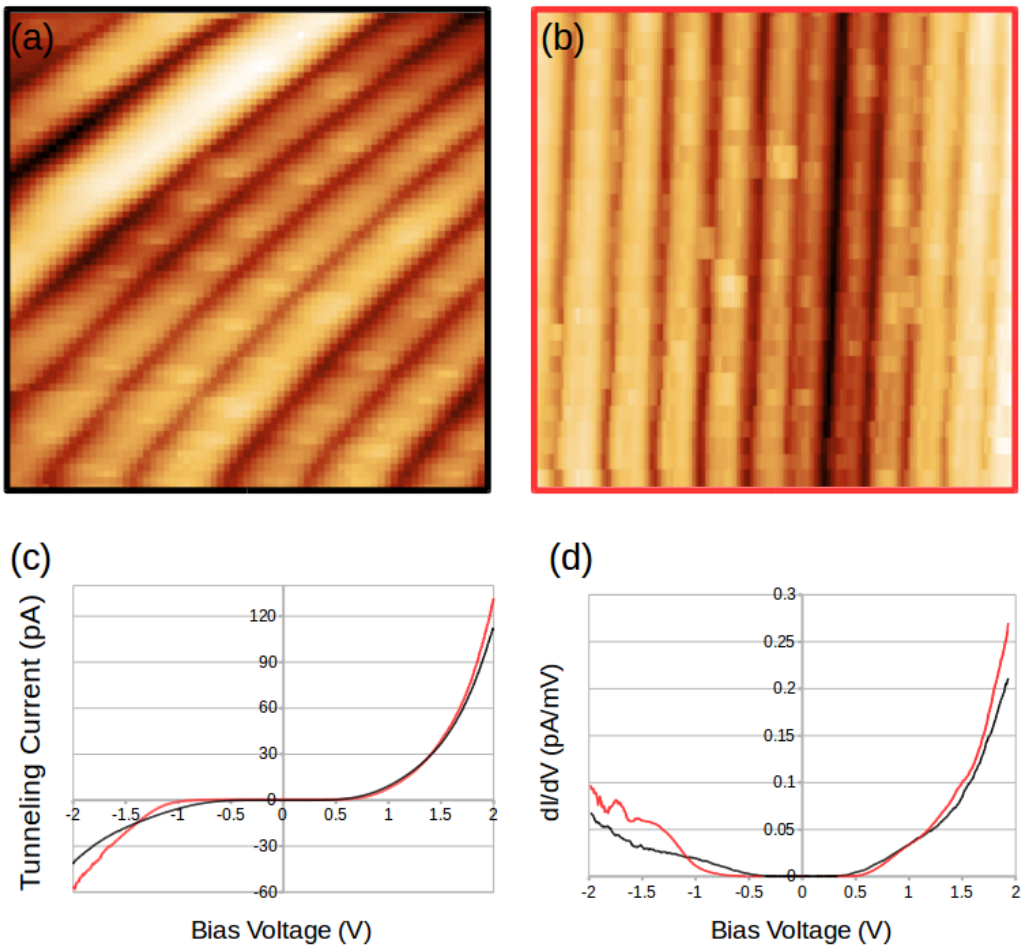

Figure 6.8: Grid spectroscopy measurements of the {111}-nanofaceted row reconstruction prepared in UHV (—) and oxygen (—) environments. (a) & (b) STM images obtained in-parallel as the grid spectroscopy measurement is on-going. (c) and (d) I(V)-curves and dI(V)/dV curves of the {111}-nanofaceted row reconstruction prepared in oxygen (—) and UHV (—) environments. The spectra are averaged over 100 individual points on the ridge of the reconstruction. There is a clear inequivalence between the reconstruction prepared in UHV and oxygen environments.

plays similarities: increased Fe/O and Fe^{2+}/Fe^{3+} ratios and a semiconducting surface.

XPS measurements depicted in figure 6.1 illustrate that the Fe/O ratio can significantly vary when annealing in UHV or oxygen atmospheres. The

{111}-nanofaceted row reconstruction prepared in different atmospheres are suggested to have different Fe/O ratios which results in different electronic properties.

6.1.4 Reflectance anisotropy spectroscopy

RAS measurements have been performed on the {111}-nanofaceted row reconstruction prepared in UHV and oxygen atmospheres. These measurements were performed on a larger single crystal. The surface preparation was identical to that which produced the surface structure seen in figures 6.4 and 6.5. As mentioned earlier the history of the sample will play an important role in the surface structure and stoichiometry. However, this section serves to highlight that RAS is sensitive to the different surface stoichiometry that can be induced by preparation procedure and history. Figure 6.9 depicts the RAS spectra of the two surfaces. Inset are the LEED images of each surface. Clearly the UHV flashed annealed crystal exhibits a better degree of order. Nevertheless, the LEED images display similar features which are associated with the {111}-nanofaceted row reconstruction. The two spectra are very similar, both exhibit a derivative-like feature below 2.1 eV and a broad feature at higher energies. The magnitude of these features is larger for the oxygen annealed crystal. The comparison of the two spectra is best visualised by the difference spectra (blue dashed line in figure 6.9) which is offset for clarity. The difference spectra is extremely similar to its components and this indicates that the mechanism at play which gives rise to this RAS signal is the same for the UHV and oxygen annealed surfaces.

In section 5.1.3, the origin of the presented RAS signal is examined in detail: the anisotropic optical response at low energies originates from small anisotropic shifts in energy of the optical transitions associated with anisotropic strain in the surface region. It is suggested that the different magnitudes of the minima/maxima feature below 2 eV of the oxygen and UHV annealed {111}-nanofaceted row reconstruction is related to different degree of strain in the terminating layers.

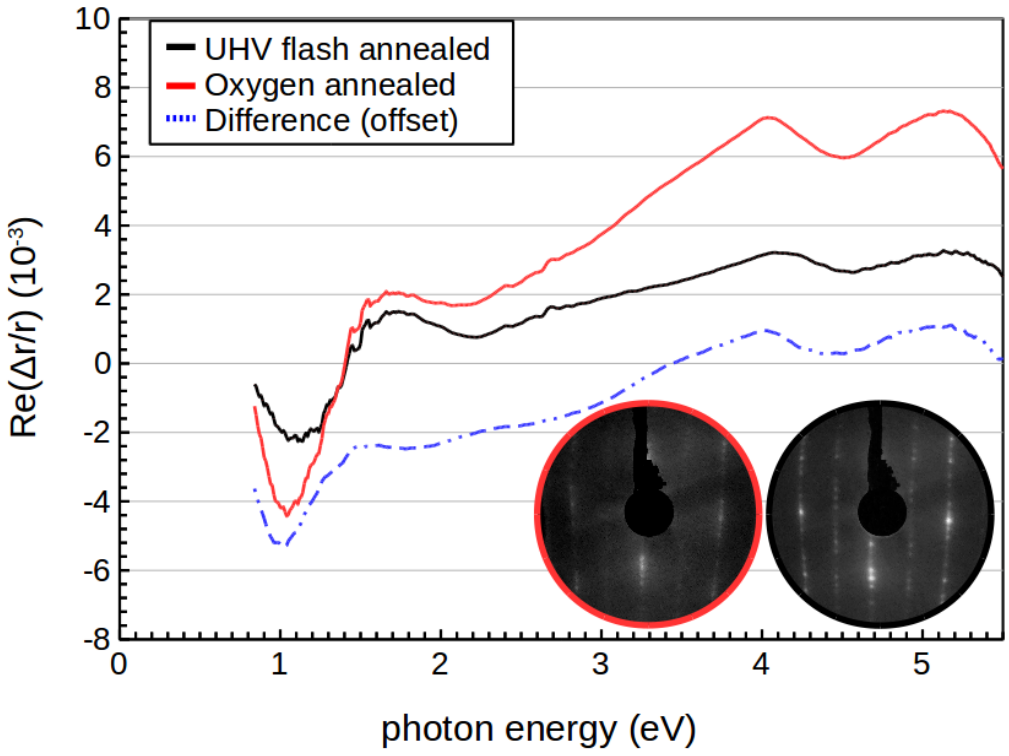

Figure 6.9: RAS spectra of a UHV flash annealed and oxygen annealed crystal. Inset are LEED images of each surface at an electron energy of 100 eV. Clearly the oxygen annealed crystal does not have an excellent degree of order. Nevertheless, both LEED images are indicative of the {111}-nanofaceted row reconstruction. The difference spectra, which is offset for clarity, is very similar to its components indicating the mechanism which generates the optical anisotropy for each surface is the same. However, the difference in magnitude of the prominent features highlights that the two structures are non-equivalent, likely related to different stoichiometry.

As is the case with the STS measurements, the non-equivalence of the RAS spectra is interpreted to be a result of differing stoichiometry in the surface region indicated by XPS measurements. Altering the surface regions stoichiometry can in turn alter the strain in the surface region and the associated RAS signal.

6.2 Atomic and electronic structure

Recently, the (1×3) row reconstruction of (110) terminated magnetite has been concluded to consist of periodic nanofacets which expose {111}-type planes [143]. However, the atomic and electronic structure remains an open question. In this section high-resolution STM images are presented, and the atomic structure of the reconstruction is discussed. Furthermore, STS measurements revealing 1D states and irregularities in the form of contaminants, missing rows and atomic steps are discussed.

6.2.1 High resolution scanning tunneling microscopy images

Figure 6.10 displays high-resolution STM images of the {111}-nanofaceted row reconstruction. The images corresponds to the surface which was prepared by two 10 s UHV flash anneals at 900 °C.

High-resolution STM images of (110) terminated magnetite are scarce in the literature. Parkinson commented on the difficulty in obtaining atomic resolution of the {111}-nanofaceted row reconstruction [143]. The difficulty is likely related to the geometry of the reconstruction. It is well known that scanning across the ridge of a row-like structure can give rise to an unstable tip. Indeed, this was the case during STM experiments. Consequently, the fast scan direction was always set perpendicular to the direction in which the rows' ridges run, corresponding to the [001] direction as seen in figure 6.10(a). As a result, the tip is constantly moving up and down to follow the corrugated nature of the reconstruction. This corrugation, which is 3 - 4 Å (compared to the atomic corrugation on the ridges of $\sim$ 30 pm) adds an additional level of difficulty to obtaining atomic resolution on the ridges. It is noted that obtaining atomic resolution on the atomically flat Fe_3O_4(110) surface structure presented in section 7, whose atomic features exhibit a similar corrugation, was a considerably easier task.

Figure 6.10(c) displays a zoom of a ridge of the {111}-nanofaceted row reconstruction. Due to the small height of the atomic features relative to the

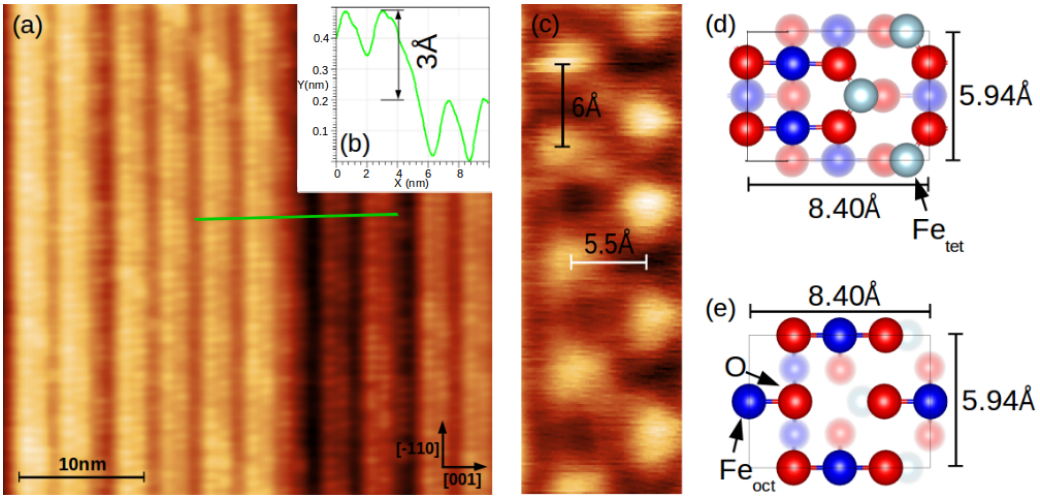

Figure 6.10: (a) $(30 \times 30)\,\mathrm{nm}^2$ STM image of the {111}-nanofaceted row reconstruction, $V = 1.20\,\mathrm{V}$ and $I = 58\,\mathrm{pA}$. (b) Line profile corresponding to the green line segment in (a). (c) Zoom of the ridge, $V = 1.20\,\mathrm{V}$ and $I = 13\,\mathrm{pA}$. (d) and (e) depict the A- and B-planes of (110) terminated magnetite. Assigning the features in STM images as iron atoms, the rows' ridges are tentatively suggested to be B-plane terminated.

row corrugation, the best way to visualise the atomic features is via a zoom of a ridge. The ridge is characterised by two rows which are separated by 5.5 Å along the [001] direction. Along the $[\bar{1}10]$ direction features are also often separated by 6 Å. However, sometimes the separation is larger, or smaller, by ∼1 Å. 6 Å corresponds to the surface unit cell parameter along the $[\bar{1}10]$ direction. The features in each row are shifted relative to each other by 3 Å in the $[\bar{1}10]$ direction. Furthermore, one of the rows is observed to be brighter than the other.

Features in CCM STM images of magnetite surfaces are assigned to iron atoms. The Fe_{oct} 3d level sits at the Fermi level [61, 64] and the oxygen 2p level sits several eV below the Fermi level [61]. Features in simulated (Tersoff-Hamann scheme) STM images, included those in this work (see figure 7.6), are positioned above iron atoms [99]. In agreement with [143], the vertical distance between ridges when steps are present is always a multiple of 3 Å (figure 6.10(b)), which corresponds to the distance between like (110) planes,

e.g. A- to A-plane or B- to B-plane. Therefore, the (110) termination is either an A- or B-plane terminated, not a mixture of both.

The question arises as to which (110) plane terminates this reconstruction, and furthermore, is the terminating plane bulk-truncated or otherwise. Figure 6.10(d) and (e) depict the A- and B-planes of (110) terminated magnetite. Considering the iron atoms, the features of the ridge show a greater comparison to the B-plane. The only difference being that the Fe_{oct} atoms of the B-plane are separated by 4.2 Å along the [001] direction, as opposed to 5.5 Å separation in STM images.

The features of the ridge show striking similarities to the reconstruction presented in section 7 which is determined to be B-plane terminated and contains oxygen surface vacancies. For comparison please see figures 7.2 and 6.10(c). Another similarity is that XPS and DFT predict increased Fe/O and Fe^{2+}/Fe^{3+} ratios for the reconstruction presented here and in section 7, respectively.

Drawing conclusions about surface reconstruction based on STM images alone is unpractical. The analysis provided here indicates that a B-plane termination is more likely than an A-plane termination. Although reconstructions are expected due to the polar nature of $Fe_3O_4(110)$. DFT calculations and the subsequent simulation of both STM images and RAS spectra are planned. These calculations combined with experimental STM, RAS and XPS measurements can provide quantitative insight into the atomic structure of the {111}-nanofaceted row reconstruction. LEED-IV measurements, and their comparison to theoretically calculated curves for different models, can also provide quantitative insight into the atomic structure of this reconstruction.

6.2.2 One-dimensional electronic states

STS measurements in section 6.1.3 demonstrate that the surface is semiconducting. Here, I(V) measurements indicate that the electronic properties of the {111}-nanofaceted row reconstruction differ across the unit cell of the reconstruction. The I(V)-curves depicted in figure 6.11(c) and the numeri-

cally differentiated I(V)-curves in figure 6.11(d) were obtained at the ridge and trough of the row structure.

The nonequivalence of the ridge and trough of the row reconstruction is best visualised by I(V)-line spectroscopy measurements. 50 individual I(V) measurements have been performed along a line segment. At each point the spectra is average over 15 individual I(V)-curves. As the tip is moved across the line, the tip height is stabilised by the CCM scanning parameters. The voltage has been swept between + 2 V and - 2 V. The spectroscopy line corresponds to the black line segment in figure 6.11(a). Below this STM image, figure 6.11(b) depicts the tunneling current value at each spectroscopy point on the line at a sweep voltage value of 1 V. Brighter corresponds to a higher tunneling current value.

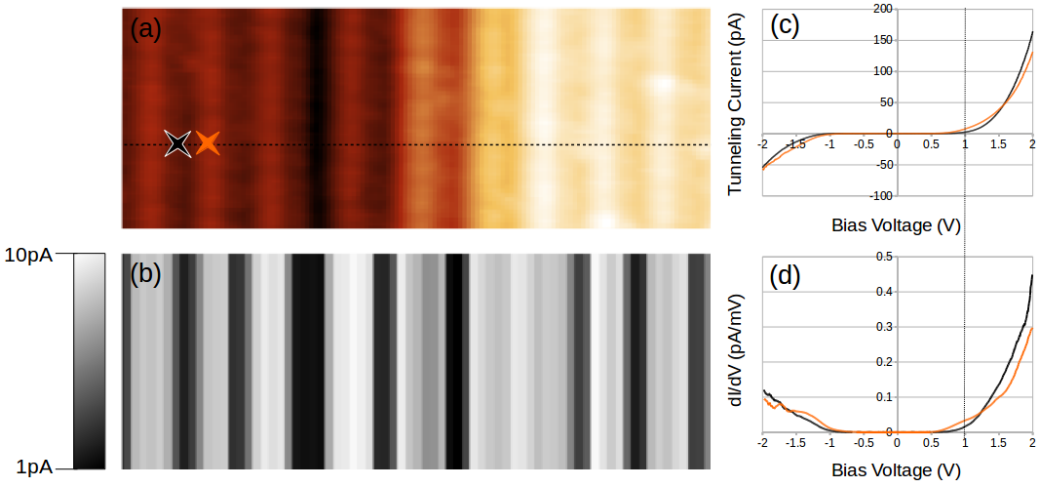

Figure 6.11: (a) STM image of the {111}-nanofaceted row reconstruction. The black and orange I(V)- and dI(V)/dV-curves in (c) and (d) correspond to the black and oranges crosses in (a). I(V)-line spectroscopy measurements have been performed along the black line segment in (a). (b) illustrates the tunneling current value at a sweep bias value of + 1 V (marked by the vertical dashed black line in (c)) for each I(V)-curve. (a) and (b) are aligned, that is to say, the current value in (b) corresponds to the I(V)-curve at the position directly above it on the black line in (a). Evidently, the electronic structure of the ridge and trough are non-equivalent.

Comparing figures 6.11(a) and 6.11(b), it is clear that the ridge and trough segments of the row reconstruction are electronically inequivalent. This is understood in terms of the RAS study of this reconstruction presented in section 5.1.3: the anisotropic optical response is interpreted to result from the modification of bulk-like states induced by a strained surface region. Furthermore, DFT calculations demonstrate that the ridge and trough of the reconstruction exhibits compressive and tensile strain, respectively (see figure 5.6). Such strain can render these sections of the unit cell non-equivalent, as is observed in STS measurements, and therefore give rise to 1D states.

An additionally mechanism which may contribute towards the electronic inequivalence is the presence of the {111}-nanofacets. When the trough is probed the nanofacets simultaneously probed due to the finite width of the STM tip. The {111}-nanofacets could very well differ electronically from the {110}-ridges. Nevertheless these measurements demonstrate the existence 1D electronic states and demonstrate that this reconstruction may provide a useful template for the growth of 1D nanostructures.

6.2.3 Contaminants and atomic structure defects

Along the ridges cluster-like features are frequently observed. Several can be seen in figure 6.12(a). These clusters, which are imaged as protrusions in STM, are several nanometers in diameter. They are imaged as one entity with no internal structure and are observed whether this reconstruction is prepared in oxygen or UHV environments. Figure 6.12(a) provides a good example of their frequency of occurrence. For single crystal magnetite, contaminants in the form of magnesium, potassium and calcium are regularly reported [113, 138, 186]. Furthermore, hydrogen and carbon regularly contribute to contaminants in UHV surface science. XPS measurements of the {111}-nanofaceted row reconstruction do not detect any observable trace of the aforementioned elements. Therefore, it is suggested that these clusters are formed from iron or iron oxide. XPS measurements did not provide any evidence towards the presence of such contaminants.

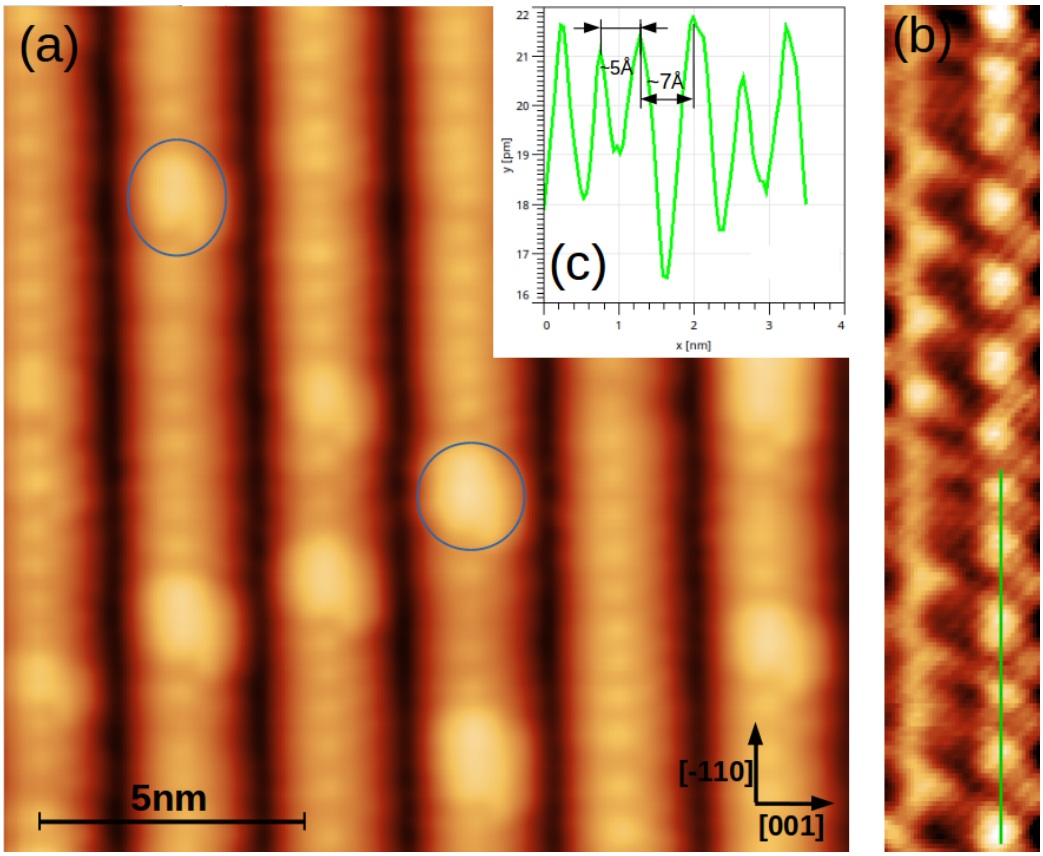

Figure 6.12: (a) $(13 \times 13)\,\mathrm{nm}^2$ STM image. The blue ovals highlight examples of the occurrence of cluster-like features which are routinely observed on the ridges of the reconstruction. (b) $(13 \times 86)\,\mathrm{Å}^2$ high resolution STM image of the ridge of the {111}-nanofaceted row reconstruction, $V = 1.20\,\mathrm{V}$ and $I = 16\,\mathrm{pA}$. It can be seen that the distance between features along the $[\bar{1}10]$ direction is not absolutely constant. This is emphasised by the line profile in (c), which corresponds to the green line segment in (b).

Figure 6.12(b) depicts a high-resolution STM image of the ridge of the {111}-nanofaceted row reconstruction. The atomic structure of the ridge is somewhat weakly ordered, in the sense that the atomic separation along the $[\bar{1}10]$ direction is not constant. This is illustrated by the line profile (figure 6.12(c)) where the distance between features varies from 5 to 7 Å.

6.2.4 Missing rows and atomic steps

Irregularities in the form of missing rows and atomic steps are frequently observed. Each of these break the ∼25 Å periodicity. However, the geometry of these features is not random. Examples of missing rows and atomic steps are depicted in figures 6.13 and 6.15. In this section it is demonstrated that the geometry of these irregularities can be understood by considering that the {111}-nanofacet coverage, at the atomic steps or missing rows, is maximised.

In the presence of missing rows ridge-to-ridge separations of ∼34 Å, ∼42 Å and ∼50 Å have been observed. These distances correspond to 4, 5 and 6 times the (110) unit cell parameter of 8.4 Å, respectively. When these features are present the separation of the rows is always observed to be an integer multiple of 8.4 Å. The vertical ridge-to-trough depth increases with

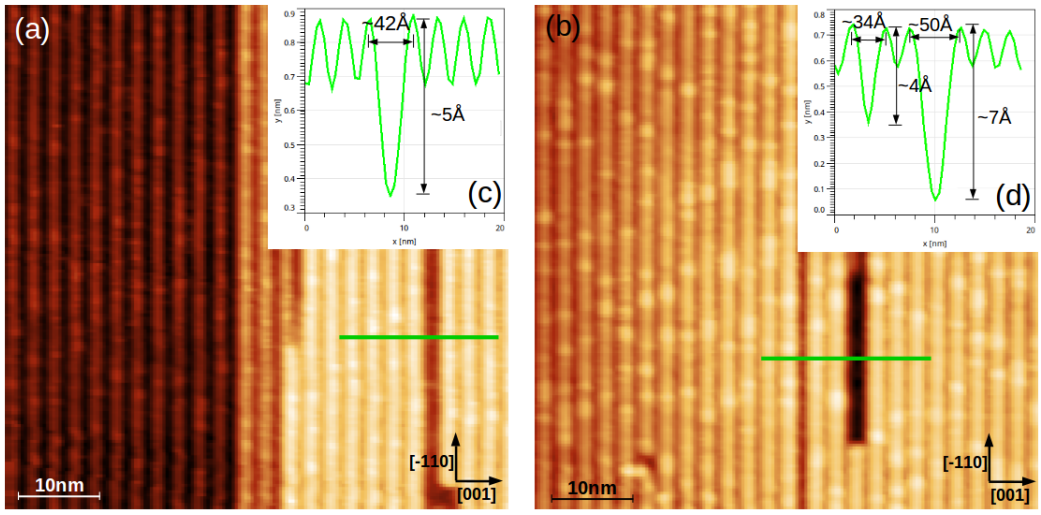

Figure 6.13: (a) and (b): 60 nm× 60 nm STM images. (c) and (d): line profiles corresponding to green line segment in (a) and (b). In the presence of missing rows the ridges can be separated by ∼34, ∼42 and ∼50 Å which corresponds to 4, 5 and 6 times the unit cell parameter of 8.4 Å. With the increasing ridge-to-ridge distance the ridge-to-trough depth increases. The reason for such relationships, which maximises the (111) coverage, can be understood by viewing figure 6.14.

the row separation as seen in figure 6.13(d). It is important to note that as the tip probes the trough it will collect current from other segments of the reconstruction due to its finite size and this results in an underestimated ridge-to-trough depth.

The geometry of the missing rows can be understood by examining the structure of this reconstruction. If one starts with the ansatz that the {110} and {111} sections of the reconstruction are always terminated by the same (110) and (111) planes and the (111) surface coverage is maximised, then is follows that the distance between rows must be a multiple of 8.4 Å. This is illustrated schematically in figure 6.14 which demonstrates examples of

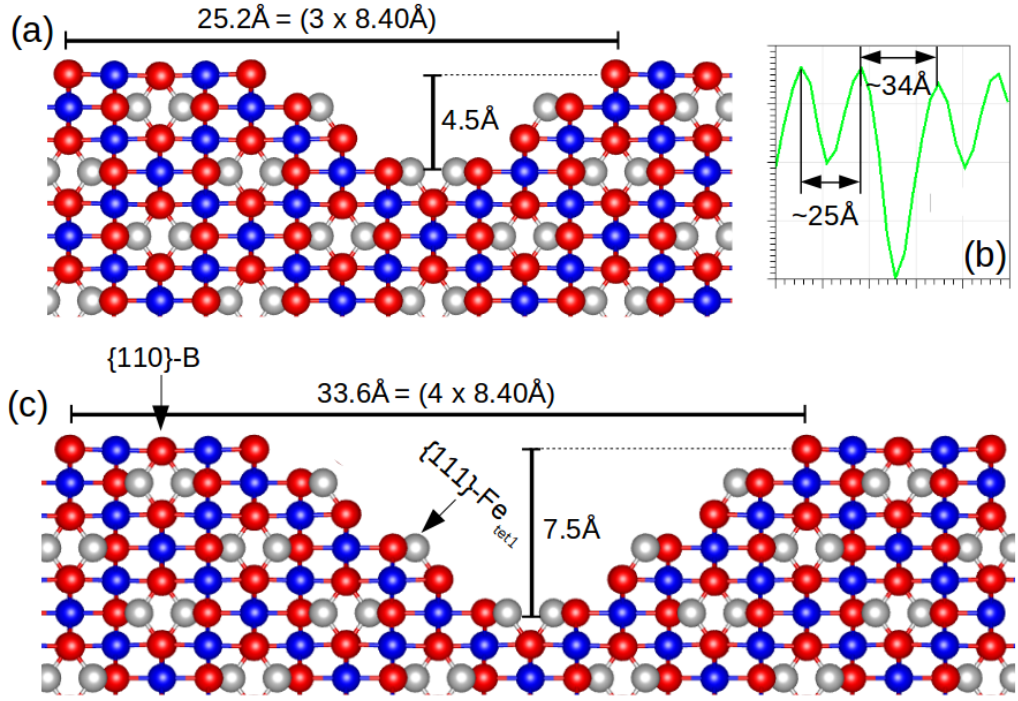

Figure 6.14: The ridge-to-ridge distance in (a) and (c) are 25.2 Å and 33.6 Å and the corresponding ridge-to-trough depths are 4.5 Å and 7.5 Å, respectively. Experimentally, when the regular 25 Å periodicity is broken by missing rows, the ridge-to-ridge distance is always an integer multiple (greater than 3) times 8.4 Å. The STM line profile in (b) illustrates a ridge-to-ridge distance of $\sim$34 Å. Note that the ridge-to-trough depth increases with the ridge-to-ridge separation.

25.2 Å ($3 \times 8.4 = 25$ Å) and 33.6 Å ($4 \times 8.4 = 25$ Å) ridge-to-ridge separations. The model in figure 6.14 is a stoichiometric slab terminated by {111} Fe_{tet_1}- and {110} B-planes. Figure 6.14 also demonstrates that with increasing row separation the facets between them increase in size, and hence, the ridge-to-trough depth increases, in agreement with the experimental observations. If the distance between rows is a non-integer times 8.4 Å, either the two facets will not be the same (111) termination or the {110} segments will be larger or of a different (110) termination.

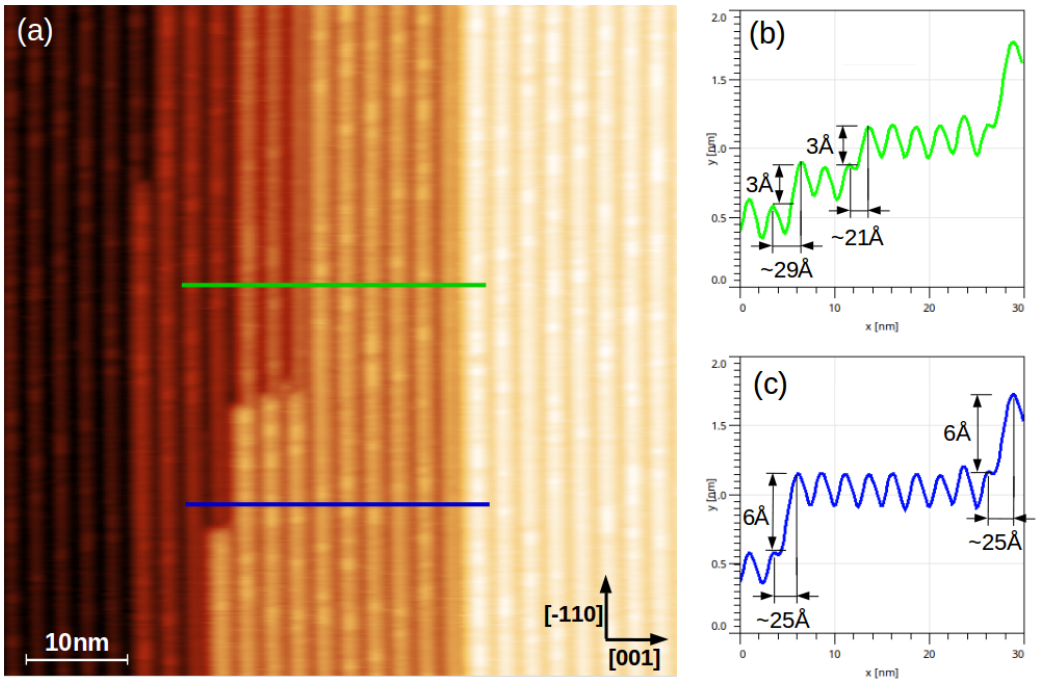

Figure 6.15: (a) 80 nm × 80 nm STM. (b) Line profile corresponding to the green line segment in (a). When the rows step up by 3 Å the lateral separation of the rows is observed to be equal to 21 Å or 29 Å, these distance correspond to $2\frac{1}{2}$ and $3\frac{1}{2}$ times the unit cell parameter of 8.4 Å, respectively. (c) Line profile corresponding to the blue line segment in (a). When the rows step up by 6 Å the lateral separation of the rows is observed to be equal to 25 Å which corresponds to 3 times the unit cell parameter of 8.4 Å. The reason for such relationships, which maximising the (111) coverage, can be understood by viewing figure 6.16.

This analysis can also be applied to the atomic steps. The rows are routinely observed to step up of down by 3 or 6 Å as seen in figure 6.15. 3 Å corresponds to the distance between like (110) planes, A to A-plane or B to B-plane. If we enforce the conclusion drawn from the missing rows, that is, the (111) coverage is maximised, we find that the ridge-to-ridge distance must be an integer and a half times 8.4 Å when their vertical separation is

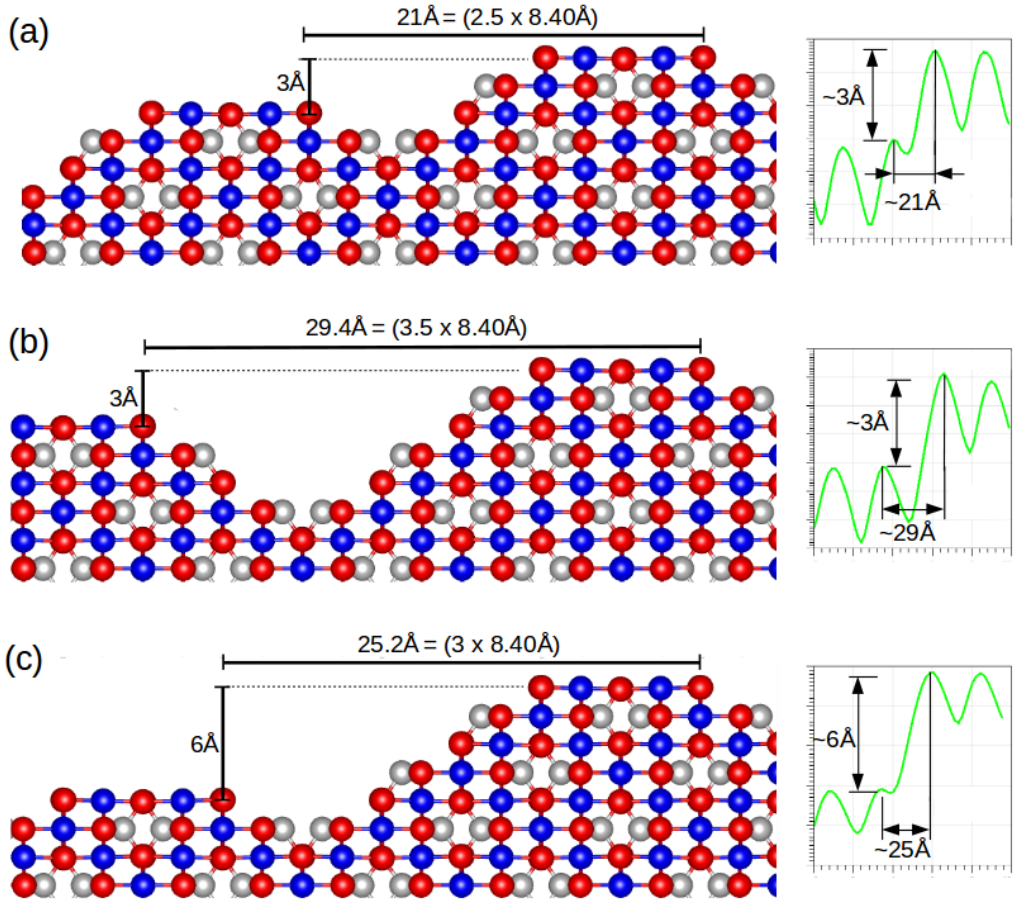

Figure 6.16: (a) and (b) illustrate that if the step height is equal to 3 Å, the lateral distance between ridges is an integer and a half times the unit cell distance. (c) illustrates that if the step height is equal to 6 Å, the lateral distance between ridges is an integer times the unit cell distance. The models are compared to the experimental STM line profiles. Note the comparison between the models and line profiles ridge-to-trough depth between the step.

3 Å. Furthermore, if the vertical separation is 6 Å the ridge-to-ridge distance must be an integer times 8.4 Å. This is depicted schematically in figure 6.16 and is always observed experimentally.

At irregularities in the form of missing rows and atomic steps, the {111}-facets are present and are maximised. The analysis is in agreement and adds weight to the work of Parkinson *et al.*, who determined on the basis of RHEED that faceting occurred [143]. The question arises as to why the reconstruction is (1×3) and not (1×4) or greater, as a larger unit cell will increase the {111} coverage. In section 5.1.3, on the basis of RAS measurements and DFT calculations, it is concluded the terminating layers of the {111}-nanofaceted row reconstruction are stained. Increasing the periodic unit increases the facet size, and hence, the facet height (surface normal direction). With increased facet height the strain in the terminating planes will be greater: the strain in any layer is constrained by the strain in the layer below it, hence, will greater facet height the strain in the terminating plane will increase. It is suggested that the reduction in surface energy associated with increasing {111} coverage, is at odds with the resultant strain energy. (1×3) periodicity is likely a balance between the two.

6.3 Discussion, conclusions & outlook

STM and LEED measurements indicate the conditions required for the preparation of the {111}-nanofaceted row reconstruction. The reconstruction can be formed in UHV by flash annealing at 900 °C, or by annealing in a molecular oxygen partial pressure of 1×10^{-6} mbar at ∼850 °C. The reconstruction is very sensitive to the molecular oxygen partial pressure: increasing the pressure produces a row reconstructed surface which appears different in LEED and STM, is rougher and likely does not contain {111}-nanofacetes. While flashing the crystal at 900 °C produces the {111}-nanofaceted row reconstruction with the best degree of order, additional flashes are detrimental to the reconstruction: areas appear which exhibit row reconstruction which is not faceted. This can be understood from XPS measurements: the UHV annealed (800 °C) crystal exhibits an increased Fe/O ratio, while the oxygen

annealed crystal (3×10^{-6} mbar , 800 °C) is stoichiometric. Multiple flashes at 900 °C will produce a highly reduced surface region which may exhibit $Fe_{1-x}O$ - like stoichiometry.

RAS and STS measurements indicate that the {111}-nanofaceted row reconstruction prepared in different environments are intrinsically different structures. STS measurements reveal semiconducting gaps of around 1.5 eV and 1.0 eV for row reconstructions prepared by oxygen annealing and UHV flash annealing, respectively. Furthermore, RAS measurements reveal similar but different spectra. These measurements indicate that the reconstructions' electronic structure can be altered by the preparation procedure and the structural changes are located at or close to the surface. XPS measurements can shed light on these observations; considering that annealing in oxygen and UHV changes the Fe/O and Fe^{2+}/Fe^{3+} ratios, it is concluded that the {111}-nanofacets are stable across some stoichiometry range and the different stoichiometry alters the correlated electronic properties.

While the reconstruction is stable across some stoichiometry range, it is evident that it is reduced. LEED images obtained during XPS measurements of the UHV annealed surface, which exhibits increased Fe/O and Fe^{2+}/Fe^{3+} ratios, are indicative of the {111}-nanofaceted row reconstruction. Oxygen sub-surface vacancies and terminations composed entirely of iron are unexpected. The increased Fe^{2+} content observed in XPS is consistent with a reduced (decreased O/Fe ratio relative to bulk truncated) termination, which are common throughout the literature. Such an Fe^{2+} enrichment is consistent with {110} oxygen surface vacancies and/or a reduced {111} termination. Sub-surface iron interstitials, which are the common defect in reducing conditions, do not produce similar XPS features. However, they cannot be ruled out. Due to the greater coverage of {111} coverage relative to the {110} coverage, if the {111} termination is reduced, it will likely be the greatest contribution towards XPS spectra.

High-resolution STM images provide insight into the reconstruction's atomic-structure. It is tentatively suggested that the {111}-nanofaceted row reconstruction is B-plane terminated as features are comparable to the B-plane of $Fe_3O_4(110)$. Drawing conclusions about surface reconstruction based

on STM images alone is unpractical. The analysis provided here indicates that a B-plane termination is more likely than an A-plane termination., although reconstructions are expected due to the polar nature of $Fe_3O_4(110)$. DFT calculations and the subsequent simulation of both STM images and RAS spectra are planned. These calculations combined with experimental STM, RAS and XPS measurements can provide quantitative insight into the atomic structure of the {111}-nanofaceted row reconstruction. LEED-IV measurements, and their comparison to theoretically calculated curves for different models, can also provide quantitative insight into the atomic structure of this reconstruction.

STS measurements indicate that the reconstruction exhibits 1D electronic states. The reconstruction therefore represents an ideal template for the growth of 1D nanostructures. As discussed above the electronic properties of the reconstruction can be altered by changing the preparation procedures. This may in turn alter the properties of 1D nanostructures. The existence of 1D states is correlated to the faceted nature of this reconstruction and more importantly the associated compressive and tensile strain at the ridge and trough of the row-structure.

Analysis of atomic steps and missing rows suggests that the {111}-nanofacets are present - adding weight to the conclusions of Parkinson *et al.* - and their coverage is maximised at these irregularities. This is unsurprising as nanofaceting reduces the surface energy. Increasing the size of the unit cell would increase the coverage of the {111}-nanofacetes. It is suggested that the reduction in surface energy associated with greater {111} coverage is at odds with the associated strain-energy. (1×3) likely represents the balance between the two.

The RAS and STM/STS measurements were performed on different single crystals, albeit from the same batch. Additionally, XPS measurements were performed in a different UHV chamber. A complete study of one single crystal performed without exposing the surface to ambient conditions can provide quantitative and complete analysis. Recently the XPS and STM chambers have been connected via a portable load-lock (vacuum suitcase) in

which a base pressure of 10^{-9} mbar is maintained while transporting between UHV chambers.

Chapter 7

$Fe_3O_4(110)$: Oxygen Vacancy Induced Surface Stabilisation

In this chapter a reconstruction is presented which forms as a result of sputtering prior to annealing. The presented reconstruction differs dramatically from the row reconstruction in that it is atomically flat, and therefore, demonstrates that a (110) termination can be stabilised.

This study was performed on a $Fe_3O_4(110)$ single crystal which has been polished and initially cleaned *in-situ* by sputter/anneals cycles. The crystal is from the same batch as the single crystal examined in chapter 6 and the polishing procedure and sputter/anneal cycles are identical to those described in that chapter. The STM tips used were polycrystalline tungsten which were electrochemically etched in NaOH. The bias voltage is applied to the surface with respect to the tip. STM experiments were conducted at 78 K.

In the proceeding sections, initially the formation of the atomically flat surface regions is discussed and subsequently the combination of a DFT study of the (110) surface with the simulation of STM images allows us to draw conclusions about this atomically flat surface structure. Furthermore, the calculation of the iron atoms spin-density distribution provides insight into the polarity-compensation mechanism.

7.1 Influence of sputtering

STM measurements depicted in figure 7.1(a) reveals a row reconstructed surface. The reconstructions periodicity of 25 Å (see figure 7.1(c)) closely matches three times the lattice parameter of 8.396 Å, and hence corresponds to the (1×3) reconstruction. Along the $[\bar{1}10]$ direction the rows break, revealing an atomically flat surface region, the blue ovals in figure 7.1(a) highlight its occurrence. The dimensions of individual areas of this structure range from (10 - 50) nm along the [001] direction and (1 - 10) nm along the $[\bar{1}10]$ direction. The area which is revealed when the rows break has for the

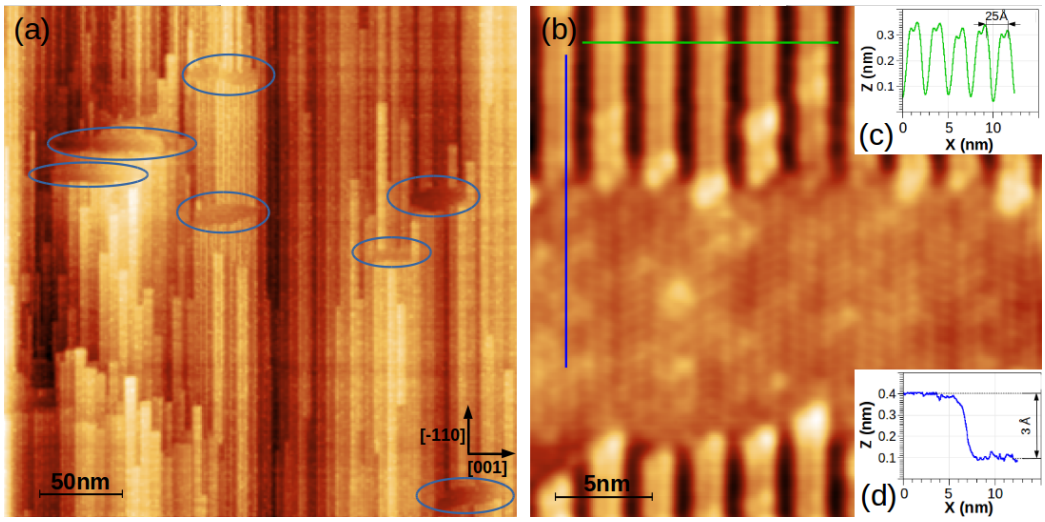

Figure 7.1: (a) $(320 \times 320)\,\mathrm{nm}^2$ STM image, $V = 1.56\,\mathrm{V}$, $I = 0.12\,\mathrm{nA}$. Row reconstructed structure with the rows' ridges running along the $[\bar{1}10]$ direction. The blue ovals highlight where the rows break, to reveal an atomically flat region. (b) $(29 \times 29)\,\mathrm{nm}^2$ STM image, $V = 1.58\,\mathrm{V}$, $I = 0.11\,\mathrm{nA}$. A region highlighted by the blue ovals in (a). (c) Line profile corresponding to the green line segment which demonstrates the row periodicity of 25 Å, this periodicity closely matches 3 times the surface unit cell parameter along the [001] direction. (d) Line profile corresponding to blue line segment illustrating that the two structures are separated vertically by 3 Å, this distance closely matches the distance between consecutive A- or B-planes. The co-existence of the two structures forms as a result of the sputtering prior to annealing. Without the sputtering step, the entire surface is row reconstructed.

vast majority of the time been observed below the adjacent rows. The two structures are separated vertically by 3 Å (figure 7.1(d)), which corresponds to the inter-planar distance between identical planes, i.e. A to A-plane or B to B-plane. Figure 7.2 displays a high-resolution STM image of such a region. Features are separated by 6 Å along the $[\bar{1}10]$ lattice direction. Along the [001] direction the distance between features varies periodically between ∼6 Å and ∼11 Å. The average atomic separation of ∼8.5 Å along [001] direction and the 6 Å separation along the $[\bar{1}10]$ lattice direction compare well to the surface unit cell parameters of 8.396 Å and 5.937 Å illustrated in figure 4.2.

The surface depicted in figures 7.1 and 7.2 was prepared by the following procedure: sputtering with Ar^+ ions with an energy of 0.5 keV for 1 h, annealing in an molecular oxygen partial pressure of 2.5×10^{-6} mbar at 750 °C

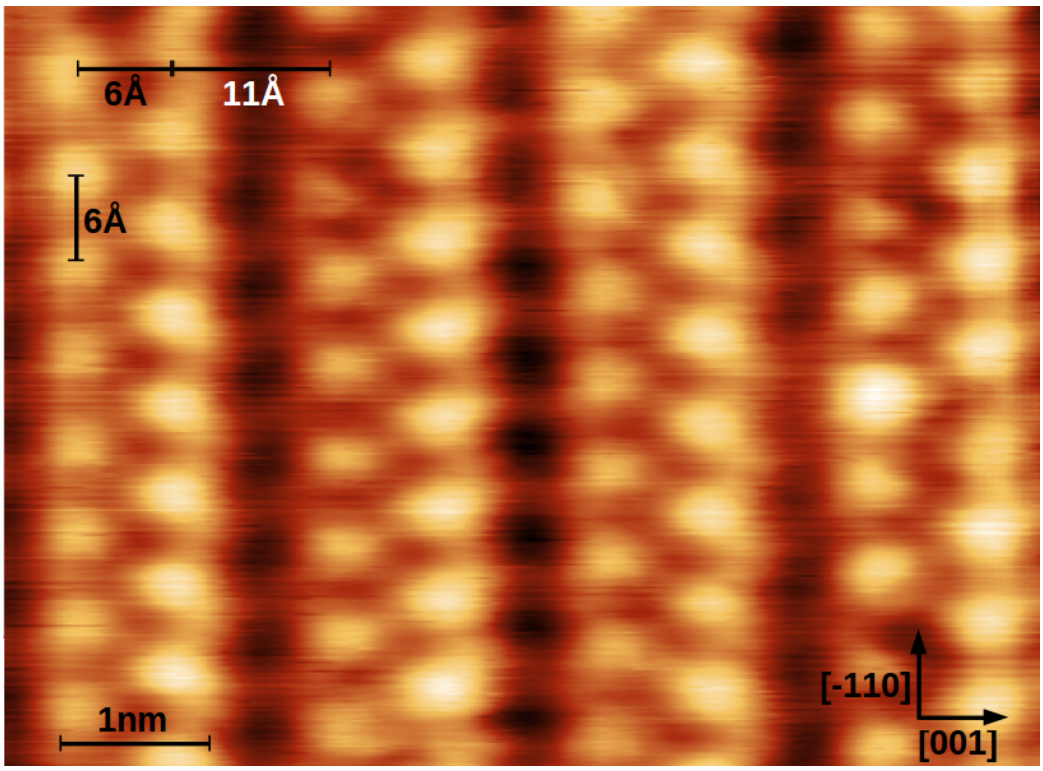

Figure 7.2: (70×50) Å^2 STM image of the atomically flat surface revealed when the rows break. $V = 0.87$ V, $I = 0.07$ nA.

for 1.5 h followed by a quick sputter anneal which consisted of sputtering at 0.6 keV for 10 mins and UHV flash annealing at 825 °C. STM measurements have been performed during each step of the cleaning procedure in order to shed light on the formation of the atomically flat surface structure: unsurprisingly STM measurements reveals that the sputtered surface is entirely disordered while after annealing in an oxygen atmosphere the row and atomically flat structure co-exist, as seen in figure 7.3(a). The co-existence of the two structures occurs regards of the annealing atmosphere: figure 7.3(b) depicts the surface structure observed after sputtering with Ar^+ ions (1 keV) for 3 hours followed by a 2 h anneal at 750 °C in a UHV environment. Further annealing in a UHV atmosphere leads to the gradual reduction in size and occurrence of the atomically flat surface regions until the row reconstruction is the only structure observed. Evidently, sputtering is pivotal to the presence of the atomically flat surface structure.

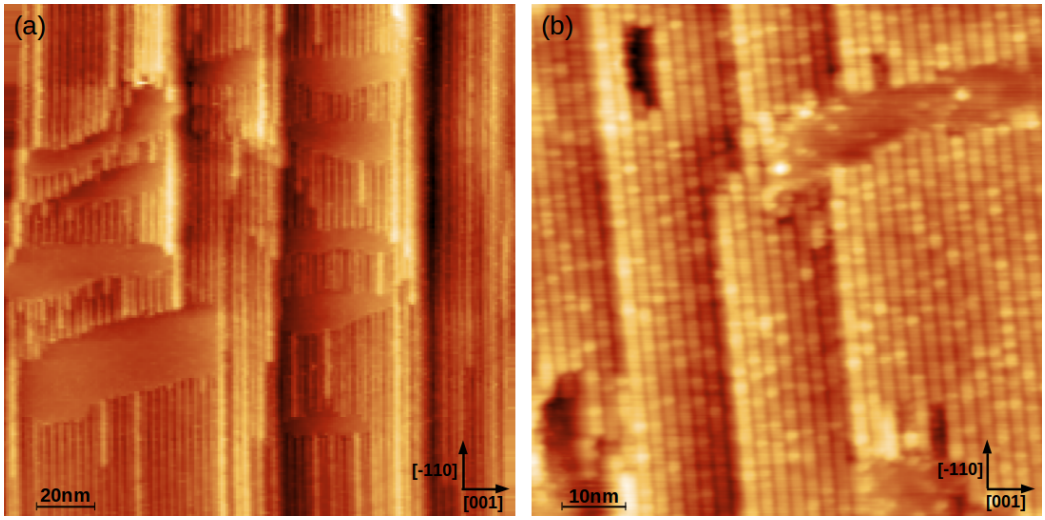

Figure 7.3: (a) $V = 1.10\,\mathrm{V}$, $I = 0.09\,\mathrm{nA}$ Surface structure after sputtering (0.5 keV, 1 h) and subsequently annealing in an oxygen environment (2.5×10^{-6} mbar, 750 °C, 1.5 h). (b) $V = 0.99\,\mathrm{V}$, $I = 0.14\,\mathrm{nA}$. Surface structure after sputtering (1 keV, 3 h) and subsequently annealing in UHV (2 h, 750 °C). Regardless of the annealing environment post sputter, the two structures co-exist.

Metal-oxide terminations which are strongly influenced by sputtering are reported throughout the literature. Moosburger *et al.* [103] demonstrated the the (2×1) reconstruction of $MoO_2(100)$ can be prepared by sputtering the (1×1) or (4×1) reconstructions. The formation of the (6×8) or (2×8) reconstructions of $SrTiO_3(110)$ depend on the sputtering dose [161]. The formation of these reconstructions are related to the change of stoichiometry induced by sputtering. Sputtering induced surface roughness can also influence surface structure: Lennie *et al.* observed pitting on the (001) termination of magnetite [187]. Pitting is defined as small enclosed areas which reside below the encompassing terrace. The phenomena is induced by sputtering which increases the surface roughness and is gradually removed by annealing. The surface structure of the "pit" is either the same structure of the surrounding terrace or is disordered. The observation in this work shows similarities: sputtering induces the co-existence of two structures and the minority-structure resides below the encompasses majority-structure. However, one key difference is that the two coexisting structures presented here are intrinsically different.

7.2 Density functional theory calculations

First principle calculations were performed in order to gain an understanding of the atomically flat surface revealed when the rows break. Full spin-polarised DFT calculations were performed using the Projector-Augmented-Wave (PAW) method [188] as implemented in the Vienna *Ab-initio* Simulation Package (VASP) [189–191]. The electron exchange and correlation were treated within the GGA using the Perdew-Burke-Ernzerhof (PBE) functional [95]. To account for the strong onsite Coulomb interaction of localised electrons, Hubbard U corrections with $U = 4.50\,\text{eV}$ [49] and $J = 0.89\,\text{eV}$ [50] ($U_{eff} = 3.61\,\text{eV}$) were applied on the Fe atoms. The $Fe_3O_4(110)$ surface was simulated by periodic supercells formed by slabs consisting of 10 unit layers and a 15 Å-wide vacuum. The positions of the atoms in the two layers most distant from the surface were constrained to account for the bulk. The Brillouin zone integrations were performed using a $2\times3\times1$ Monkhorst-Pack (MP)

grid [192]. The applied energy cutoff was 500 eV. Each system was relaxed until the Hellmann-Feynman force on each atom was less than 0.05 eV/Å.

7.2.1 Surface energy calculations

Li *et al.* performed a DFT study of the (110) termination of magnetite, it was concluded that the oxygen vacated B-plane represents the most energetically stable termination of those considered [185] as seen in figure 7.4. It should be noted that B-terminated magnetite contains two inequivalent oxygen atoms. All of which are bonded to one surface Fe_{oct}, half are bonded to one sub-surface Fe_{tet} and the other half are bonded to two sub-surface Fe_{oct}.

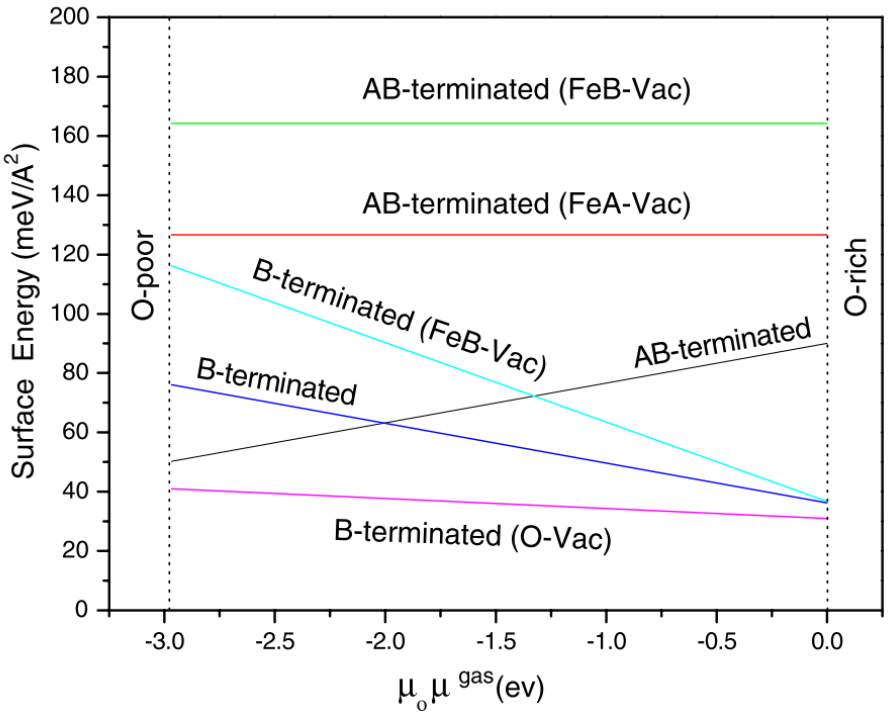

Figure 7.4: DFT calculations of the surface energy of different (110) surfaces of magnetite taken from Li *et al.* [185]. Oxygen surface vacancies on B-terminated magnetite are found to be the energetically favourable surface vacancy, of those considered, across the entire range of considered oxygen chemical potentials.

Henceforth, these inequivalent surface oxygen atoms on the B-terminated surface will be notated O_2 and O_3, with the subscript indicating the oxygen atoms coordination number. The aforementioned DFT study examined threefold oxygen vacancies only. Here, both of the possible oxygen vacancy coordinations on B-terminated $Fe_3O_4(110)$ are considered. To assist in understanding the proposed surface model, the reader is directed to figure 4.2 which depicts the A- and B-terminations of $Fe_3O_4(110)$. Initially, (1×1) B-terminated models which contain one surface oxygen vacancy were considered, the O_2 vacancy was found to be energetically favourable over the O_3 vacancy. With the features observed in STM images in mind, (1×2) models which contain two surface oxygen vacancies have been examined. Figure 7.5 depicts the (1×2) O_2 vacancy model. Every second O_2 atom is vacant along the row of O_2 atoms, and hence are separated by the $[\bar{1}10]$ unit cell distance, in the adjacent O_2 rows the vacancies are shifted by half the unit cell. The

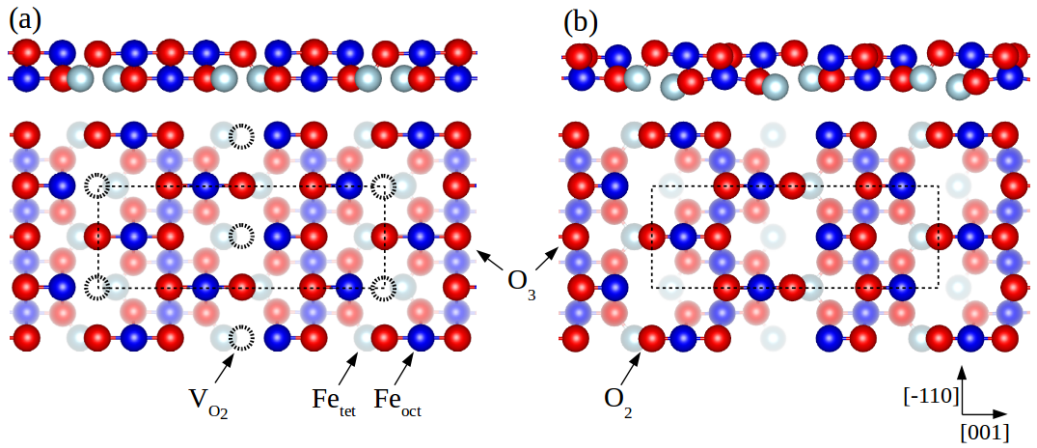

Figure 7.5: (a) depicts the side view and top view of the unrelaxed geometry of the B-terminated (1×2) twofold coordinated oxygen vacancy model. (b) depicts the fully relaxed geometry. Twofold and threefold coordinated surface oxygen atoms are indicated. O_2 atoms are bonded to one surface Fe_{oct} and one sub-surface Fe_{tet}, while O_3 atoms are bonded to one surface Fe_{oct} and two sub-surface Fe_{oct}. Rows of oxygen running in the $[\bar{1}10]$ direction alternate between O_2 and O_3. The black dashed circles in (a) highlight the surface O_2 vacancies.

(1×2) O_3 vacancy model is identical apart from the coordination of the surface oxygen vacancy.

DFT calculations of these two models indicate, as is the case for (1×1) models, that twofold coordinated oxygen represents the more energetically stable vacancy, with the difference in surface energy being $54\,\mathrm{meV/Å^2}$. The surface energy was calculated from equation 4.4. A value for the chemical potential of bulk magnetite, which is required to calculate the surface energy, is obtained by performing a bulk magnetite DFT calculation. Figure 7.5(a) and (b) depict the initial and relaxed geometry of the B-terminated O_2 vacancy model. Furthermore, the magnitude of the surface and sub-surface atoms relaxations are listed in table 7.1. It appears the oxygen vacated A-plane has not been investigated. However, anion vacancies on the electron defi-

Surface	[001]	[$\bar{1}$10]	[110]	Sub-surface	[001]	[$\bar{1}$10]	[110]
$O_2(1)$	0.13	0.00	0.25	$Fe_{tet}(1)$	0.17	0.00	-0.33
$Fe_{oct}(1)$	-0.17	0.00	0.07	O(1)	0.14	0.10	-0.01
$O_3(1)$	-0.30	0.00	-0.03	O(2)	0.14	-0.10	-0.01
$O_3(2)$	0.30	0.00	-0.03	$Fe_{oct}(1)\&(2)$	0.00	0.00	0.28
$Fe_{oct}(2)$	0.17	0.00	0.07	O(3)	-0.14	-0.10	-0.01
$O_2(2)$	-0.13	0.00	0.25	O(4)	-0.14	0.10	-0.01
$Fe_{oct}(3)$	-0.03	0.00	-0.09	$Fe_{tet}(2)$	-0.17	0.00	-0.33
$O_3(3)$	-0.12	0.00	-0.06	$Fe_{tet}(3)$	-0.12	0.00	0.19
$O_3(4)$	0.12	0.00	-0.06	O(5)	0.03	0.05	0.16
$Fe_{oct}(4)$	0.03	0.00	-0.09	O(6)	0.03	-0.05	0.16
				$Fe_{oct}(3)\&(4)$	0.00	0.00	0.23
				O(7)	-0.03	-0.05	0.16
				O(8)	-0.03	0.05	0.16
				$Fe_{tet}(4)$	0.12	0.00	0.19

Table 7.1: Relaxation in Ångström of the surface and sub-surface atoms within the B-terminated O_2 surface vacancy model (figure 7.5). Top to bottom corresponds to atoms from left to right in the unit cell depicted in figure 7.5(b). Positive magnitudes in the [001] and [$\bar{1}$10] directions follow the direction of the vectors in figure 7.5, while a negative [110] magnitude corresponds to a relaxation into the bulk.

cient A-plane are likely to give rise to an energetically unfavourable surface termination.

7.2.2 Simulation of STM images

STM images of the (1×2) B-terminated O_2 vacancy model have been simulated. Simulations correspond to the Tersoff-Hamann scheme [193] in which the unknown electronic structure of the tip is replaced by a simple model system: the tip is approximated to be point-like and its wavefunction is s-type and electronically flat. The tunneling current then depends on the integrated partial DOS of the unperturbed surface states at the tip position.

Two high resolution STM images are shown in figure 7.6(a) and (b), below each of the STM images sit the simulated STM images of the (1×2) B-terminated O_2 vacancy model shown in figure 7.5. The simulated images show a good agreement with experiment. The black dashed rectangle in each of the simulated images represents the (1×2) surface unit cell, positioned identically to the surface unit cell depicted in figure 7.5(b). All of the features within the surface unit cell are positioned above the four surface Fe_{oct} atoms. This is not surprising since the Fe_{oct} 3d level sits at the Fermi level [61, 64] and the oxygen 2p level sits several eV below the Fermi level [61]. Previous studies of the (111) and (001) surfaces of magnetite also interpreted protrusions in constant current STM images as Fe_{oct} atoms [99, 104]. The presence of surface oxygen vacancies leads to the inequivalance of the iron surface atoms; The unit cell in figure 7.6(c) & (d), which depicts the atoms of the terminating layer, reveal that the brightest features in each of the simulated images differ. In figure 7.6(c) the two brightest features are positioned above Fe_{oct} atoms which are bonded to two surface oxygen atoms, in contrast, the brightest features in figure 7.6(d) are positioned above Fe_{oct} atoms which are bonded to one surface oxygen atom. This is further emphasised by the simulated STM images of B-terminated $Fe_3O_4(110)$ with no surface vacancies, depicted in figure 7.6(e) & (f), which are calculated at $+0.75$ and $+1.00$ eV. In these images the iron atoms, which are all bonded to two surface oxygen surface atoms, show only very minor differences.

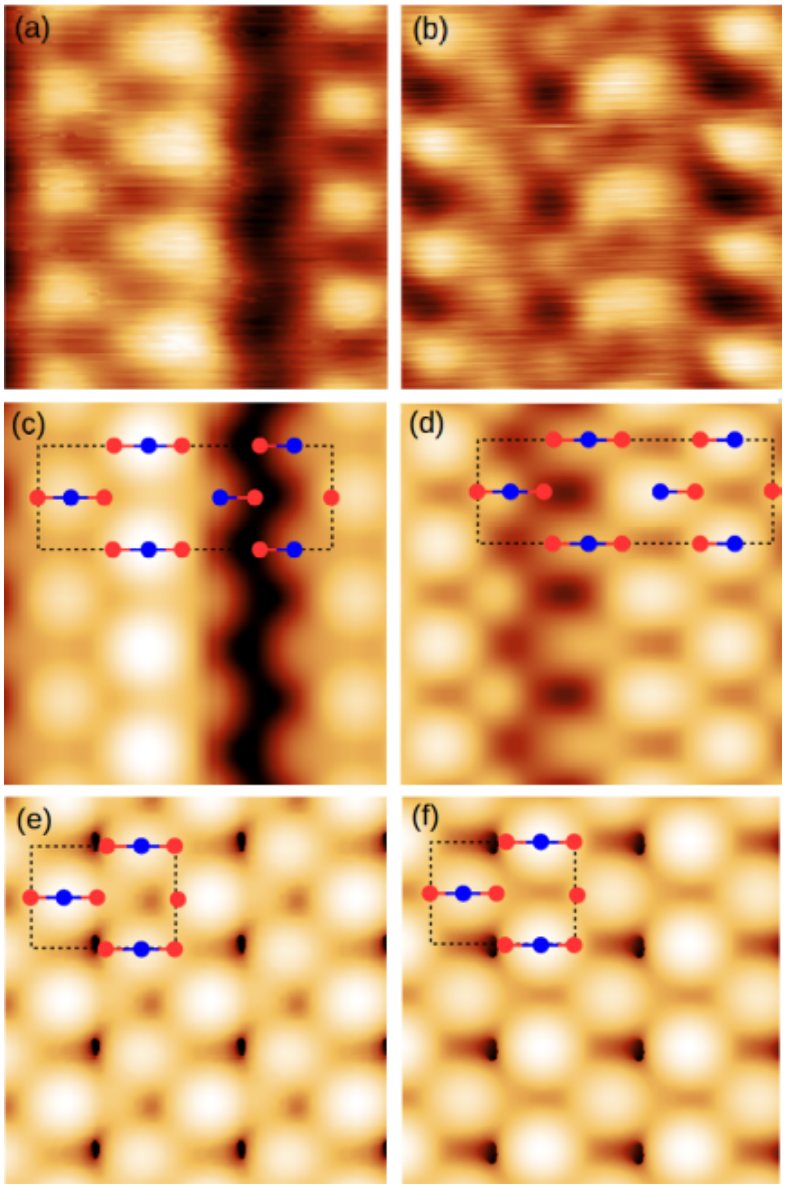

Figure 7.6: (a),(b) High resolution (21×21) Å^2 STM images. (a) $V = 0.87$ V, $I = 0.07$ nA, (b) $V = 0.60$ V, $I = 0.78$ nA. Simulated STM images of the proposed model calculated at 0.87 V (c) and 0.60 V (d), respectively. The simulated STM images correspond to a Tersoff-Hamann calculation of the (1×2) B-terminated O_2 vacancy model. The black dashed rectangle in (c) and (d) corresponds to the surface unit cell of the model, identical to the surface unit cell illustrated in figure 7.5(b). Blue circles represent iron surface atoms, while red circles represent oxygen surface atoms. (e) and (f) represent the simulated STM images of B-terminated $Fe_3O_4(110)$ with no vacancies, calculated at energies $+0.75$ eV and $+1.00$ eV.

7.2.3 Spin density distributions

Figure 7.7 illustrates the calculated spin density distributions of the iron atoms in the first four layers of the proposed surface model. Blue and silver spin densities represent the majority and minority spin orientations, respectively. Fe_{oct} and Fe_{tet} sites are antiferromagnetically coupled, as is the case for bulk magnetite. A spherical distribution indicates a half filled d-band, and hence Fe^{3+} character. Deviation from a spherical distribution indicates an increased occupation of the $3d^6$ orbital, and hence Fe^{2+} character [109].

The four surface Fe_{oct} atoms all display Fe^{2+} character. The two that have an in-plane dangling bond due to an oxygen vacancy display greater Fe^{2+} character. This is in agreement with a previous study of $Fe_3O_4(001)$, which demonstrated a progressive reduction of surface iron to Fe^{2+} as the surface Fe/O ratio was increased [109]. The remaining Fe_{oct} atoms all display close to spherical character, this can be interpreted as $Fe^{2.5+}$ character, as is the case with bulk Fe_{oct}. Fe_{tet} atoms which have a bond removed due to the

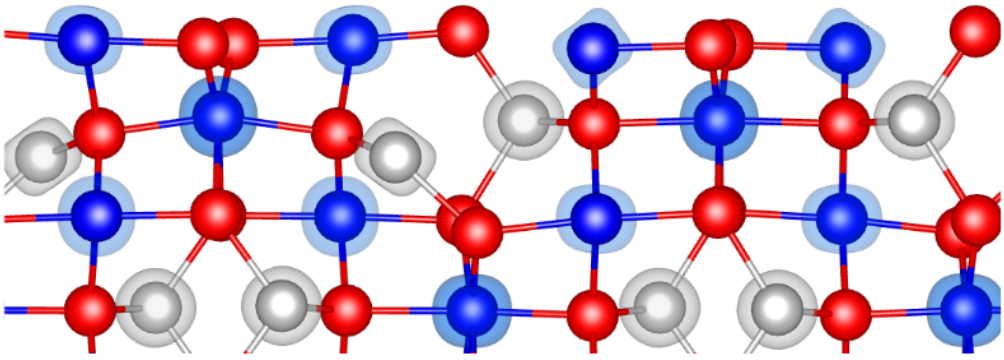

Figure 7.7: Side view illustration of the B-terminated O_2 vacancy model. Overlayed onto the iron atoms is their respective spin density distributions obtained from DFT calculations. Blue and silver distributions represent the majority and minority spin channels. A spherical spin distribution indicates a half filled d-band , and hence Fe^{3+} character. Any deviation from spherical shape indicates increased $3d^6$ occupation, and hence Fe^{2+} character. Surface Fe_{oct} atoms and Fe_{tet} atoms, with a dangling bond due to presence of surface oxygen vacancies, all display 2+ character.

existence of surface oxygen vacancies exhibit Fe^{2+} character. The remaining Fe_{tet} atoms display Fe^{3+} character, as is the case for bulk magnetite.

A polar surface can compensate for its polarity by reducing its surface charge to half that of the bulk value [6, 120], this is detailed further in section 4.1.2. One must take care when defining the surface region; When considering polarity compensation we define the surface region as the area which deviates from the bulk. For the considered model the surface region is defined as the termination plane and first sub-surface layer. The sub-surface layer is included as the Fe_{tet} atoms, which are missing a bond due to the presence of the surface oxygen vacancies, exhibits Fe^{2+} character opposed to Fe^{3+} character of bulk-like Fe_{tet}. Considering that we are dealing with a (1×2) model and a bulk-like B-plane (a B-plane is immediately below the surface region) with (1×2) size has a net charge of -6 electrons, the surface region must have a charge deficit of 3 electrons to be polar compensated.

In order to examine how the existence of oxygen vacancies and predicted Fe_{oct} charge ordering influences the stability of this surface, the surface region charge has been calculated for the following ions charges: the octahedrally coordinated surface iron are designated Fe^{2+}, while the remaining Fe_{oct} are designated $Fe^{2.5+}$, as they are in the bulk. The tetrahedrally coordinated iron, which has a dangling bond due to the existence of the oxygen surface vacancies, are designated Fe^{2+}, while the other Fe_{tet} atoms are Fe^{3+}, as they are in the bulk. Starting with the terminating layer, two surface oxygens are bonded to two sub-surface $Fe^{2.5+}_{oct}$(6-fold) and one surface Fe^{2+}_{oct}(4-fold), resulting in a charge of $\frac{2.5}{6} + \frac{2.5}{6} + \frac{2}{4} = \frac{4}{3}\,e^-$ each. A further two surface oxygens are bonded to two sub-surface $Fe^{2.5+}_{oct}$(6-fold) and one surface Fe^{2+}_{oct}(3-fold), resulting in a charge of $\frac{2.5}{6} + \frac{2.5}{6} + \frac{2}{3} = \frac{3}{2}\,e^-$ each. Lastly, two surface oxygens are bonded to one sub-surface Fe^{3+}_{tet}(4-fold) and one surface Fe^{2+}_{oct}(4-fold), resulting in a charge of $\frac{3}{4} + \frac{2}{4} = \frac{5}{4}\,e^-$ each. Therefore, considering there are four Fe^{2+}_{oct} within the terminating layers unit cell, the charge excess per unit cell is $2(\frac{4}{3}) + 2(\frac{3}{2}) + 2(\frac{5}{4})$ - $4(2) = \frac{1}{6}\,e^-$. Turning to the sub-surface layer, four oxygens are bonded to one surface Fe^{2+}_{oct}(3-fold), two $Fe^{2.5+}_{oct}$(6-fold) and one Fe^{3+}_{tet}(4-fold), resulting in a charge of $\frac{2}{3} + \frac{2.5}{6} + \frac{2.5}{6} + \frac{3}{4} = \frac{9}{4}\,e^-$. A further four oxygens are bonded to one surface Fe^{2+}_{oct}(4-fold), two $Fe^{2.5+}_{oct}$(6-fold)

and one Fe^{2+}_{tet}(3-fold), resulting in a charge of $\frac{2}{4}+\frac{2.5}{6}+\frac{2.5}{6}+\frac{2}{3}=2e^-$. Therefore, considering there are four $Fe^{2.5+}_{oct}$, two Fe^{3+}_{tet} and two Fe^{2+}_{tet} within the (1×2) area of the sub-surface layer, the charge deficit per (1×2) area is $4(2.5)+2(3)+2(2)-4(2)-4(\frac{9}{4})=3e^-$. Finally, considering the terminating and sub-surface layers exhibit charge excess and deficits of $\frac{1}{6}e^-$ and $3e^-$, respectively, the surface region charge deficit is equal to $2.83e^-$. As was discussed above, to achieve polar compensation this surface region is required to have a charge deficit of $3e^-$. Increased surface covalent character, out of plane charge transfer or a combination of both can lead to polar compensated and stable surface. It is noted that spin density distributions do not provide quantitative analysis of the cation charges. However, the analysis provided here demonstrates that the combination of oxygen surface vacancies and charge ordering can contribute towards a polar compensated and stable termination.

The largest and brightest features in figure 7.2 form rows separated by 17 Å along the [001] direction, the orientation of these features differ from row to row. This indicates that the surface exhibits longer range order than the (1×2) model in figure 7.5. It is possible minor relaxations along the $[\bar{1}10]$ direction to give rise to these asymmetries. A (1×4) model, which corresponds to the (1×2) model depicted in figure 7.5 doubled in the [001] direction, has been allowed to relax. No additional distortions along the $[\bar{1}10]$ direction were observed. In the present work, the nature of these subtle features or the size of the unit cell are not determined. However, the good agreement between experimental and simulated STM images of the B-terminated model containing twofold oxygen vacancies - which have been predicted by DFT calculations to be the most energetically stable surface vacancy of those considered - leads to the strong suggestion that the investigated surface is B-terminated and contains an ordered array of twofold oxygen vacancies.

Due to the fact that this termination occupies the minority of the surface, further experiments to verify the proposed model are limited. IV-LEED and angular resolved XPS would clearly be ideal experiments. In theory, this model could be tested by dosing the surface with small amounts of H_2O. The surface oxygen vacancies should, in theory, provide an preferential absorption

site for the water molecule. This could lead to the presence of a surface hydroxide, which should be identifiable by the combination of STM and DFT.

7.3 Discussion & conclusions

Sputtering prior to annealing leads to the co-existence of two surface structures: the row reconstruction and an atomically flat surface structure. When the crystal is annealed alone, in oxygen or UHV environments, the row reconstruction is dominant. The row reconstruction forms as a result of faceting which exposes energetically favourable {111}-planes. The observation of the atomically flat surface structure illustrates that a (110) termination can be stabilised. Clearly, the atomically flat surface structure is stabilised by an entirely different mechanism to that which stabilises the row reconstruction.

DFT calculations of the Fe_3O_4(110) surface indicate that twofold coordinated oxygen represent the most energetically stable oxygen vacancy on the B termination of Fe_3O_4(110). The comparison between simulated and experimental STM images indicates that the atomically flat surface region corresponds to this aforementioned B-terminated surface containing an ordered array of twofold coordinated oxygen vacancies. DFT calculations of the spin density distributions indicate charge ordering of surface and sub-surface octahedral iron. Charge ordering on this oxygen vacated surface contributes towards a polar compensated termination, additional polarity compensation mechanisms such as increased surface covalent character and/or charge transfer can lead to a stabilised surface. The determination of the surface structure and specifically the mechanism which stabilises this surface may provide insight into how polar and transition metal oxide surfaces reconstruct.

Altering the sputtering dose and annealing temperature and time does not see a vast increase of the coverage of atomically flat surface regions. It appears that the atomically flat structure is not an initial state which the row reconstruction eventually encompasses, but forms in-parallel with the row reconstruction. It is clear that the state of the surface post sputter is a vital initial state, prior to annealing, which allows for the two structures to

co-exist. Their coexistence illustrates that there are several possible terminations with only moderate differences in formation energies. Considering that annealing reduces the coverage of the atomically flat surface regions, it is reasonable to conclude that the row reconstruction is energetically favourable.

Chapter 8

Discussion & Conclusions

In this work the study of (110) terminated magnetite and strontium titanate has been presented, with the core focus being on the former. The work can be split into two parts: (1) the investigation, primarily by STM, of two contrasting Fe_3O_4(110) surface reconstructions: the known but far from fully characterised {111}-nanofaceted row reconstruction and an atomically flat surface reconstruction. (2) The anisotropic optical response of Fe_3O_4(110) and $SrTiO_3$(110) terminations investigated by RAS.

Beginning with the RAS study presented in chapter 5, for all the examined terminations RAS is sensitive to the influence that the surface region has on the bulk-like region in the vicinity of the selvedge. The anisotropic optical response is interpreted to originate from small anisotropic shifts in the energy of bulk-like optical transitions.

DFT calculations of the {111}-nanofaceted row reconstruction confirm that the structure exhibits an anisotropic strain gradient along the surface normal. The modification of bulk-like states and the associated RAS spectra originate from this anisotropic strain gradient.

The anisotropic optical response of the as-polished Fe_3O_4(110) surface and $SrTiO_3$(110) surface terminations are also interpreted to originate from anisotropic strain. The strain of the as-polished Fe_3O_4(110) surface is suggested to originate from the maghemite overlayer which forms in ambient conditions. The altered stoichiometry of $SrTiO_3$(110) terminations as a result

of *ex-situ* pre-cleaning and/or *in-situ* cleaning procedures is suggested to give rise to anisotropic strain of bulk-like states. Furthermore, RAS is sensitive to the contrasting modification of bulk-like states for different $SrTiO_3(110)$ terminations.

RAS is extremely sensitive to the formation of an anisotropic conductance within the $SrTiO_3$ bandgap. The conductance is a result of well known oxygen vacancies, which form during vacuum annealing and are correlated to a metallic state and modification of the Ti 2p core level identified by UPS and XPS, respectively. This IR lineshape is suggested to be a combination of mid-gap defects state, induced by a significant number of oxygen vacancies in the surface region, and a free-electron contribution. Finally, the electron gas owes its anisotropy to the influence of an anisotropic surface termination and is located close to the termination. The sensitivity of RAS to the electron gas is promising for work on $SrTiO_3/LaAlO_3$ heterostructures which displays a Q2DEG at the interface. The origin of the Q2DEG appears to be some combination of oxygen vacancies in the $SrTiO_3$ substrate, charge transfer to the interface to compensate for the polar nature of $LaAlO_3$ and the influence of the $SrTiO_3$ termination. RAS represents a non-destructive probe, which can monitor the formation of the electron gas during heterostructure growth and examine the influence of different $SrTiO_3$ terminations and $LaAlO_3$ growth conditions and thicknesses. RAS represent a technique which has the possibility to unambiguously determine the mechanism(s) behind the formation of the Q2DEG at the $SrTiO_3/LaAlO_3$ interface under different conditions. Furthermore, in theory, different mechanisms can be examined individually. Such insight has wider implications to heterostructure growth in general.

Turning to the {111}-nanofaceted row reconstruction investigated in chapter 6, XPS measurements indicate the reconstruction exhibits increased Fe^{2+}/Fe^{3+} and Fe/O ratios relative to stoichiometric magnetite. The reconstruction is very sensitive to the preparation procedure. Slightly modifying the conditions sees the formation of slightly different surface structures related to an altered stoichiometry. While the {111}-nanofaceted row reconstruction is reduced, STS and RAS measurements indicate that preparing the reconstruction in oxygen or vacuum environments gives rise to differ-

ent electronic properties. In light of the aforementioned XPS measurements, it is concluded that the reconstruction is stable across some stoichiometry range and the change in stoichiometry is correlated to minor changes in the electronic structure.

The analysis of missing rows and atomic steps of the {111}-nanofaceted row reconstruction is aided by considering the strain identified by RAS and DFT: At these irregularities the {111} coverage is maximised. The unit cell size of (1×3) opposed to a larger periodic unit, which would increase the energetically favourable {111} coverage, is understood by considering that larger {111} coverage is associated with an increased strain energy. (1×3) periodicity likely represents a balance between the two. An interesting question, in the authors opinion, is what dictates faceting dynamics. The competition behind facet induced strain and the the reduction in surface energy associated with facet coverage, as is the case for {111}-faceted $Fe_3O_4(110)$, is one such mechanism which can dictate facet dynamics.

1D electronic states running perpendicular to the row periodicity of the {111}-nanofaceted row reconstruction are observed in STS measurements. These electronic states are understood in terms of the anisotropic strain in the terminating layers identified by RAS measurements and DFT calculations. Compressive and tensile strain along the $[\bar{1}10]$ lattice direction give rise to the inequivalence of electronic states. The existence of 1D electronic states highlights the potential of this reconstruction as a template for the growth of 1D nanostructures.

This work highlights the potential of combining surface sensitive measurements with RAS measurements in the case of bulk isotropic metal oxides. RAS is sensitive to the influence the surface termination has on the near-selvedge bulk, however this information indirectly provides insight into aspects of the surface termination

The absorption dynamics and properties of grown 1D nanostructures will very likely be influenced by the stoichiometry and correlated electronic properties of the {111}-nanofaceted row reconstruction template. Firstly, great care must be taken in preparing the template, as it will dictate the nanostructure properties. Secondly, this reconstruction represents a robust template,

as the influence of the different stoichiometries and correlated electronic properties on the nanostructure properties can be examined. RAS represents a non-invasive tool which is sensitive to the differing properties of the template, and hence, can used in-real time to monitor the state of the template. Considering the highly anisotropic nature 1D nanostructures, RAS can, in theory, be employed to monitor the growth and properties of these nanostructures in real-time. This approach can clearly be advantageous for nanostructure growth.

Analysis of high resolution STM images leads to the tentative suggestion that the {111}-nanofaceted row reconstruction is $Fe_3O_4(110)$ B-plane terminated. The reduced Fe^{2+}/Fe^{3+} and Fe/O ratios indicated by XPS measurements are suggested to arise from {110} oxygen surface vacancies, which are found to be the energetically favourable surface vacancy by DFT calculations, and/or reduction of the {111} facets. However, the existence of sub-surface cation interstitials cannot be ruled out.

Finally, in chapter 7 the formation and structure of the atomically flat surface reconstruction of $Fe_3O_4(110)$ is examined. Sputtering prior to annealing gives rise to the coexistence of both the row reconstruction and the atomically flat surface structure, and it appears the latter termination cannot be isolated. DFT calculations of the $Fe_3O_4(110)$ surface indicate that twofold coordinated oxygen represents the most energetically stable oxygen vacancy on the B-termination of $Fe_3O_4(110)$. The comparison between simulated and experimental STM images indicates that the atomically flat surface structure corresponds to this aforementioned B-termination containing an ordered array of twofold coordinated oxygen vacancies.

DFT calculations of the spin density distributions indicate charge ordering of surface and subsurface octahedral iron. Charge ordering on this oxygen vacated surface contributes towards a polar compensated termination, additional polarity compensation mechanisms such as increased surface covalent character and/or charge transfer can lead to a stabilised surface.

The determination of the surface structure and specifically the mechanism which stabilises this surface may provide insight into how polar and metal oxide surfaces in general reconstruct. The existence of two drastically

different structures on the same surfaces indicates that the surface can be stabilised by more than one mechanism. This observation, along with the intricacy of the discussed surface structure, highlights the complexity of both magnetite and transition metal oxide surfaces in general.

In summary, metal oxide surfaces have been studied for approximately a quarter of a century, which has resulted in their use in a range of applications. Moreover, metal oxides and their terminations remain candidates for emerging and future technologies. As such, the continued fundamental study of metal oxide terminations remains a priority. These surfaces are inherently difficult to characterise, as demonstrated in this work. The use of different techniques, such as RAS, and the investigation of the insight such techniques can provide, is of great importance to further metal oxide surface science. Furthermore, the combination of new and commonly used techniques, which provide contrasting insight, can greatly aid in these fundamental studies. The studies presented here, of (110) terminated Fe_3O_4 and $SrTiO_3$, provide fundamental insight into the nature and formations of different surface terminations. This is of great importance for nanostructure and heterostructure growth and properties as well as of fundamental value to the surface science community. The RAS study of these terminations, being the first of its kind conducted on metal oxide surface reconstructions, demonstrates the value of its use and what insight it can provide.

8.1 Future work

Single crystalline $SrTiO_3$ is insulating and therefore STM experiments are limited. The crystals only becomes conductive enough to approach with the STM tip once the formation oxygen vacancies formed during vacuum annealing increases the conductivity to some critical value. The crystal was found to be conductive enough to approach after annealing at 800 °C for one hour (annealing was performed stepwise at 100 °C intervals). This limits the reconstructions which can be examined by STM and prevents a comprehensive RAS and STM study from being performed on $SrTiO_3$ single crystals. STM studies are routinely performed on Nb:$SrTiO_3$(110) single crystals, since dop-

ing with a small percent of niobium drastically increases the conductivity of strontium titanate single crystals. A combined STM and RAS study of single crystal Nb:$SrTiO_3$(110) can potentially provide additional insight into the structure of $SrTiO_3$(110) reconstructions.

This work has revealed two novel $SrTiO_3$(110) surfaces, a c(2×2) termination and a nearly single domain (1×4) termination. To the author's knowledge, a c(2×2) structure has not been investigated and the (1×4) termination has only been observed to coexist as the minority reconstruction with the known $(n \times 1)$ series of reconstructions. The c(2×2) surface was not well ordered, and a significant carbon contamination remained. Sputter/anneal cycles may remove the contamination and produce a cleaner surface with a better degree of order. If a well ordered c(2×2) termination is achieved, this surface will be characterised by STM and RAS. A similar study is planned for the (1×4) termination. RAS is sensitive to the influence that the selvedge has on the near-selvedge bulk and therefore provides different information to, for example, surface sensitive STM. Therefore, a combined STM and RAS study and the subsequent simulation of STM images and RAS spectra can provide comprehensive characterisation.

The sensitivity of RAS towards the Q2DEG near the surface of reconstructed $SrTiO_3$(110) terminations opens up the possibility to monitor the formation of the anisotropic Q2DEG at the $LaAlO_3/SrTiO_3$(110) interface *in-situ* and in real-time. Furthermore, the contribution from different mechanisms can be examined. Prior to performing such an experiment, the optical anisotropy of $LaAlO_3$(110) would be characterised by RAS. Multiple experiments can be envisaged which will examine to formation of the Q2DEG at the $LaAlO_3/SrTiO_3$(110) interface *in-situ* and in real-time: (1) $LaAlO_3$ growth on different $SrTiO_3$ terminations, whose presence can be confirmed by RAS. The influence of the growth on the $SrTiO_3$ termination can be monitored by RAS: $LaAlO_3$ is a wide bandgap ($\sim$5 eV) material, while $SrTiO_3$ has a bandgap of $\sim$3.3 eV. Therefore, the RAS features below $\sim$5 eV, and above $\sim$3.3 eV, should in theory be due to the $SrTiO_3$ termination. (2) $LaAlO_3$ growth on a $SrTiO_3$ substrate which doesn't exhibit the Q2DEG prior to growth, if possible. This can isolate the proposed charge transfer to the

interface from the polar, and hence, unstable $LaAlO_3$ termination. (3) Dependence on the $LaAlO_3$ thickness: The electron gas is reported to form only after the $LaAlO_3$ reaches some critical thickness. (4) Influence of the post-growth treatment, such as sample cool down in oxygen atmospheres, which are performed to counter the growth conditions which typically induce oxygen vacancies in the $SrTiO_3$ surface region. Finally, RAS can monitor this state without exposing heterostructures to ambient conditions which may influence the interface, especially at small $LaAlO_3$ thickness where the interface is close to the surface.

DFT calculations and the subsequent simulation of both STM images and RAS spectra can provide quantitative insight into the atomic structure of the {111}-nanofaceted row reconstruction. Furthermore, the fully relaxed geometry and the simulation of RAS spectra can provide insight into the bands which are modified by the anisotropic strain gradient in the terminating layers. $Fe_3O_4(001)$ has recently been used as the prototype template for the initial study of single atom catalysis [10, 12–15]. The fundamental and comprehensive understanding of the {111}-nanofaceted row reconstruction is required to probe this surface's potential as a template for the study of single atom catalysis.

The 1D states of the {111}-nanofaceted row reconstruction can provide a template for the growth and study of 1D nanostructures. Multiple experiments are under consideration. For example, the 1D states and the periodic unit length of 2.5 nm may provide an excellent template for the growth of porphyrin chains. This reconstruction offers a robust template for the growth and study of nanowires: the stoichiometry and correlated electronic properties of the {111}-nanofaceted row reconstruction template are strongly influenced by the preparation procedure. RAS is sensitive to this modification, and therefore, can be utilized in real-time to control the surface structure, and furthermore, can be employed to monitor the growth and properties of highly anisotropic nanowires.

These studies have been conducted across two chambers. Work has just been completed to connect XPS and STM chamber via a portable load-lock, in which a base pressure of 10^{-9} mbar is maintained while transporting

between UHV chambers. A complete study of one single crystal performed without exposing the surface to ambient conditions can provide quantitative and complete analysis of particular surface reconstructions.

In summary, the presented research can motivate future experiments for researchers working in areas ranging from surface science, thin film, heterostructure and nanostructure growth and computational solid state physics. To name a few, this work opens up the possibility to study new $SrTiO_3(110)$ surface terminations, utilise the faceted $Fe_3O_4(110)$ termination as a template for the growth of nanowires, investigate the Q2DEG at the $SrTiO_3/LaAlO_3$ interface in real-time during heterostructure growth and computationally model and compare RAS spectra, which would represent a new means of characterising metal oxide surface reconstructions.

Bibliography

[1] J. Haber. Catalysis by transition metal oxides. In *Solid State Chemistry in Catalysis*, pages 3–21. American Chemical Society, 1985.

[2] J. J. Richard. *Catalytic ammonia synthesis: fundamentals and practice*. Springer Science & Business Media, 2013.

[3] H. Adkins and W. R. Peterson. The oxidation of methanol with air over iron, molybdenum, and iron-molybdenum oxides. *Journal of the American Chemical Society*, 53(4):1512–1520, 1931.

[4] D. S. Newsome. The water-gas shift reaction. *Catalysis Reviews*, 21(2):275–318, 1980.

[5] S. C. Christoforou, E. A. Efthimiadis, and I. A. Vasalos. Catalytic reduction of NO and N_2O to N_2 in the presence of O_2, C_3H_6, SO_2, and H_2O. *Industrial & engineering chemistry research*, 41(9):2090–2095, 2002.

[6] C. Noguera. Polar oxide surfaces. *Journal of physics. Condensed matter*, 12(31):R367–R410, 2000.

[7] O. Lübben, S. A. Krasnikov, A. B. Preobrajenski, B. E. Murphy, S. I. Bozhko, S. K. Arora, and I. V. Shvets. Self-assembly of Fe nanocluster arrays on templated surfaces. *Journal of Applied Physics*, 111(7):07B515, 2012.

[8] O. Lübben, S. A. Krasnikov, B. Walls, N. N. Sergeeva, B. E. Murphy, A. N. Chaika, S. I. Bozhko, and I. V. Shvets. Nanoclusters and nano-

lines: the effect of molybdenum oxide substrate stoichiometry on iron self-assembly. *Nanotechnology*, 28(20):205602, 2017.

[9] G. S. Parkinson, Z. Novotny, G. Argentero, M. Schmid, J. Pavelec, R. Kosak, P. Blaha, and U. Diebold. Carbon monoxide-induced adatom sintering in a Pd-Fe_3O_4 model catalyst. *Nature Materials*, 12(8):724–728, 2013.

[10] R. Bliem, R. Kosak, L. Perneczky, Z. Novotny, O. Gamba, D. Fobes, Z. Mao, M. Schmid, P. Blaha, U. Diebold, and et al. Cluster nucleation and growth from a highly supersaturated adatom phase: silver on magnetite. *ACS Nano*, 8(7):7531–7537, 2014.

[11] J. Pavelec, J. Hulva, D. Halwidl, R. Bliem, O. Gamba, Z. Jakub, F. Brunbauer, M. Schmid, U. Diebold, and G. S. Parkinson. A multi-technique study of CO_2 adsorption on Fe_3O_4 magnetite. *The Journal of Chemical Physics*, 146(1):014701, 2017.

[12] G. S. Parkinson, Z. Novotny, P. Jacobson, M. Schmid, and U. Diebold. Room temperature water splitting at the surface of magnetite. *Journal of the American Chemical Society*, 133(32):12650–12655, 2011.

[13] R. Bliem, J. E. S. van der Hoeven, J. Hulva, J. Pavelec, O. Gamba, P. E. de Jongh, M. Schmid, P. Blaha, U. Diebold, and G. S. Parkinson. Dual role of CO in the stability of subnano Pt clusters at the Fe_3O_4(001) surface. *Proceedings of the National Academy of Sciences*, 113(32):8921–8926, 2016.

[14] R. Bliem, J. Pavelec, O. Gamba, E. McDermott, Z. Wang, S. Gerhold, M. Wagner, J. Osiecki, K. Schulte, M. Schmid, P. Blaha, U. Diebold, and G. S. Parkinson. Adsorption and incorporation of transition metals at the magnetite Fe_3O_4(001) surface. *Physical Review B*, 92(7):075440, 2015.

[15] Z. Novotny, G. Argentero, Z. Wang, M. Schmid, U. Diebold, and G. S. Parkinson. Ordered array of single adatoms with remarkable thermal

stability: Au/Fe_3O_4(001). *Physical Review Letters*, 108(21):216103, 2012.

[16] A. Ohtomo and H. Y. Hwang. A high-mobility electron gas at the $LaAlO_3$/$SrTiO_3$ heterointerface. *Nature*, 441(7089):120–120, 2006.

[17] A. Brinkman, M. Huijben, M. van Zalk, J. Huijben, U. Zeitler, J. C. Maan, W. G. van der Wiel, G. Rijnders, D. H. A. Blank, and H. Hilgenkamp. Magnetic effects at the interface between non-magnetic oxides. *Nature Materials*, 6(7):493–496, 2007.

[18] H. M. Christen, D. H. Kim, and C. M. Rouleau. Interfaces in perovskite heterostructures. *Applied Physics A*, 93(3):807–811, 2008.

[19] S. A. Pauli and P. R. Willmott. Conducting interfaces between polar and non-polar insulating perovskites. *Journal of Physics: Condensed Matter*, 20(26):264012, 2008.

[20] C. Li, Q. Xu, Z. Wen, S. Zhang, A. Li, and D. Wu. The metallic interface between insulating $NdGaO_3$ and $SrTiO_3$ perovskites. *Applied Physics Letters*, 103(20):201602, 2013.

[21] G. Binnig, H. Rohrer, Ch. Gerber, and E. Weibel. Surface studies by scanning tunneling microscopy. *Physical Review Letters*, 49(1):57–61, 1982.

[22] A. N. Chaika. High resolution STM imaging. In *Surface Science Tools for Nanomaterials Characterization*, pages 561–619. Springer Berlin Heidelberg, 2015.

[23] C. Bai. Scanning tunneling microscopy and its applications. *Shanghai Scientific Technical Publishers, Shanghai, 2nd edition*, 32, 2000.

[24] C. J. Chen and W. F. Smith. Introduction to scanning tunneling microscopy. *American Journal of Physics*, 62(6):573–574, 1994.

[25] S. Ernst, S. Wirth, M. Rams, V. Dolocan, and F. Steglich. Tip preparation for usage in an ultra-low temperature UHV scanning tunneling

microscope. *Science and Technology of Advanced Materials*, 8(5):347–351, 2007.

[26] C. Davisson and L. H. Germer. Diffraction of electrons by a crystal of nickel. *Physical Review*, 30(6):705–740, 1927.

[27] M. P. Seah and W. A. Dench. Quantitative electron spectroscopy of surfaces: A standard data base for electron inelastic mean free paths in solids. *Surface and interface Analysis*, 1(1):2–11, 1979.

[28] P. Weightman, D. S. Martin, R. J. Cole, and T. Farrell. Reflection anisotropy spectroscopy. *Reports on Progress in Physics*, 68(6):1251, 2005.

[29] J-T. Zettler. Characterization of epitaxial semiconductor growth by reflectance anisotropy spectroscopy and ellipsometry. *Progress in Crystal Growth and Characterization of Materials*, 35(1):27–98, 1997.

[30] I. Kamiya, D. E. Aspnes, L. T. Florez, and J. P. Harbison. Reflectance-difference spectroscopy of (001) GaAs surfaces in ultrahigh vacuum. *Physical Review B*, 46(24):15894, 1992.

[31] T-L. Chan, C. Z. Wang, M. Hupalo, M. C. Tringides, Z-Y. Lu, and K. M. Ho. First-principles studies of structures and stabilities of Pb/Si(111). *Physical Review B*, 68(4):045410, 2003.

[32] J. R. Power, O. Pulci, A. Shkrebtii, S. Galata, A. Astropekakis, K. Hinrichs, N. Esser, R. Del Sole, and W. Richter. Sb-induced (1×1) reconstruction on Si(001). *Physical Review B*, 67(11):115315, 2003.

[33] A. Astropekakis, J. R. Power, K. Fleischer, N. Esser, S. Galata, D. Papadimitriou, and W. Richter. Influence of Sn on the optical anisotropy of single-domain Si(001). *Physical Review B*, 63(8):085317, 2001.

[34] D. S. Martin, A. M. Davarpanah, S. D. Barrett, and P. Weightman. Reflection anisotropy spectroscopy of the Na/Cu(110) (1×2) surface reconstruction. *Physical Review B*, 62(23):15417, 2000.

[35] U. Rossow, R. Goldhahn, D. Fuhrmann, and A. Hangleiter. Reflectance difference spectroscopy RDS/RAS combined with spectroscopic ellipsometry for a quantitative analysis of optically anisotropic materials. *Physica Status Solidi (b)*, 242(13):2617–2626, 2005.

[36] K. Fleischer, R. Verre, O. Mauit, R. G. S. Sofin, L. Farrell, C. Byrne, C. M. Smith, J. F. McGilp, and I. V. Shvets. Reflectance anisotropy spectroscopy of magnetite (110) surfaces. *Physical Review B*, 89(19):195118, 2014.

[37] S. Bahrs, A. Bruchhausen, A. R. Goñi, G. Nieva, A. Fainstein, K. Fleischer, W. Richter, and C. Thomsen. Effect of light on the reflectance anisotropy and chain-oxygen related raman signal in untwinned, underdoped crystals of $YBa_2Cu_3O_{7-\delta}$. *Journal of Physics and Chemistry of Solids*, 67(1):340–343, 2006.

[38] D. E. Aspnes. Above-bandgap optical anisotropies in cubic semiconductors: A visible-near ultraviolet probe of surfaces. *Journal of Vacuum Science & Technology B: Microelectronics Processing and Phenomena*, 3(5):1498–1506, 1985.

[39] J. D. E. McIntyre and D. E. Aspnes. Differential reflection spectroscopy of very thin surface films. *Surface Science*, 24(2):417–434, 1971.

[40] U. Rossow, L. Mantese, and D. E. Aspnes. Lineshapes of surface induced optical anisotropy spectra measured by RDS/RAS. *Applied Surface Science*, 123-124:237–242, 1998.

[41] L. D. Sun, M. Hohage, P. Zeppenfeld, R. E. Balderas-Navarro, and K. Hingerl. Surface-induced d-band anisotropy on Cu(110). *Surface Science*, 527:L184–L190, 2003.

[42] D. Papadimitriou and W. Richter. Highly sensitive strain detection in silicon by reflectance anisotropy spectroscopy. *Physical Review B*, 72(7):075212, 2005.

[43] K. Fleischer, O. Mauit, and I. V. Shvets. Stability and capping of magnetite ultra-thin films. *Applied Physics Letters*, 104(19):192401, 2014.

[44] P. Hohenberg and W. Kohn. Inhomogeneous electron gas. *Physical Review*, 136(3B):864–867, 1964.

[45] W. Kohn and L. J. Sham. Self-consistent equations including exchange and correlation effects. *Physical Review*, 140(4A):A1133–A1138, 1965.

[46] D. M. Ceperley and B. J. Alder. Ground state of the electron gas by a stochastic method. *Physical Review Letters*, 45(7):566–569, 1980.

[47] K. Capelle. A birds-eye view of density-functional theory. *Brazilian Journal of Physics*, 36(4a):1318–1343, 2006.

[48] J. P. Perdew and A. Zunger. Self-interaction correction to density-functional approximations for many-electron systems. *Physical Review B*, 23(10):5048–5079, 1981.

[49] V. I. Anisimov, I. S. Elfimov, N. Hamada, and K. Terakura. Charge-ordered insulating state of Fe_3O_4 from first-principles electronic structure calculations. *Physical Review B*, 54(7):4387 – 4390, 1996.

[50] V. I. Anisimov, J. Zaanen, and O. K. Andersen. Band theory and Mott insulators: Hubbard U instead of Stoner I. *Physical Review B*, 44(3):943–954, 1991.

[51] H. J. Kulik, M. Cococcioni, D. A. Scherlis, and N. Marzari. Density functional theory in transition-metal chemistry: A self-consistent Hubbard U approach. 97(10), 2006.

[52] G. Ketteler, W. Weiss, W. Ranke, and R. Schlögl. Bulk and surface phases of iron oxides in an oxygen and water atmosphere at low pressure. *Physical Chemistry Chemical Physics*, 3(6):1114–1122, 2001.

[53] R. M. Cornell and U. Schwertmann. The iron oxides: structure, properties, reactions, occurrences and uses. *John Wiley & Sons*, 2003.

[54] C. E. Diebel, R. Proksch, C. R. Green, P. Neilson, and M. M. Walker. Magnetite defines a vertebrate magnetoreceptor. *Nature*, 406(6793):299–302, 2000.

[55] G. A. Prinz. Magnetoelectronics. *Science*, 282(5394):1660–1663, 1998.

[56] J. J. Versluijs, M. A. Bari, and J. M. D. Coey. Magnetoresistance of half-metallic oxide nanocontacts. *Physical Review Letters*, 87(2):026601, 2001.

[57] S. Parkin, Xin J., C. Kaiser, A. Panchula, K. Roche, and M. Samant. Magnetically engineered spintronic sensors and memory. *Proceedings of the IEEE*, 91(5):661–680, 2003.

[58] W. H. Bragg. The structure of magnetite and the spinels. *Nature*, 95(2386):561–561, 1915.

[59] E. J. W. Verwey. Electronic conduction of magnetite (Fe_3O_4) and its transition point at low temperatures. *Nature*, 144(3642):327–328, 1939.

[60] B. A. Calhoun. Magnetic and electric properties of magnetite at low temperatures. *Physical Review*, 94(6):1577–1585, 1954.

[61] R. Arras, B. Warot-Fonrose, and L. Calmels. Electronic structure near cationic defects in magnetite. *Journal of physics. Condensed matter*, 25(25):256002, 2013.

[62] Yu. S. Dedkov, U. Rüdiger, and G. Güntherodt. Evidence for the half-metallic ferromagnetic state of Fe_3O_4 by spin-resolved photoelectron spectroscopy. *Physical Review B*, 65(6):073405, 2002.

[63] E. J. W. Verwey and P. W. Haayman. Electronic conductivity and transition point of magnetite (Fe_3O_4). *Physica*, 8(9):979–987, 1941.

[64] W. Kündig and R. S. Hargrove. Electron hopping in magnetite. *Solid State Communications*, 7(1):223–227, 1969.

[65] G. S. Parks and K. K. Kelley. The heat capacities of some metallic oxides. *The Journal of Physical Chemistry*, 30(1):47–55, 1925.

[66] M. Iizumi, T. F. Koetzle, G. Shirane, S. Chikazumi, M. Matsui, and S. Todo. Structure of magnetite (Fe_3O_4) below the Verwey transition temperature. *Acta Crystallographica Section B Structural Crystallography and Crystal Chemistry*, 38(8):2121–2133, 1982.

[67] M. S. Senn, J. P. Wright, and J. P. Attfield. Charge order and three-site distortions in the verwey structure of magnetite. *Nature*, 481(7380):173–176, 2011.

[68] F. Zhou and G. Ceder. First-principles determination of charge and orbital interactions in Fe_3O_4. *Physical Review B*, 81(20):205113, 2010.

[69] D. J. Huang, H.-J. Lin, J. Okamoto, K. S. Chao, H.-T. Jeng, G. Y. Guo, C.-H. Hsu, C.-M. Huang, D. C. Ling, W. B. Wu, C. S. Yang, and C. T. Chen. Charge-orbital ordering and Verwey transition in magnetite measured by resonant soft x-ray scattering. *Physical Review Letters*, 96(9):096401, 2006.

[70] J. P. Wright, J. P. Attfield, and P. G. Radaelli. Charge ordered structure of magnetite Fe_3O_4 below the verwey transition. *Physical Review B*, 66(21):214422, 2002.

[71] H-T. Jeng, G. Y. Guo, and D. J. Huang. Charge-orbital ordering and Verwey transition in magnetite. *Physical Review Letters*, 93(15):156403, 2004.

[72] M. P. Pasternak, W. M. Xu, G. Kh. Rozenberg, R. D. Taylor, and R. Jeanloz. Pressure-induced coordination crossover in magnetite; the breakdown of the Verwey-Mott localization hypothesis. *Journal of Magnetism and Magnetic Materials*, 265(2):L107–L112, 2003.

[73] G. Kh. Rozenberg, M. P. Pasternak, W. M. Xu, Y. Amiel, M. Hanfland, M. Amboage, R. D. Taylor, and R. Jeanloz. Origin of the Verwey transition in Magnetite. *Physical Review Letters*, 96(4):045705, 2006.

[74] J. García and G. Subías. The Verwey transition - a new perspective. *Journal of physics. Condensed matter*, 16(7):R145–R178, 2004.

[75] H. Liu and C. Di Valentin. Band gap in magnetite above Verwey temperature induced by symmetry breaking. *The Journal of Physical Chemistry C*, 121(46):25736–25742, 2017.

[76] R. Grau-Crespo, A. Y. Al-Baitai, I. Saadoune, and N. H. De Leeuw. Vacancy ordering and electronic structure of γ-Fe_2O_3 (maghemite): a theoretical investigation. *Journal of Physics: Condensed Matter*, 22(25):255401, 2010.

[77] F. Koch and J. B. Cohen. The defect structure of $Fe_{1-x}O$. *Acta Crystallographica Section B Structural Crystallography and Crystal Chemistry*, 25(2):275–287, 1969.

[78] F. Schrettle, Ch. Kant, P. Lunkenheimer, F. Mayr, J. Deisenhofer, and A. Loidl. Wüstite: electric, thermodynamic and optical properties of FeO. *The European Physical Journal B*, 85(5):1–13, 2012.

[79] E. Gartstein, J. B. Cohen, and T. O. Mason. Defect agglomeration in Wüstite at high temperatures. *Journal of Physics and Chemistry of Solids*, 47(8):775–781, 1986.

[80] P. D. Battle and A. K. Cheetham. The magnetic structure of non-stoichiometric ferrous oxide. *Journal of Physics C: Solid State Physics*, 12(2):337–345, 1979.

[81] J. G. Bednorz and K. A. Müller. Perovskite type oxides the new approach to high-T_c superconductivity. Nobel lecture. *Angewandte Chemie International Edition*, 27(5):735–748, 1988.

[82] H. Unoki and T. Sakudo. Electron spin resonance of Fe^{3+} in $SrTiO_3$ with special reference to the 110 K phase transition. *Journal of the Physical Society of Japan*, 23(3):546–552, 1967.

[83] K. van Benthem, C. Elsässer, and R. H. French. Bulk electronic structure of $SrTiO_3$: Experiment and theory. *Journal of Applied Physics*, 90(12):6156–6164, 2001.

[84] Y. Mukunoki, N. Nakagawa, T. Susaki, and H. Y. Hwang. Atomically flat (110) $SrTiO_3$ and heteroepitaxy. *Applied Physics Letters*, 86(17):171908, 2005.

[85] M. C. Tarun, F. A. Selim, and M. D. McCluskey. Persistent photoconductivity in strontium titanate. *Physical Review Letters*, 111(18):187403, 2013.

[86] J. F. Schooley, W. R. Hosler, and M. L. Cohen. Superconductivity in semiconducting $SrTiO_3$. *Physical Review Letters*, 12(17):474–475, 1964.

[87] N. Reyren, S. Thiel, A. D. Caviglia, L. F. Kourkoutis, G. Hammerl, C. Richter, C. W. Schneider, T. Kopp, A.-S. Ruetschi, D. Jaccard, M. Gabay, D. A. Muller, J.-M. Triscone, and J. Mannhart. Superconducting interfaces between insulating oxides. *Science*, 317(5842):1196–1199, 2007.

[88] S. Thiel. Tunable quasi-two-dimensional electron gases in oxide heterostructures. *Science*, 313(5795):1942–1945, 2006.

[89] M. Huijben, G. Rijnders, D. H. A. Blank, S. Bals, S. Van Aert, J. Verbeeck, G. Van Tendeloo, A. Brinkman, and H. Hilgenkamp. Electronically coupled complementary interfaces between perovskite band insulators. *Nature Materials*, 5(7):556–560, 2006.

[90] W. Siemons, G. Koster, H. Yamamoto, W. A. Harrison, G. Lucovsky, T. H. Geballe, D. H. A. Blank, and M. R. Beasley. Origin of charge density at $LaAlO_3$ on $SrTiO_3$ heterointerfaces: Possibility of intrinsic doping. *Physical Review Letters*, 98(19):196802, 2007.

[91] G. Herranz, M. Basletić, M. Bibes, C. Carrétéro, E. Tafra, E. Jacquet, K. Bouzehouane, C. Deranlot, A. Hamzić, J.-M. Broto, A. Barthélémy,

and A. Fert. High mobility in $LaAlO_3/SrTiO_3$ heterostructures: origin, dimensionality, and perspectives. *Physical Review Letters*, 98(21):216803, 2007.

[92] M. Yazdi-Rizi, P. Marsik, B. P. P. Mallett, K. Sen, A. Cerreta, A. Dubroka, M. Scigaj, F. Sánchez, G. Herranz, and C. Bernhard. Infrared ellipsometry study of photogenerated charge carriers at the (001) and (110) surfaces of $SrTiO_3$ crystals and at the interface of the corresponding $LaAlO_3/SrTiO_3$ heterostructures. *Physical Review B*, 95(19):195107, 2017.

[93] H. P. R. Frederikse and W. R. Hosler. Hall mobility in $SrTiO_3$. *Physical Review*, 161(3):822–827, 1967.

[94] C. Baeumer, C. Xu, F. Gunkel, N. Raab, R. A. Heinen, A. Koehl, and R. Dittmann. Surface termination conversion during $SrTiO_3$ thin film growth revealed by x-ray photoelectron spectroscopy. *Scientific Reports*, 5(1), 2015.

[95] J. P. Perdew, K. Burke, and M. Ernzerhof. Generalized gradient approximation made simple. *Physical Review Letters*, 77(18):3865–3868, 1996.

[96] J. V. Badding. Superconducting materials: Cobalt oxide layers. *Nature Materials*, 2(4):208–210, 2003.

[97] S. Lany. Semiconducting transition metal oxides. *Journal of Physics. Condensed matter*, 27(28):283203, 2015.

[98] Y. Shimakawa, Y. Kubo, and T. Manako. Giant magnetoresistance in $Ti_2Mn_2O_7$ with the pyrochlore structure. *Nature*, 379(6560):53–55, 1996.

[99] R. Bliem, E. McDermott, P. Ferstl, M. Setvin, O. Gamba, J. Pavelec, M. A. Schneider, M. Schmid, U. Diebold, P. Blaha, L. Hammer, and G. S. Parkinson. Subsurface cation vacancy stabilization of the magnetite (001) surface. *Science*, 346(6214):1215–1218, 2014.

[100] R. E. Tanner, M. R. Castell, and G. A. D. Briggs. High resolution scanning tunnelling microscopy of the rutile TiO_2(110) surface. *Surface Science*, 412-413:672–681, 1998.

[101] M. Paul, M. Sing, R. Claessen, D. Schrupp, and V. A. M. Brabers. Thermodynamic stability and atomic and electronic structure of reduced Fe_3O_4(111) single-crystal surfaces. *Physical Review B*, 76(7):075412, 2007.

[102] N. G. Condon, F. M. Leibsle, T. Parker, A. R. Lennie, D. J. Vaughan, and G. Thornton. Biphase ordering on Fe_3O_4(111). *Physical Review B*, 55(23):15885–15894, 1997.

[103] J. Moosburger-Will, M. Krispin, M. Klemm, and S. Horn. LEED and STM studies of the stability of the MoO_2(100) surface. *Surface Science*, 605(15-16):1445–1451, 2011.

[104] T. K. Shimizu, J. Jung, H. S. Kato, Y. Kim, and M. Kawai. Termination and Verwey transition of the (111) surface of magnetite studied by scanning tunneling microscopy and first-principles calculations. *Physical Review B*, 81(23):235429, 2010.

[105] N. Berdunov, S. Murphy, G. Mariotto, and I. V. Shvets. Room temperature study of a strain-induced electronic superstructure on a magnetite (111) surface. *Physical Review B*, 70(8):085404, 2004.

[106] B. Walls, O. Lübben, K. Palotás, K. Fleischer, K. Walshe, and I. V. Shvets. Oxygen vacancy induced surface stabilization: (110) terminated magnetite. *Physical Review B*, 94(16):165424, 2016.

[107] S. A. Krasnikov, S. I. Bozhko, K. Radican, O. Lübben, B. E. Murphy, S-R. Vadapoo, H-C. Wu, M. Abid, V. N. Semenov, and I. V. Shvets. Self-assembly and ordering of C60 on the WO_2/W(110) surface. *Nano Research*, 4(2):194–203, 2010.

[108] K. Jordan, A. Cazacu, G. Manai, S. F. Ceballos, S. Murphy, and I. V. Shvets. Scanning tunneling spectroscopy study of the electronic structure of Fe_3O_4 surfaces. *Physical Review B*, 74(8):085416, 2006.

[109] Z. Novotny, N. Mulakaluri, Z. Edes, M. Schmid, R. Pentcheva, U. Diebold, and G. S. Parkinson. Probing the surface phase diagram of $Fe_3O_4(001)$ towards the Fe-rich limit: Evidence for progressive reduction of the surface. *Physical Review B*, 87(19):195410, 2013.

[110] T. J. Beck, A. Klust, M. Batzill, U. Diebold, C. Di Valentin, and A. Selloni. Surface structure of $TiO_2(011)$-(2x1). *Physical Review Letters*, 93(3):036104, 2004.

[111] O. Dulub, L. A. Boatner, and U. Diebold. STM study of the geometric and electronic structure of Zno(0001)-Zn, $(000\bar{1})$-O, $(10\bar{1}0)$, and $(11\bar{2}0)$ surfaces. *Surface Science*, 519(3):201–217, 2002.

[112] S. Förster, K. Meinel, R. Hammer, M. Trautmann, and W. Widdra. Quasicrystalline structure formation in a classical crystalline thin-film system. *Nature*, 502(7470):215–218, 2013.

[113] G. Mariotto, S. F. Ceballos, S. Murphy, N. Berdunov, C. Seoighe, and I. V. Shvets. Self-assembled alkali and alkaline earth metal nanopatterns on $Fe_3O_4(001)$. *Physical Review B*, 70(3):035417, 2004.

[114] U. Diebold. The surface science of titanium dioxide. *Surface Science Reports*, 48(5-8):53–229, 2003.

[115] S. F. Ceballos, G. Mariotto, K. Jordan, S. Murphy, C. Seoighe, and I. V. Shvets. An atomic scale STM study of the $Fe_3O_4(001)$ surface. *Surface Science*, 548(1-3):106–116, 2004.

[116] Sh. K. Shaikhutdinov, M. Ritter, X.-G. Wang, H. Over, and W. Weiss. Defect structures on epitaxial $Fe_3O_4(111)$ films. *Physical Review B*, 60(15):11062–11069, 1999.

[117] J. A. Enterkin, A. K. Subramanian, B. C. Russell, M. R. Castell, K. R. Poeppelmeier, and L. D. Marks. A homologous series of structures on the surface of $SrTiO_3$(110). *Nature Materials*, 9:245–248, 2010.

[118] Y. Liang, F. Li, W. Wang, H. Yang, and J. Guo. Formation of Sr adatom chains on $SrTiO_3$(110) surface determined by strain. *Journal of Physics: Condensed Matter*, 28(36):365003, 2016.

[119] P. W. Tasker. The stability of ionic crystal surfaces. *Journal of Physics C: Solid State Physics*, 12(22):4977–4984, 1979.

[120] J. Goniakowski, F. Finocchi, and C. Noguera. Polarity of oxide surfaces and nanostructures. *Reports on Progress in Physics*, 71(1):016501, 2007.

[121] A. Barbier, C. Mocuta, and G. Renaud. Structure, transformation, and reduction of the polar NiO(111) surface. *Physical Review B*, 62(23):16056–16062, 2000.

[122] O. Dulub, U. Diebold, and G. Kresse. Novel stabilization mechanism on polar surfaces: ZnO(0001)-Zn. *Physical Review Letters*, 90(1):016102, 2003.

[123] A. Subramanian, L. D. Marks, O. Warschkow, and D. E. Ellis. Direct observation of charge transfer at a MgO(111) surface. *Physical Review Letters*, 92(2):026101, 2004.

[124] A. Barbier, G. Renaud, and A. Stierle. The NiO(111)-(1x1) surface. *Surface Science*, 402-404:757–760, 1998.

[125] J. Goniakowski and C. Noguera. The concept of weak polarity: an application to the $SrTiO_3$(001) surface. *Surface Science*, 365(2):L657–L662, 1996.

[126] C. Noguera, A. Pojani, P. Casek, and F. Finocchi. Electron redistribution in low-dimensional oxide structures. *Surface Science*, 507-510:245–255, 2002.

[127] M. Ritter and W. Weiss. $Fe_3O_4(111)$ surface structure determined by LEED crystallography. *Surface Science*, 432(1-2):81–94, 1999.

[128] K. Reuter and M. Scheffler. Composition, structure, and stability of $RuO_2(110)$ as a function of oxygen pressure. *Physical Review B*, 65(3):035406, 2001.

[129] B. Stanka, W. Hebenstreit, U. Diebold, and S. A. Chambers. Surface reconstruction of $Fe_3O_4(001)$. *Surface Science*, 448(1):49–63, 2000.

[130] G. Mariotto, S. Murphy, and I. V. Shvets. Charge ordering on the surface of $Fe_3O_4(001)$. *Physical Review B*, 66(24):245426, 2002.

[131] R. Pentcheva, F. Wendler, H. L. Meyerheim, W. Moritz, N. Jedrecy, and M. Scheffler. Jahn-Teller stabilization of a polar metal oxide surface: $Fe_3O_4(001)$. *Physical Review Letters*, 94(12):126101, 2005.

[132] G. S. Parkinson. Iron oxide surfaces. *Surface Science Reports*, 71(1):272–365, 2016.

[133] J. Noh, O. I. Osman, S. G. Aziz, P. Winget, and J-L. Brédas. Magnetite $Fe_3O_4(111)$ surfaces: impact of defects on structure, stability, and electronic properties. *Chemistry of Materials*, 27(17):5856–5867, 2015.

[134] M. E. Grillo, M. W. Finnis, and W. Ranke. Surface structure and water adsorption on $Fe_3O_4(111)$: Spin-density functional theory and on-site Coulomb interactions. *Physical Review B*, 77(7):075407, 2008.

[135] K. T. Rim, D. Eom, S-W. Chan, M. Flytzani-Stephanopoulos, G. W. Flynn, X-D. Wen, and E. R. Batista. Scanning tunneling microscopy and theoretical study of water adsorption on Fe_3O_4: implications for catalysis. *Journal of the American Chemical Society*, 134(46):18979–18985, 2012.

[136] N. Berdunov, G. Mariotto, S. Murphy, K. Balakrishnan, and I. V. Shvets. Self-assembly of iron nanoclusters on the $Fe_3O_4(111)$ superstructured surface. *Physical Review B*, 71(11):113406, 2005.

[137] R. Jansen, B. J. Nelissen, D. L. Abraham, H. van Kempen, and V. A. M. Brabers. Surface structure of $Fe_3O_4(110)$ studied by scanning tunneling microscopy. *iEEE Transactions on Magnetics*, 30(6):4506–4508, 1994.

[138] R. Jansen, V. A. M. Brabers, and H. van Kempen. One-dimensional reconstruction observed on $Fe_3O_4(110)$ by scanning tunneling microscopy. *Surface Science*, 328(3):237–247, 1995.

[139] R. Jansen. Scanning tunneling microscopy and spectroscopy on thin $Fe_3O_4(110)$ films on MgO. *Journal of Vacuum Science Technology B*, 14(2):1173, 1996.

[140] G. Maris, O. Shklyarevskii, L. Jdira, J. G. H. Hermsen, and S. Speller. One-dimensional structural and electronic properties of magnetite $Fe_3O_4(110)$. *Surface Science*, 600(23):5084–5091, 2006.

[141] G. Maris, L. Jdira, J. G. H. Hermsen, S. Murphy, G. Manai, I. V. Shvets, and S. Speller. Nano-magnetic probing on magnetite. *IEEE Transactions on Magnetics*, 42(10):2927–2929, 2006.

[142] G. Maris, L. Jdira, J. G. H. Hermsen, S. Murphy, G. Manai, I. V. Shvets, and S. Speller. Towards spin-polarized scanning tunneling microscopy on magnetite (110). *Japanese Journal of Applied Physics*, 45(3B):2225–2229, 2006.

[143] G. S. Parkinson, P. Lackner, O. Gamba, S. Maaß, S. Gerhold, M. Riva, R. Bliem, U. Diebold, and M. Schmid. $Fe_3O_4(110)$-(1x3) revisited: Periodic (111) nanofacets. *Surface Science*, 649(7):120–123, 2016.

[144] D. Santos-Carballal, A. Roldan, R. Grau-Crespo, and N. H. de Leeuw. A DFT study of the structures, stabilities and redox behaviour of the major surfaces of magnetite Fe_3O_4. *Physical Chemistry Chemical Physics*, 16(39):21082–21097, 2014.

[145] R. Herger, P. R. Willmott, O. Bunk, C. M. Schlepütz, B. D. Patterson, and B. Delley. Surface of strontium titanate. *Physical Review Letters*, 98(7):076102, 2007.

[146] M. R. Castell. Scanning tunneling microscopy of reconstructions on the $SrTiO_3$(001) surface. *Surface Science*, 505:1–13, 2002.

[147] F. Silly, D. T. Newell, and M. R. Castell. $SrTiO_3$(001) reconstructions: the (2×2) to c(4×4) transition. *Surface Science*, 600(17):219–223, 2006.

[148] S. Gerhold, Z. Wang, M. Schmid, and U. Diebold. Stoichiometry-driven switching between surface reconstructions on $SrTiO_3$(001). *Surface Science*, 621:L1–L4, 2014.

[149] T Kubo and H Nozoye. Surface structure of $SrTiO_3$(100). *Surface Science*, 542(3):177–191, 2003.

[150] M. Kareev, S. Prosandeev, J. Liu, C. Gan, A. Kareev, J. W. Freeland, M. Xiao, and J. Chakhalian. Atomic control and characterization of surface defect states of TiO_2 terminated $SrTiO_3$ single crystals. *Applied Physics Letters*, 93(6):061909, 2008.

[151] A. Biswas, P. B. Rossen, C.-H. Yang, W. Siemons, M.-H. Jung, I. K. Yang, R. Ramesh, and Y. H. Jeong. Universal Ti-rich termination of atomically flat $SrTiO_3$ (001), (110), and (111) surfaces. *Applied Physics Letters*, 98(5):051904, 2011.

[152] C. Rodenbücher, S. Wicklein, R. Waser, and K. Szot. Insulator-to-metal transition of $SrTiO_3$:Nb single crystal surfaces induced by Ar bombardment. *Applied Physics Letters*, 102(10):101603, 2013.

[153] B. Psiuk, J. Szade, and K. Szot. $SrTiO_3$ surface modification upon low energy Ar^+ bombardment studied by XPS. *Vacuum*, 131:14–21, 2016.

[154] R. Bachelet, F. Sánchez, F. J. PaloMares, C. Ocal, and J. Fontcuberta. Atomically flat SrO-terminated $SrTiO_3$(001) substrate. *Applied Physics Letters*, 95(14):141915, 2009.

[155] B. C. Russell and M. R. Castell. Surface of sputtered and annealed polar $SrTiO_3(111)$: TiO_x-rich (n×n) reconstructions. *The Journal of Physical Chemistry C*, 112(16):6538–6545, 2008.

[156] B. C. Russell and M. R. Castell. (13×13)R13.9° and (7×7)R19.1° reconstructions of the polar $SrTiO_3(111)$ surface. *Physical Review B*, 75(15):155433, 2007.

[157] J. Brunen and J. Zegenhagen. Investigation of the $SrTiO_3(110)$ surface by means of LEED, scanning tunneling microscopy and auger spectroscopy. *Surface Science*, 389(1-3):349–365, 1997.

[158] B. C. Russell and M. R. Castell. Reconstructions on the polar $SrTiO_3(110)$ surface: Analysis using STM, LEED, and AES. *Physical Review B*, 77(24):245414, 2008.

[159] F. Li, Z. Wang, S. Meng, Y. Sun, J. Yang, Q. Guo, and J. Guo. Reversible transition between thermodynamically stable phases with low density of oxygen vacancies on the $SrTiO_3(110)$ surface. *Physical Review Letters*, 107(3):036103, 2011.

[160] Z. Wang, J. Feng, Y. Yang, Y. Yao, L. Gu, F. Yang, Q. Guo, and J. Guo. Cation stoichiometry optimization of $SrTiO_3(110)$ thin films with atomic precision in homogeneous molecular beam epitaxy. *Applied Physics Letters*, 100(5):051602, 2012.

[161] Z. Wang, F. Yang, Z. Zhang, Y. Tang, J. Feng, K. Wu, Q. Guo, and J. Guo. Evolution of the surface structures on $SrTiO_3(110)$ tuned by Ti or Sr concentration. *Physical Review B*, 83(15):036103, 2011.

[162] Y. Cao, S. Wang, S. Liu, Q. Guo, and J. Guo. Electronic structures of the $SrTiO_3(110)$ surface in different reconstructions. *The Journal of Chemical Physics*, 137(4):044701, 2012.

[163] B.Psiuk, J. Szade, M. Pilch, and K. Szot. XPS studies of perovskites surface instability caused by Ar ion and electron bombardment and metal deposition. *Vacuum*, 83:S69–S72, 2009.

[164] S. Gerhold, M. Riva, Z. Wang, R. Bliem, M. Wagner, J. Osiecki, K. Schulte, M. Schmid, and U. Diebold. Nickel-oxide-modified $SrTiO_3(110)$-(4×1) surfaces and their interaction with water. *The Journal of Physical Chemistry C*, 119(35):20481–20487, 2015.

[165] R. Aragón, R. J. Rasmussen, J. P. Shepherd, J. W. Koenitzer, and J. M. Honig. Effect of stoichiometry changes on electrical properties of magnetite. *Journal of Magnetism and Magnetic Materials*, 54-57:1335–1336, 1986.

[166] F. Bourgeois, P. Gergaud, H. Renevier, C. Leclere, and G. Feuillet. Low temperature oxidation mechanisms of nanocrystalline magnetite thin film. *Journal of Applied Physics*, 113(1):013510, 2013.

[167] S. F. Alvarado A. Schlegel and P. Wachter. Optical properties of magnetite (Fe_3O_4). *Journal of Physics C: Solid State Physics*, 12(6):1157–1164, 1979.

[168] T. Tepper, C. A. Ross, and G. F. Dionne. Microstructure and optical properties of pulsed-laser-deposited iron oxide films. *iEEE Transactions on Magnetics*, 40(3):1685–1690, 2004.

[169] V. N. Antonov, B. N. Harmon, V. P. Antropov, A. Ya. Perlov, and A. N. Yaresko. Electronic structure and magneto-optical Kerr effect of Fe_3O_4 and Mg^{2+} - or Al^{3+} -substituted Fe_3O_4. *Physical Review B*, 64(13):134410, 2001.

[170] W. F. J. Fontijn, P. J. van der Zaag, M. A. C. Devillers, V. A. M. Brabers, and R. Metselaar. Optical and magneto-optical polar kerr spectra of Fe_3O_4 and Mg^{2+} or Al^{3+} -substituted Fe_3O_4. *Physical Review B*, 56(9):5432–5442, 1997.

[171] H-T. Jeng and G. Y. Guo. First-principles investigations of the electronic structure and magnetocrystalline anisotropy in strained magnetite Fe_3O_4. *Physical Review B*, 65(9):094429, 2002.

[172] K. Fleischer, S. Chandola, Th. Herrmann, N. Esser, W. Richter, and J. F. McGilp. Free-electron response in reflectance anisotropy spectra. *Physical Review B*, 74(19):195432, 2006.

[173] V. E. Henrich, G. Dresselhaus, and H. J. Zeiger. Surface defects and the electronic structure of $SrTiO_3$ surfaces. *Physical Review B*, 17(12):4908–4921, 1978.

[174] U. Rossow. Interpretation of surface-induced optical anisotropy of clean, hydrogenated, and oxidized vicinal silicon surfaces investigated by reflectance-difference spectroscopy. *Journal of Vacuum Science & Technology B: Microelectronics and Nanometer Structures*, 14(4):3070, 1996.

[175] K. Hingerl, R. E. Balderas-Navarro, A. Bonanni, P. Tichopadek, and W. G. Schmidt. On the origin of resonance features in reflectance difference data of silicon. *Applied Surface Science*, 175-176:769–776, 2001.

[176] Y. S. Kim, J. Kim, S. J. Moon, W. S. Choi, Y. J. Chang, J.-G. Yoon, J. Yu, J.-S. Chung, and T. W. Noh. Localized electronic states induced by defects and possible origin of ferroelectricity in strontium titanate thin films. *Applied Physics Letters*, 94(20):202906, 2009.

[177] K. Eom, E. Choi, M. Choi, S. Han, H. Zhou, and J. Lee. Oxygen vacancy linear clustering in a perovskite oxide. *The Journal of Physical Chemistry Letters*, 8(15):3500–3505, 2017.

[178] H. Cheng and A. Selloni. Surface and subsurface oxygen vacancies in anatase TiO_2 and differences with rutile. *Physical Review B*, 79(9), 2009.

[179] B. Reihl, J. G. Bednorz, K. A. Müller, Y. Jugnet, G. Landgren, and J. F. Morar. Electronic structure of strontium titanate. *Physical Review B*, 30(2):803–806, 1984.

[180] G. Herranz, F. Sánchez, N. Dix, M. Scigaj, and J. Fontcuberta. High mobility conduction at (110) and (111) $LaAlO_3/SrTiO_3$ interfaces. *Scientific Reports*, 2(1), 2012.

[181] T. Fujii, F. M. F. de Groot, G. A. Sawatzky, F. C. Voogt, T. Hibma, and K. Okada. *In-situ* XPS analysis of various iron oxide films grown by NO_2-assisted molecular-beam epitaxy. *Physical Review B*, 59(4):3195–3202, 1999.

[182] T. Yamashita and P. Hayes. Analysis of XPS spectra of Fe^{2+} and Fe^{3+} ions in oxide materials. *Applied Surface Science*, 254(8):2441–2449, 2008.

[183] C. R. Brundle, T. J. Chuang, and K. Wandelt. Core and valence level photoemission studies of iron oxide surfaces and the oxidation of iron. *Surface Science*, 68:459–468, 1977.

[184] J. A. Van Orman and K. L. Crispin. Diffusion in oxides. *Reviews in Mineralogy and Geochemistry*, 72(1):757–825, 2010.

[185] Y. L. Li, K. L. Yao, and Z. L. Liu. Structure, stability and magnetic properties of the $Fe_3O_4(110)$ surface: Density functional theory study. *Surface Science*, 601(3):876–882, 2007.

[186] G. Mariotto, S. Murphy, N. Berov, S. F. Ceballos, and I. V. Shvets. Influence of Ca and K on the reconstruction of the $Fe_3O_4(001)$ surface. *Surface Science*, 564:79–86, 2004.

[187] A. R. Lennie, N. G. Condon, F. M. Leibsle, P. W. Murray, G. Thornton, and D. J. Vaughan. Structures of $Fe_3O_4(111)$ surfaces observed by scanning tunneling microscopy. *Physical Review B*, 53(15):10244–10253, 1996.

[188] P. E. Blöchl. Projector augmented-wave method. *Physical Review B*, 50(24):17953–17979, 1994.

[189] G. Kresse and D. Joubert. From ultrasoft pseudopotentials to the projector augmented-wave method. *Physical Review B*, 59(3):1758–1775, 1999.

[190] G. Kresse and J. Furthmüller. Efficiency of ab-initio total energy calculations for metals and semiconductors using a plane-wave basis set. *Computational Materials Science*, 6(1):15–50, 1996.

[191] G. Kresse and J. Furthmüller. Efficient iterative schemes for ab initio total-energy calculations using a plane-wave basis set. *Physical Review B*, 54(16):11169–11186, 1996.

[192] H. J. Monkhorst and J. D. Pack. Special points for brillouin-zone integrations. *Physical Review B*, 13(11):5188–5192, 1976.

[193] J. Tersoff and D. R. Hamann. Theory of the scanning tunneling microscope. *Physical Review B*, 31(2):805–813, 1985.